DEVELOPMENT OF A LASER LIFETIME PRESSURE-SENSITIVE PAINT METHOD FOR TURBINE ANALYSIS

by

Papa Aye Nyansafo Aye-Addo

A Dissertation

Submitted to the Faculty of Purdue University

In Partial Fulfillment of the Requirements for the degree of

Doctor of Philosophy

School of Aeronautics & Astronautics

West Lafayette, Indiana

December 2021

THE PURDUE UNIVERSITY GRADUATE SCHOOL
STATEMENT OF COMMITTEE APPROVAL

Dr. Guillermo Paniagua, Chair

School of Mechanical Engineering

Dr. John P. Sullivan

School of Aeronautics and Astronautics

Dr. Steven F. Son

School of Mechanical Engineering

Dr. Terrence R. Meyer

School of Mechanical Engineering

Approved by:

Dr. Gregory A. Blaisdell

To my parents Rev. Prof. Charles Aye-Addo and Dr. Gertrude Aye-Addo. Your love, sacrifice, and support are the reasons why I can pursue my dreams.

Psalms 111:2-4

Great are the works of the LORD, studied by all who delight in them. Full of splendor and majesty is his work, and his righteousness endures forever. He has caused his wondrous works to be remembered; the LORD is gracious and merciful.

ACKNOWLEDGMENTS

First and foremost, I am grateful to God for the opportunity to pursue and complete my doctoral program. I am also thankful to my research advisors, family, and friends for supporting me throughout my graduate school tenure. Your dedication to my success provided vital support for me to persevere to finish writing my dissertation.

Over the past five years, my primary advisor, Dr. Guillermo Paniagua, has helped me develop confidence in my research aptitude and experimental methodology. As an advisor and mentor, he continually expressed a deep appreciation for working together and collaborating with other research groups. I am much obliged to Dr. Terrence Meyer and the Advanced Diagnostics and Propulsion Research Laboratory for loaning the Quasi-continuous burst mode research laser for my experiments and Mateo Gomez, who was instrumental in fixing and aligning the laser. I greatly appreciate my doctoral committee's time and valuable feedback, including Dr. John Sullivan and Dr. Steven Son. When I started investigating Pressure Sensitive Paint (PSP), Dr. Sullivan graciously offered some materials and equipment for initial trials. I am also thankful to the Rolls-Royce STARR program, which funded my research expenses, including lab equipment, conference travel, and journal publications.

I am profoundly thankful to all the past and present students from the Purdue Experimental Turbine Aerothermal Lab. Through our interactions building up the research facility from an empty test cell, using shared equipment, or spending hours setting up experiments, your commitment to excellent work and unique perspective on problem-solving made my experience working with you enjoyable. I am also thankful for the deep and fulfilling relationships with my brothers and sisters in Christ, including Pastors Tom Biang and Fred Douglas, Prof. Seth Armah, Town Oh, Dr. Aaron Gall, Greg Gerard, Nadia Numa, Allison Chau, and Dr. Phu Vo. I am also grateful for the encouragement and friendship from my cohort, including Dr. Rufat Kulakhmetov, Dr. Paht Juangphanich, and Dr. Kola Ogunsina.

Last but not least, I am indebted to my family for their unwavering love, support, and encouragement. Without the sacrifice and determination of my parents, I will not have had the opportunity to live and study in the United States. My lovely sisters took care of me in many ways than I can recount. They always welcomed me home to rest and recover, and I believe they also succeeded in transforming me into a stylish Ph.D. student.

TABLE OF CONTENTS

LIST OF TABLES

LIST OF FIGURES

NOMENCLATURE

Abbreviation

d_{fr}	=	Fractal diameter of pores
h	=	Coating thickness
n_{pore}	=	Number of pores
r_{pore}	=	Mean radius of pores
t	=	Time
A	=	Stern Volmer coefficient
A_m	=	Amplitude
AA	=	Anodized Aluminum
B	=	Stern Volmer coefficient
BPF	=	Blade passing frequency
C	=	2nd order polynominal coefficient
CCD	=	Charge coupled device
CFD	=	Computational Fluid Dynamics
CMOS	=	Complementary metal-oxide semiconductor
D_m	=	Mass diffusivity of oxygen
DLT	=	Direct linear transformation
FS	=	Full scale output
FOV	=	Field of view
FLA	=	Forward looking aft
H	=	Modulation depth
I	=	Intensity emission
K_q	=	Rate constant for quenching process
LED	=	Light-emitting diode
LPF	=	Low-pass filter
M_{eff}	=	Amplitude modulation index
MLC	=	Metal-liquid complexes
N	=	total number of images
Nd: YAG	=	Neodymium-doped yttrium aluminum garnet

P	=	Static pressure
P_{ref}	=	Reference static pressure
PC	=	Polymer ceramic
PS	=	Airfoil pressure side
PSP	=	Pressure Sensitive Paint
PIV	=	Particle Image Velocimetry
PMT	=	Photomultiplier tube
PtTFPP	=	Platinum tetra-fluorenyl porphyrin
PtTFPP-PP	=	Platinum tetra-fluorenyl porphyrin / Polymer ceramic porous binder
RANS	=	Reynolds-Averaged Navier-Stokes
Re/L	=	Reynolds number per unit length
ROI	=	Region of interest
S_0	=	Singlet ground
S_1	=	First electronic state
S_2	=	Second electronic state
SS	=	Airfoil suction side
SNR	=	Signal to noise ratio
T	=	Temperature
T_1	=	First triplet state
TLC	=	Thin-layer Chromatography
TRL	=	Technology Readiness Level
TTL	=	Transistor-transistor logic
URANS	=	Unsteady Reynolds-Averaged Navier-Stokes

Subscripts

i	=	matrix row
j	=	matrix column
1,2,3	=	2nd order polynomial coefficients
T	=	Total temperature
o	=	reference time constant
ref	=	reference condition

max	=	Maximum
min	=	Minimum
avg	=	Mean
RMS	=	Root mean squared
STD	=	Standard Deviation

Greek Symbols

φ_n	=	Phase angle
ω_n	=	Modulation frequency
μ	=	mean
σ	=	standard deviation
ρ	=	Density
τ	=	Luminescent lifetime constant
τ_o	=	Reference lifetime constant

ABSTRACT

To increase overall aircraft engine efficiency, the diameter of the high-pressure turbine is reduced, leading to low aspect ratio airfoils. Secondary flow dominates in these low aspect ratio turbines, and the small airfoil geometry inhibits flush-mounted, full-spatial dynamic pressure measurements with pressure transducers. Airfoil surface pressure measurements are vital to understanding the inherently unsteady flow phenomena in turbines. Additionally, aerodynamic performance data derived from high-resolution surface pressure measurements provide invaluable data for validating computational fluid dynamics codes used for prediction. Non-intrusive measurement techniques such as fast-responding Pressure Sensitive Paint (PSP) offer a potential solution of a full-field optical measurement of surface pressure fluctuation, with each camera pixel representing a sensor. The porous binder improves the dynamic response of PSP, making it suitable for unsteady flow environments such as turbomachinery applications. In this view, the overall objective of the current doctoral research is to develop a lifetime PSP method using laser-based excitation for surface pressure measurement on a new class of high-pressure turbines.

The overall research goal was subdivided into three main strategies. (1) A pulse lifetime calibration procedure of a porous polymer/ceramic binder PSP was developed in a pressure-controlled chamber to assess the correlation between pressure and time-resolved luminescent lifetime, pressure sensitivity, and signal-to-noise ratio. (2) The lifetime technique was implemented for surface pressure measurements in a linear test section to measure high spatial pressure gradients and resolve unsteady flow features. A data reduction routine and an optimal binning bundle of pixels were proposed for calibration analysis to reduce the overall pressure uncertainty. Uncertainty quantification and sensitivity analysis were also completed to determine the parameters with a substantial effect on the pressure uncertainty. (3) The pulse lifetime method was demonstrated on a high-pressure turbine vane suction surface at engine representative conditions. The surface pressure data were corroborated with static pressure tappings and computational simulations. This research effort provided new insights into time-resolved luminescent lifetime PSP techniques. Steady and unsteady flow features from surface pressure measurements were identified using a precise calibration method. The lifetime pulse method was effective in a high-pressure turbine flow field, paving the way for back-to-back PSP experiments with different turbine geometries.

CHAPTER 1: INTRODUCTION

Modern civil turbofans evolve towards smaller engine cores, increasing propulsive efficiency and reducing jet noise. However, secondary flows dominate the flow field of high-pressure turbines within the engine core because of the airfoils' low aspect ratio (span-to-chord ratio) and high turning ([1–4]). These secondary flows, which scale with the blade chord, are created at the end wall and blade junction and extract energy from the fluid, otherwise used to rotate the blade and produce thrust, resulting in incidence loss in the next stage of the turbine [5]. The turbine flow field is inherently unsteady with multi-stage stator-rotor interactions, adversely impacting airfoils' aerodynamic loading, thermal management, and structural integrity ([6–8]). As turbine designers aim for 0.5% improvement in overall efficiency [9], high fidelity experimental data is essential to assess turbine performance with high accuracy and improved spatial resolution.

Turbine aerothermal research facilities primarily rely on instrumentation, such as pneumatic tubing connected to an orifice hole of 0.016" diameter, to measure the airfoil surface pressure or ultra-miniature piezo-resistive sensors (0.066" diameter) to measure unsteady pressure. Without a protective screen, the piezo-resistive sensors have an ideal natural frequency of 300 kHz for a range of 345 kPa. However, the small airfoil geometry inhibits flush-mounted, full-spatial dynamic pressure measurements with these sensors. Moreover, unsteady flow separation is more relevant and challenging to predict using computational models such as unsteady Reynolds Averaged Navier Stokes (URANS) solvers. High-frequency pressure-sensitive paint (PSP) offers a potential solution of a full-field accurate measurement of surface pressure fluctuation, with each camera pixel representing a sensor.

This dissertation focuses on developing an optical surface pressure measurement technique for high-pressure turbine analysis at engine-relevant conditions. The research outcomes reinforce the fundamental principles of pulse lifetime PSP with a comprehensive and precise calibration study, uncertainty quantification, and potential as a rapid, robust method for evaluating the aerodynamic performance of turbine airfoil designs.

1.1 Research Objectives

To increase overall aircraft engine efficiency, the diameter of the high-pressure turbine is reduced, leading to low aspect ratio turbines. In these low aspect ratio turbines, secondary flow dominates, and due to its small size, it is complicated to mount pressure transducers. The overall objective of this dissertation is to demonstrate optical surface pressure measurements on a new class of turbines. The overall goal can be subdivided into three main points:

1. **<u>Accuracy Assessment of a Pulse Lifetime Procedure with no-flow</u>**

Most studies have focused on the lifetime-gated method with low-frequency excitation; however, there is a lack of research on the pulse-lifetime technique, including a fundamental understanding of the underlying luminescence decay process with high spatial and temporal analysis. The objective is to develop a calibration procedure for a laser-based high-frequency pulse lifetime PSP method and evaluate the calibration method's accuracy.

2. **<u>Uncertainty Quantification and Unsteady Analysis of the Pulse Lifetime Method in a Linear Test Section</u>**

The pulse lifetime procedure was tested on a wavy surface exposed to supersonic flow in a linear test section (TRL 1-2). The objective is to assess the feasibility of the technique for aerodynamic testing with high spatial pressure gradients, perform an uncertainty analysis of the method, and test its capability to resolve unsteady flow features.

3. **<u>Application of the Pulse Lifetime PSP Method in an Annular Test Section</u>**

The surface pressure is an important parameter for quantifying the lift distribution and aerodynamic loading of turbine airfoil designs. Using the pulse lifetime PSP method, the objective is to measure the surface pressure on a high-pressure turbine vane suction surface in an annular test section (TRL 3-4). The experimental data are corroborated with computational RANS solver results.

1.2 Research Methodology

The following methodology is outlined to achieve the three research objectives explained in the previous section:

1.) Development of a Calibration Procedure for the Pulse Lifetime PSP Method

A calibration technique is developed to evaluate the pulse lifetime method's accuracy, reliability, and uncertainty. A systematic evaluation of the pulse lifetime method is investigated by manufacturing and testing a pressure chamber operated under vacuum and above ambient pressure with optical access to excite and capture the fluorescence of a sample PSP coupon.

The calibration test specimen is a 54 mm diameter Aluminum disc of 3.175 mm thickness sprayed with a commercially available porous PSP (PtTFPP adsorbed in a Polymer-ceramic binder) with a lifetime of approximately 10 µs (~ 16 kHz cutoff frequency) under ideal conditions at ambient pressure. A state-of-the-art quasi-continuous burst-mode Neodymium-doped Yttrium Aluminum Garnet (Nd: YAG) laser provides a high energy output of 215 mJ/pulse to excite the PSP at 532 nm. The laser has a repetition rate of 10 kHz, a burst duration of 10.8 milliseconds, and a wait time of 10 seconds between each pulse burst. A high-speed *Shimadzu HPV-X2* camera records 240 images at 400 kHz to capture the luminescence decay of PtTFPP for each of the 15 calibration pressure points. A *GE DPI 610* pressure calibrator sets the O_2 concentration in the chamber. The calibration procedure is summarized in Figure 1. A Quantum Composer 9530 pulse delay generator triggers and synchronizes the camera and laser. After every pulse, the camera acquires 20 images with a delay of 10 ns before the first image.

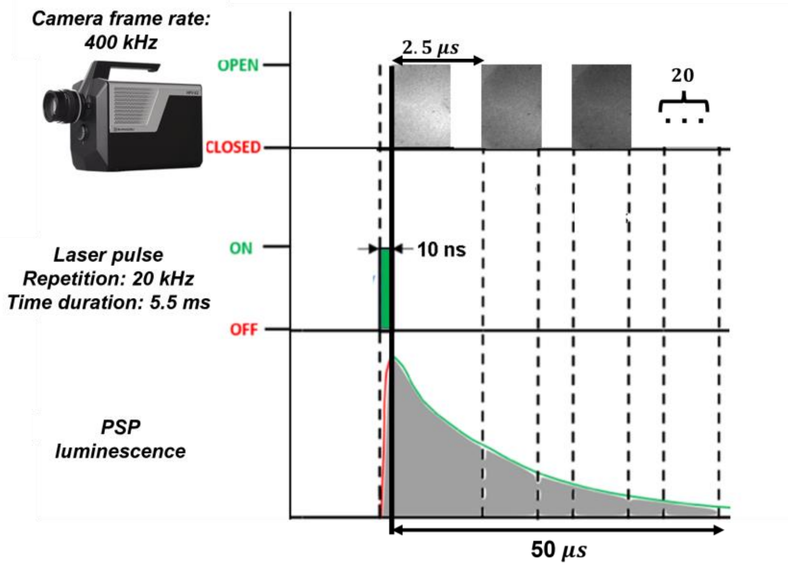

Figure 1: Calibration procedure for high-frequency pulse lifetime method

A single exponential decay model is used to calculate the lifetime at each calibration pressure for each bundle of pixels, using only the 2nd through 4th images. A 2nd order polynomial is used to develop a calibration curve between the normalized lifetime and pressure using the calculated lifetime results. The results yield a unique set of calibration coefficients for each bundle of pixels. The calibration results are analyzed to determine the difference between the reconstructed pressure from PSP and the pressure set by the calibrator. The pressure sensitivity, signal-to-noise (SNR) ratio, and the thickness variation of the calibration coupon are analyzed.

2.) Demonstration of Pulse Lifetime PSP in a Supersonic Test Section

The pulse lifetime PSP method is demonstrated in a supersonic test section with vacuum experiments. The test article is a convergent-divergent section followed by wavy surfaces. Porous PSP was applied on two waves to test the capability of measuring unsteady pressure in the shear layer, separation, and downstream compression zones. The PSP calibration is performed *in-situ* with the entire test section under vacuum, using the static pressure tappings as a reference. Under a vacuum, the wavy surface is exposed to supersonic flow during wind-on experiments. Three mass flow rates are tested to evaluate the capability of measuring pressure gradients up to 15 kPa. A comprehensive uncertainty quantification and sensitivity analysis of the calibration method is performed to determine the parameters with a substantial effect on the pressure uncertainty. A data processing tool is developed to remove images with a low SNR and select an optimal binning bundle of pixels to reduce uncertainty. The time-averaged spatially resolved surface pressure from PSP is compared with static pressure tappings, Computational Fluid Dynamics (CFD) RANS results, and Shadowgraph experimental results. A spatial-temporal analysis of pressure is conducted to identify unsteady flow patterns across the surface pressure field.

3.) Integration of Pulse Lifetime PSP in a High-Pressure Turbine Vane Annular Cascade

In this phase, the pulse lifetime method is applied on a high-pressure turbine vane suction surface in an annular test section (TRL 3-4) to characterize wall pressure distribution. The annular vane cascade is a large capacity test section with a shroud diameter of 840 mm, able to handle mass flows up to 18 kg/s at a wide range of temperatures. The test section's large size maximizes the spatial resolution of optical techniques such as PSP and high-frequency Particle Image Velocimetry (PIV). The test section is equipped with instrumentation for performance characterization, including static pressure tappings.

An optical alignment process is developed with a laser delivery probe and a rigid borescope-intensifier-camera setup. A vacuum pump connected to the wind tunnel lowers the test section's ambient pressure to 80 kPa in several steps to calibrate the PSP *in situ*. Time-averaged reconstructed pressure from the PSP is compared with low-frequency static pressure tappings and computational simulations. The results of time-resolved pressure are analyzed using DFT for a bundle of 5x5 pixels.

1.3 Structure of the document

The dissertation is divided into six chapters according to each of the research methodologies:

- **Chapter 2** is a concise but substantive overview of pressure-sensitive paint methods used for aerodynamic testing. It describes and explains the relevant photophysical principles for the lifetime PSP technique.
- **Chapter 3** explains the development of the pulse lifetime procedure. A systematic evaluation of the pulse lifetime technique is completed, including the criteria for selecting the composition of the luminophore molecule and binder, illumination source, and camera. The experimental setup for pulse lifetime and calibration sequence with a Quasi-continuous burst mode laser is described. The coating thickness of the calibration coupon is measured

with a corrective calibration procedure as a source of error in the overall measurement uncertainty. At constant pressure and temperature, the intensity, lifetime, and reconstructed pressures spatial variation are assessed, and the reduction of spatial variation by ratioing is explained. The single exponential decay is evaluated to model the luminescence decay of the PSP, and a 2nd order polynomial is assessed for the correlation of pressure and lifetime. The lifetime calibration results from the PSP are compared with the set calibrator pressures to evaluate the relative difference. The pressure sensitivity and signal-to-noise ratio as a function of the calibration pressure is illustrated.

- **Chapter 4** describes the validation of the pulse lifetime technique in a low TRL (1-2) linear test section. The test section is a converging-diverging nozzle followed by a wavy surface. The explanation of the experimental setup includes the optical layout, application of PSP on the test apparatus, inlet flow conditions, no-flow calibration sequence, and data synchronization. A data processing routine is described in detail to remove data with low SNR, reduce uncertainty, and select the optimal binning for flow-field. A combination of points on the intensity decay curve was evaluated to understand the effect on the calculated lifetime and coefficient of determination. A pixel binning study was performed to reduce the uncertainty of using a single averaged value across all pixels and image pixelization without distorting the image. Low-frequency discrete pressure sensors are compared with the calibration results from the PSP to assess the relative difference. A detailed calibration uncertainty is performed considering the parameters that affect the conversion of the single exponential lifetime to pressure using a quadratic relationship. The time-averaged and spanwise-averaged pressure results are evaluated and compared to static pressure tappings, and the 2-D images from the camera are mapped to the 3-D geometry. A spatial-temporal analysis is conducted to assess pressure fluctuations.
- **Chapter 5** investigates the pulse lifetime PSP technique at 20 kHz applied in an annular vane cascade (TRL 3-4). In the annular test section, the PSP technique was used to measure the time-averaged static pressure field on the suction surface of a high-pressure turbine vane. The experiments were conducted at engine representative conditions in the Purdue Big Rig for Annular Stationary Turbine Analysis module at the Purdue Experimental Turbine Aerothermal Lab. The 2-D pressure results showed a gradual pressure increase in the spanwise and flow directions, corroborated with local static pressure taps and

computational results. The variation in PSP thickness was measured as a contribution to the uncertainty. The DFT of the unsteady pressure signal showed increased frequency content in wind-on conditions than wind-off conditions at the mid-span and 30% span. Compared to the mid-span region, there were increased frequencies and pressure amplitudes in the hub end wall region.

- **Chapter 6** summarizes the conclusions of the research objectives and how each objective was completed.

CHAPTER 2: A REVIEW OF PRESSURE-SENSITIVE PAINT METHODS

2.1 Pressure Sensitive Paint

The oxygen quenching process of luminophores in solution or adsorbed on an oxygen porous binder material has been well understood since the 1930s [10]. Oxygen quenching is the collisional deactivation of the molecule by an oxygen quencher and is described by the Stern-Volmer relation [11] shown in eq. (1). According to Henry's law, the oxygen concentration in the binder is proportional to its partial pressure in ambient air, proportional to the local static pressure. The intensity and luminescence lifetime are inversely proportional to pressure, so as the static pressure increases, the luminescent energy of the luminophore decreases. I_0/I is the ratio of fluorescence intensity without quenching to the intensity with quenching at an oxygen partial pressure, and K_q is the rate constant for the quenching process.

Since it is difficult to measure I_0, the Stern-Volmer relation is written in another form shown in eq. (2). The reference is acquired during *in-situ* or *apriori* calibration at ambient conditions to compensate for possible sources of error such as coating thickness, illumination intensity, and temperature. The relationship between the constant K_q and *A* and *B* coefficients are shown in eq. (3). The Stern-Volmer coefficients are also temperature-dependent due to thermal quenching (decreasing luminescence intensity at higher temperatures). The first introduction of PSP as a surface flow visualization technique for aerodynamic flows was accomplished by Peterson and Fitzgerald [10] in the 1980s. Since then, PSP applied to aerodynamic flows was further developed by researchers in the United States and the Soviet Union ([12,13]).

$$\frac{I_0}{I} = \frac{\tau_0}{\tau} = 1 + K_q P_{O_2} \tag{1}$$

$$\frac{I_{ref}}{I} = \frac{\tau_{ref}}{\tau} = B(T)\frac{P}{P_{ref}} + A(T) \tag{2}$$

$$K_q = \frac{A}{B * P_{ref}} \tag{3}$$

The basics of a PSP experiment include an oxygen-sensitive luminophore molecule (Pyrene, ruthenium, or porphyrin complexes) adsorbed in an oxygen-permeable binder matrix. An illumination source (*i.e.*, xenon lamps, LED arrays, or lasers) is required to excite the luminophore within its absorptive spectrum. At the same time, the fluorescence emission is collected by a photodetector (PMT, CCD, or CMOS camera). Once the luminophore is excited to a higher energy state, the energy dissipated is primarily through luminescence (radiation of light energy from the luminophore) and oxygen quenching. The radiation transition from the lowest excited singlet state to the ground state is called fluorescence, and phosphorescence is the radiative transition from the triplet state to the ground state. The emission is at a larger wavelength than the excitation due to Stokes's shift in both cases. Solvent relaxation occurs when there is ample time during the emission process of the excited molecule. Solvent molecules surround the excited molecule, reducing the energy and emitting at a higher wavelength [14].

The photophysical principles of PSP have been well documented ([13,15]). PSP as an optical method of global pressure measurements offers an attractive alternative to conventional pressure measurements. The pixel resolution of the photodetector only limits the spatial resolution of PSP; therefore, PSP is applied in regions of interest that are difficult to measure with conventional sensors. PSP can also identify complex flow structures such as boundary layer separation, transition, and shock waves. With an initial investment of $20,000 to $30,000, PSP is a relatively low-cost alternative to extensive pressure taps, costing $100 per tap [16].

2.2 Fast-responding Pressure Sensitive Paint

Conventional, homogeneous polymer-based PSPs are primarily used for steady-state surface pressure measurements. The timescale of oxygen molecules to permeate the binder and interact with luminescent molecules is a few hundred milliseconds [16]. A fast-responding or unsteady pressure-sensitive paint is more suitable for measuring surface pressure distributions for short-duration or capturing time-varying phenomena. Porous binders increase the mass diffusivity of oxygen and provide a larger air-polymer surface area, facilitating increased interactions between oxygen and exposed luminescent molecules, resulting in broader frequency response. A representation of the comparison between convention polymer binders and porous binders is shown in Figure 2.

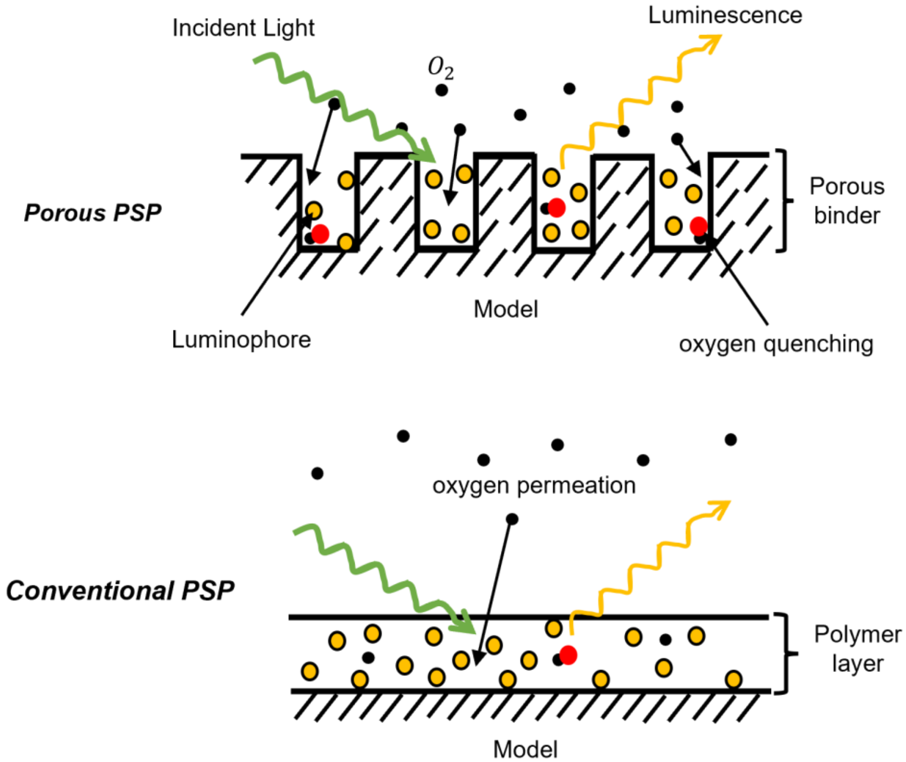

Figure 2: Diagram of oxygen permeation in porous and conventional polymer binders

The PSP's dynamic response depends on both timescales of gas diffusion and luminophore luminescent lifetime. An estimation of the gas diffusion time constant of a very porous PSP is given in eq. (4) [17] where n_{pore} is the number of pores per area and r_{pore} is the mean radius of the pores. Depending on the luminophore, binder, and solvent combination, the luminescent lifetime of PSP is typically between 1-50 micro-seconds at ambient conditions [17]. The diffusion timescale is the primary constraint on the paint's dynamic response, typically much larger than the luminescent lifetime. The three major types of luminophores (porphyrin, Pyrene, and ruthenium) based complexes have relatively short lifetimes (~ 10^{-6} s). The coating thickness h can either be decreased or the mass diffusivity of oxygen (D_m), n_{pore} or r_{pore} can be increased to improve the diffusion timescale. Coating thickness does not only affect dynamic response but also signal-to-noise ratio (SNR), since the luminescent emission is dependent on the thickness of the PSP.

$$\tau_{diff} \propto \frac{h^{2-d_{fr}}}{D_m n_{pore} r_{pore}} \tag{4}$$

There are three main types of porous binders. Anodized aluminum PSP (AA-PSP) uses anodized aluminum as a porous PSP binder. Aluminum is anodized by creating a thin aluminum oxide layer on the surface by an electrochemical process. The coating is highly absorbent, with 10- to 100-nm microspores uniformly distributed on the aluminum surface [17]. Sakaue et al. [18] characterized the response timescales of AA-PSP. With organic luminophores, AA-PSP has a lifetime on the order of 1 ns, and with metal complex luminophores, the lifetime is on the order of 100 ns. Fujii et al. [19] calibrated AA-PSP with a shock tube and measured a 350 ns time constant (over 1 MHz frequency response). Although AA-PSP has the most significant frequency response, the entire model needs to be dipped into a sulfuric acid bath. It also has a weaker luminescent signal, requiring a bright illumination source [20]. Thin-layer chromatography PSP (TLC-PSP) uses a commercial porous silica thin-layer chromatography (TLC) plate as the binder. Although TLC-PSP is commercially available, it is limited to simple geometries due to its brittle nature. Sakaue et al. [21] and Baron et al. [22] demonstrated a response time of 70 µs and 25 µs, respectively, for TLC-PSP.

Polymer ceramic (PC-PSP) is a porous binder that contains hard ceramic particles in a small amount of polymer (~3.5% by weight) [23]. Gregory [16] developed a formulation of PC-PSP that can be sprayed on the testing article, making the application process more convenient than AA-PSP and TLC-PSP for small-scale and large models testing with complex testing geometries. The luminophore can be already mixed with the binder, dipping deposition, or over-spraying a prepared binder surface. Both Bathophen ruthenium and platinum porphyrin have a similar temperature sensitivity from 0.65% to 1.35% per °C and lifetimes when used with a polymer ceramic binder. PC-PSP is also available commercially from *ISSI, inc*. [24]. The pressure sensitivity of platinum porphyrin has a higher value of approximately 0.82% per kPa [25] than Bathophen ruthenium, which has a pressure sensitivity of 0.2% per kPa.

The main factor that impacts the dynamic response of PC-PSP is the ratio of polymer content to hard ceramic particles. Peng and Liu [26] provide a comprehensive summary of state-of-the-art knowledge on fast-responding pressure-sensitive paint. A response time range from 10 μs to 10 s has been tested for a polymer content range of 2.6% to 90% ([25,27–30]). Gregory & Sullivan [27] assessed the effect of quenching kinetics on the unsteady response of the paint. The pressure response of PSP was faster for decay in pressure and slower for a pressure increase. Sugimoto et al. [29] suggested that only luminescent impacted response characteristics. Both the temperature and thickness of polymer/ceramic content had negligible effects. Kameda [31] and McMullen et al. [32] experimentally verified that an accurate first-order and half-order system modeling of a combination of luminescent lifetime and diffusion provided the best fitting.

2.3 Overview of lifetime Pressure-sensitive paint calibration methods

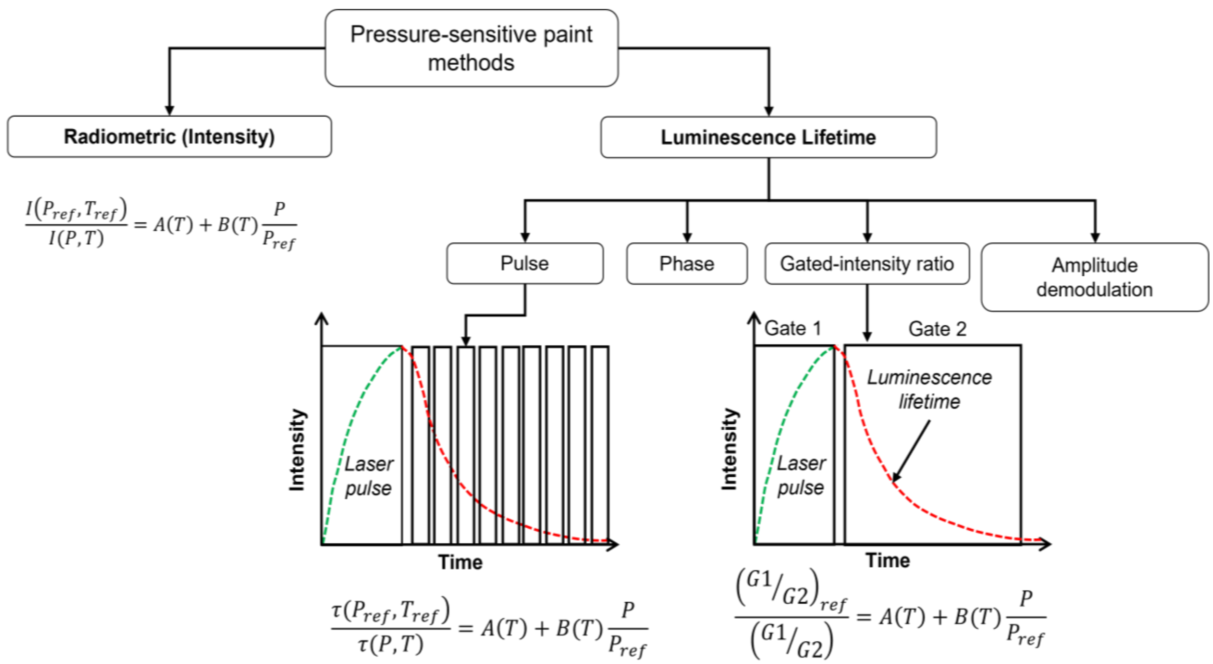

Figure 3: Diagram of Pressure-sensitive paint intensity and lifetime techniques

There are four types of PSP lifetime procedures: pulse, phase, amplitude demodulation, and gated intensity ratio, as shown in Figure 3**.** Liu & Sullivan [15] provide a detailed review of the PSP lifetime technique. The emission *I* response of PSP to a time-varying excitation light source can be modeled by the first-order system in eq. (5). The ideal luminescent decay response becomes a single exponential function for a pulse excitation light. Therefore, the lifetime is defined as intensity decay time to *1/e* or 37% of its initial value. For a general periodic excitation light source (*i.e.*, square, sine, triangle waveforms), the phase angle is related to the luminescent lifetime by eq. (6) [30].

$$\frac{dI}{dt} = -\frac{I}{\tau} + E(t) \tag{5}$$

$$\tan\varphi = \omega_n \tau \tag{6}$$

In the pulse method, after the PSP is excited by a pulsed light source, the luminescent decay is measured using a fast-responding photodetector. The lifetime is calculated by applying a least-squares fitting of the time-resolved data with single or multiple exponential functions [33]. The lifetime, pressure, and temperature are inputs for equations in eq. (7). The system of equations is solved to retrieve the polynomial coefficients *A* and *B*. In a micro-heterogeneous polymer matrix, a multi-exponential luminescent emission decay has been observed in contrast to a single-exponential decay [34].

$$\frac{\tau_{i\,ref}}{\tau_i} = A_i(T) + B_i(T)\frac{P}{P_{ref}}, (i = 1,2, \dots N, N \geq 2) \tag{7}$$

The phase method detects a phase shift between a modulated excitation light and the luminescent signal. A generic period waveform such as a sinusoidal function can be used for excitation. The phase angle between the luminescent emission and excitation light is uniquely related to the lifetime for a fixed modulation frequency by eq. (8).

$$P = K_{sv}^{-1}\left[\frac{\omega\tau_0}{tan\varphi} - 1\right] \tag{8}$$

In the amplitude demodulation method, the lifetime can be obtained from the measurement of the effective modulation index. The equipment required for this method is simple since only the mean and standard deviation of the sinusoidal luminescent intensity and excitation light intensity are needed [15]. A simple formula for the amplitude modulation index, valid only for sinusoidally modulated excitation light, is shown in eq. (9). The optimal modulation frequency is obtained by maximizing the amplitude modulation index to pressure. For a typical PSP, Ru(DPP) in GE RTV 118 with a lifetime of 4.7 μs, the optimal modulation frequency is 41 kHz [15].

$$M_{eff} = \sqrt{2}H^{-1}\frac{std(I)}{\langle I \rangle} \tag{9}$$

The lifetime-gated (Gated-intensity ratio) method is the most widely used lifetime method. The luminescence decay is gated by integrating the intensity over two separate time intervals. A ratio between the integrals is a function of a luminescent lifetime, as shown in eq. (10) with the assumption of a single exponential decay luminescent signal. If the gating intervals and ratios have measurable dependencies on pressure and temperature, both pressure and temperature can be determined simultaneously from gated intensity ratio images. Goss et al. [35] compared phase lifetime, pulse lifetime, and intensity-based PSP. The results showed that the time-resolved multiple-gate method had greater pressure sensitivity than other lifetime and intensity methods.

Schreivogel et al. [10] tested both intensity and lifetime techniques with the flow around isolated surface roughness in supersonic flow. The lifetime technique did not significantly show sensitivity to paint thickness or temperature. Klein et al. [11] compared Light-emitting diode (LED) modulated lifetime and laser single-shot lifetime methods. The LED-based lifetime and laser single-shot method had an error of 200 Pa and 250 Pa, respectively. The measurement error was calculated from the difference between pressure tap and PSP data. The unsteady flow was resolved with the laser-based lifetime measurement system. Sugioka et al. [12] used PC-PSP to measure pressure distribution on a pitching airfoil in transonic flow. The results indicated that the measurement error for lifetime PSP was 50% less than the intensity method.

It is well known that the luminescence lifetime is not constant under uniform temperature and pressure conditions, especially at low speed ([36,37]). Hartmann [37] attributed this result to the microheterogeneity of the polymer matrix, which can induce considerable errors in low-speed PSP measurements. The error caused by the spatial variation in luminescence lifetime was reduced by applying the ratio-of-ratio method (ratio of lifetime ratio at wind-on to reference lifetime ratio at no-flow conditions).

$$\frac{I_1}{I_2} = \frac{\int_{t_2}^{t_3} I\,dt}{\int_{t_0}^{t_1} I\,dt} = \frac{\mathrm{e}^{\left(-\frac{t_3}{\tau}\right)} - \mathrm{e}^{\left(-\frac{t_2}{\tau}\right)}}{\mathrm{e}^{\left(-\frac{t_1}{\tau}\right)} - \mathrm{e}^{\left(-\frac{t_0}{\tau}\right)}} \tag{10}$$

2.4 Review of Relevant Physical Principles

2.4.1 Principles of Luminescence

The luminescence process is described as light emission from any substance from an electronically excited state [14]. Luminescence can be mainly categorized as either fluorescence or phosphorescence, depending on the nature of the excited state. In excited singlet states, the return to the ground state is spin allowed and occurs rapidly by photon emission (fluorescence). Fluorescence typically occurs from organic aromatic compounds with a typical lifetime of approximately 10 ns. The lifetime is the average time between excitation and return to the ground state. The first observation of fluorescence by Sir John F. W. Herschel discovered that a glass of tonic water exposed to sunlight produces a faint blue glow visible at the surface if the glass is oriented at a right angle relative to sunlight [14]. The quinine in tonic water is excited by ultraviolet (UV) light from the sun, and upon return to the ground state, it emits blue light near 450 nm. Other fluorophores encountered daily are green or red-orange glow in antifreeze due to fluorescein or rhodamine.

Phosphorescence is light emission from the triplet excited state. In this case, the electron in the excited orbital has the same spin orientation as the ground-state electron; therefore, the transition to the ground state is forbidden. Phosphorescence lifetimes are slower than fluorescence, typically milliseconds to seconds. In some cases, transition metal-ligand complexes (MLCs) contain a metal and one or more organic ligands and display mixed singlet-triplet lifetimes of 100 ns to several microseconds.

2.4.2 Jablonski diagram

The Jablonski diagram (Figure 4), named after Alexander Jablonski, the father of fluorescence spectroscopy, describes absorption and light emission processes. The singlet ground, first, and second electronic states are defined by S_0, S_1, and S_2, respectively. The fluorophores exist at vibration energy levels depicted by 0, 1, 2, *etc*. A fluorophore is typically excited to S_1 or S_2 states. Internal conversion is rapid relaxation to the lowest vibrational energy level of S_1 and occurs within 10^{-12} or less. Return to the ground state occurs at a higher vibration energy level, quickly reaching thermal equilibrium (10^{-12} s).

A spin conversion of molecules in S_1 state to the first triplet state (T_1) can occur during the intersystem crossing. Phosphorescence is the emission from the triplet state to the ground state, shifted to longer wavelengths (lower energy) relative to fluorescence. The rate constant from triplet emission is several orders of magnitude larger than singlet emission because the transition from T_1 to singlet ground state is forbidden.

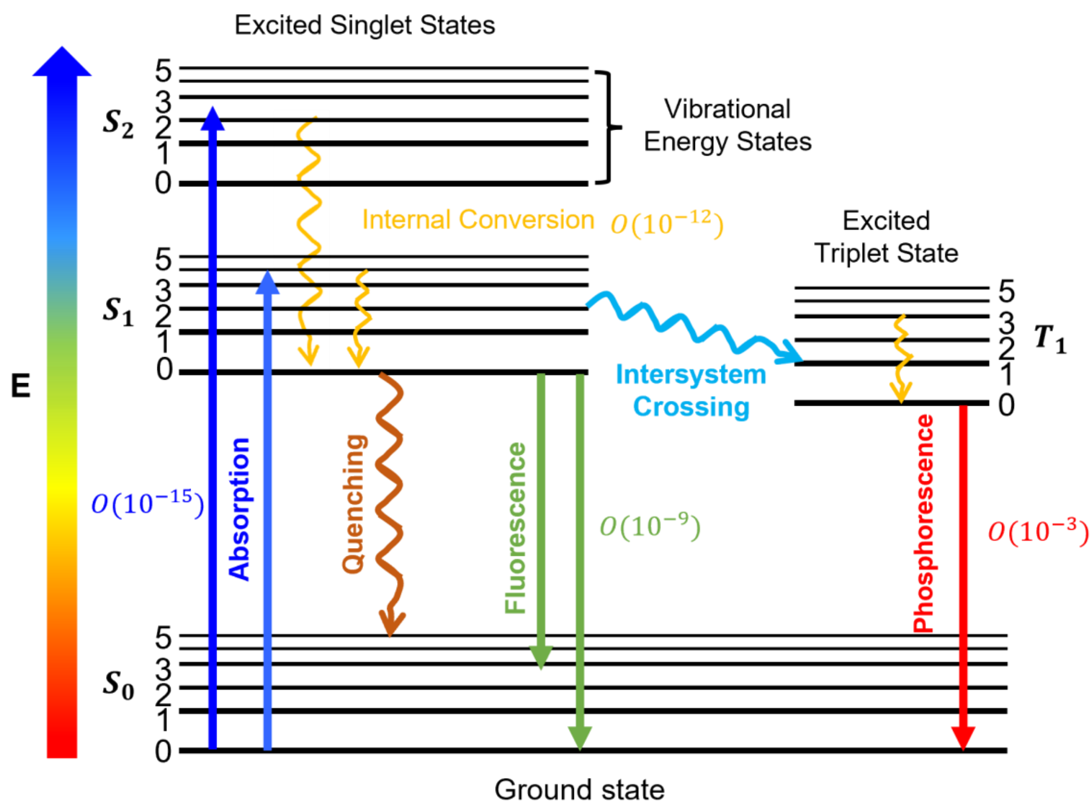

Figure 4: Electromagnetic radiation absorption and emission process described by the Jablonski diagram

The intensity of fluorescence or phosphorescence is decreased by quenching mechanisms such as collisional quenching. When a quencher such as O_2 is in contact with an excited state molecule, the fluorophore returns to the ground state due to a diffusive encounter with the quencher. Equation (1) describes the decrease in intensity by the quencher. Fluorophores can also form non-diffusive interactions with quenchers in the form of static quenching (non-fluorescent complexes with quenchers). In contrast to absorption, which is an instantaneous process, emission occurs over more extended periods, providing an opportunity for the fluorophore's interactions with quenchers in the solution.

The Jablonski diagram shows that the emission occurs at a longer wavelength (lower energy) than the absorption. The energy losses between excitation and emission can be almost less than 50% [14]. Another property of fluorescence is that the emission spectrum is independent of the excitation wavelength. The fluorescence emission process is random, and few molecules emit their photons precisely at $t = \tau$. The lifetime is defined as the average time the molecule spends in the excited state before returning to the ground state. Only 63% of molecules have decayed before $t = \tau$ for a single exponential decay model.

CHAPTER 3: DEVELOPMENT OF A PULSE LIFETIME PSP CALIBRATION PROCEDURE

This chapter investigates a systematic evaluation of the pulse lifetime calibration method by manufacturing and testing a pressure chamber operated under vacuum and above atmospheric pressure with optical access to excite and capture the fluorescence of a sample PSP coupon. The calibration results are analyzed to evaluate the accuracy, reliability, and uncertainty of the pulse lifetime method.

3.1 Luminophore molecule and binder

A PtTFPP luminophore with a polymer ceramic binder from *ISSI*, Inc. [24] was used for calibration and wind tunnel experiments. The paint formula has three components: Parts A and B make up the binder, and Part C is the luminophore solution. Part A's volume is determined based on the interrogation region of interest and paint thickness required for the experiment. A graduated cylinder and syringe are used to measure 4% of Part A from Part B. Parts A and B are combined in a jar with a tight lid and shaken thoroughly. An *Iwata* airbrush precise for fine and coarse brush painting is used to apply several coating layers of the binder mixture until the required thickness is achieved. After coating the binder *in situ*, the paint is dried at room temperature for an hour. Finally, part C is poured into a thoroughly cleaned airbrush and sprayed on top of the binder until uniformly pale pink.

The absorptive spectrum of the paint has peak efficiencies at the Soret band (395 nm) and Q-band (541 nm), and the emission spectrum has a peak efficiency near 650 nm. The absorption and emission of PtTFPP from Sullivan [20] are shown in Figure 5**.** A spectrometer was used to measure the fluorescence after excitation with an Nd: YAG laser (532 nm). The spectrometer was manually calibrated with Ne-Hg lamps within Hg and Ne wavelength spectrums. An iterative process with a flashlight was used to check that a 2-3 nm resolution was met with the spectrometer slit opening distance while maintaining signal intensity. The results from the spectrometer experiment shown in Figure 6 confirm the emission spectra wavelength of PtTFPP using a 532-notch filter at ambient pressure.

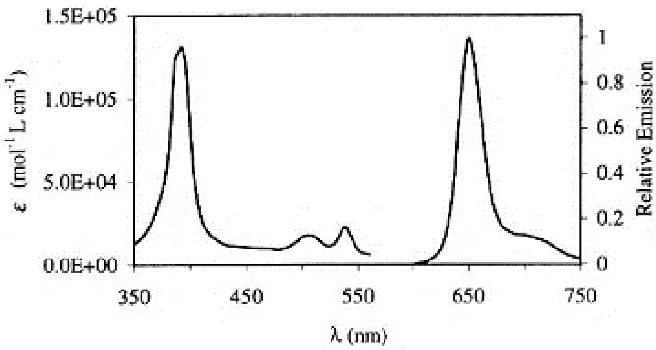

Figure 5: Absorption and emission spectrum of PtTFPP [20]

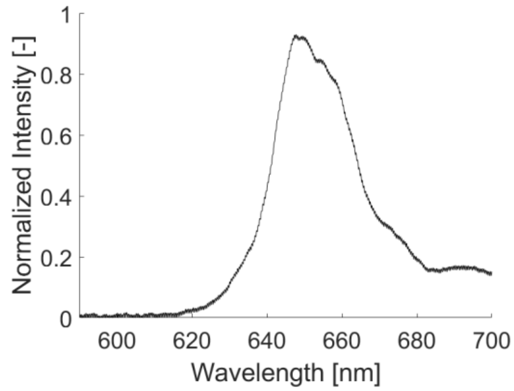

Figure 6: Emission spectrum of PtTFPP measured with a spectrometer

3.2 Illumination source

Traditionally, the lifetime-based technique requires a modulated light source (*i.e.*, laser, modulated LEDs, or flash lamps). A state-of-the-art quasi-continuous burst-mode Nd: YAG laser following the design of Slipchenko et al. [38] was used as a light source to excite the paint at 532 nm (2^{nd} harmonic output of the laser). The high energy output of the laser makes it suitable for high-speed surface imaging [39] and planar imaging of unsteady flows [40]. High-frequency lasers, such as quasi-continuous burst mode lasers, output a very high repetition rate with a short burst duration due to high voltage capacitor banks cooling requirements.

The laser has a linewidth of < 2 GHz at 1064.3 m with 215 mJ/pulse at 20 kHz. The pulse burst duration is 10.8 milli-seconds with nominal repetition rates at 10 kHz and 20 kHz. The pulse burst duration is extended by one order of magnitude compared to previous flashlamp-pumped designs due to the addition of a fiber oscillator and diode-pumped solid-state amplifiers. The maximum excitation of the paint is limited to 20 kHz, which provides a window of 50 µs to capture the fluorescence decay of the luminophores at ambient pressure between laser pulses. The paint has a longer decay lifetime at lower pressures, with a time between each laser pulse of 100 µs near-vacuum. The duration of the intensity decay to 99% of its initial value at the lowest calibration pressure determines the time between each laser pulse [14]. A spherical diffuser and a plano-convex focusing lens produce a closely elliptical uniform laser beam spot on the test article.

3.3 Photodetector

A fast-shutter camera is required to capture the luminescent lifetime with high spatial resolution fully. An intensified charge-coupled device (CCD) or interline transfer CCD camera is typically used to collect the excited luminescent decay for the gated-intensity ratio approach. Compared to the intensity method, the lifetime method has relatively lower luminescent intensity; thus, the exposure time is increased to improve the SNR. However, since the ICCD cameras have higher noise levels than the CCD, a coupled image intensifier is used for shorter gating times. Most CCD cameras utilize the double exposure method to acquire two or more gates during a single excitation pulse. The first gate is during the laser pulse and has a shorter gate width and the second gate usually has exposure times of milliseconds. The pulse lifetime approach requires a highly sensitive, high-speed photodetector such as a CMOS (complementary metal-oxide-semiconductor) camera. A CMOS sensor has faster frame rates because each pixel has an amplifier and converts the charge to voltage. However, it also has lower sensitivities and is noisier than CCD cameras because of the smaller active pixel area. An intensifier can be coupled with a CMOS camera to improve the sensitivity, especially in applications where the signal of the excited luminescent decay is not significant.

3.4 Pulse lifetime calibration setup

A calibration chamber was designed and manufactured to evaluate the pulse lifetime calibration method. A high-speed camera with sufficient spatial resolution repeatedly samples the intensity decay after the pulse excitation until the entire decay is measured. The pressure chamber, shown in Figure 7**,** is operated under vacuum and above atmospheric pressure with optical access to illuminate and capture the fluorescence of a sample PSP coupon. The optical setup, shown in Figure 8, shows the path of the laser beam through a series of 532 Nd: YAG mirrors, including a 25.4 mm Plano-convex focusing spherical lens and a 25.4 mm, 1500 grit ground glass diffuser for a uniformly diffused 38 mm diameter region of interest (ROI). A 532-notch filter is attached to the camera lens to cut off any reflections from the laser beam and capture the peak luminescent emission at 650 nm. Additionally, the inner chamber was spray-coated with a black matte paint to reduce the reflections of the laser beam on the metal surface. A 50.8 mm aluminum disc coupon was spray-coated with PC-PSP and mounted in the calibration chamber to evaluate the lifetime method.

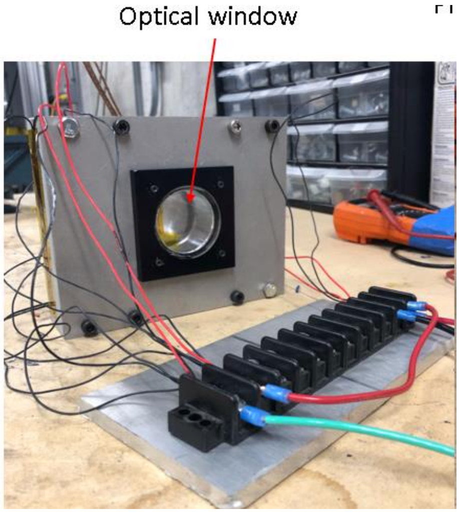

Figure 7: Pressure calibration chamber

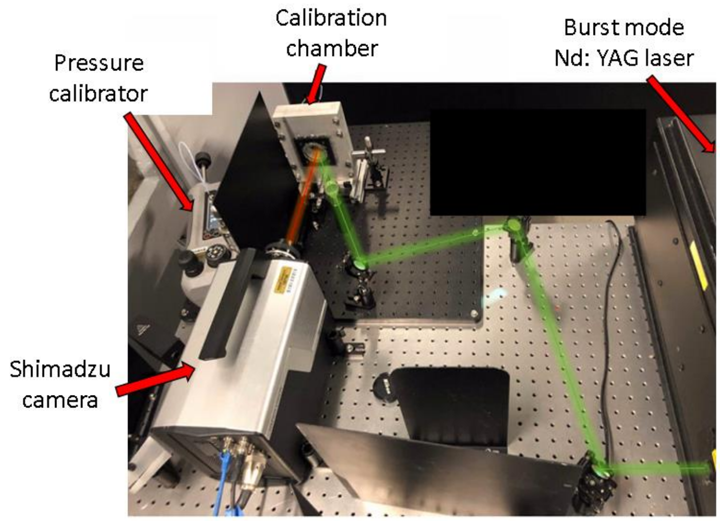

Figure 8: Pulse lifetime calibration optical setup

The sequence of the pulse lifetime calibration is as follows: a *GE DPI 610* pressure calibrator connected to the calibration chamber is used to set a uniform pressure with an accuracy of 0.025% of the full-scale 689.48 kPa pressure range. A *Quantum Composer, 9530 pulse delay generator*, sends a trigger output signal to start the laser pulse train and set the timing sequence shown in Figure 9. The laser has a repetition rate of 20 kHz and burst duration of 2 milliseconds, and each pulse has a 10 ns width. The camera is synchronized with the laser in duty cycle mode to sample at 400 kHz and acquire 20 images after each laser pulse with a 10 ns delay to avoid image saturation by the laser. A total of 240 images are recorded for each calibration pressure due to a memory limit of the *Shimadzu HPV-X2* high-speed camera. The acquisition details of the experiment are summarized in Table 1**.**

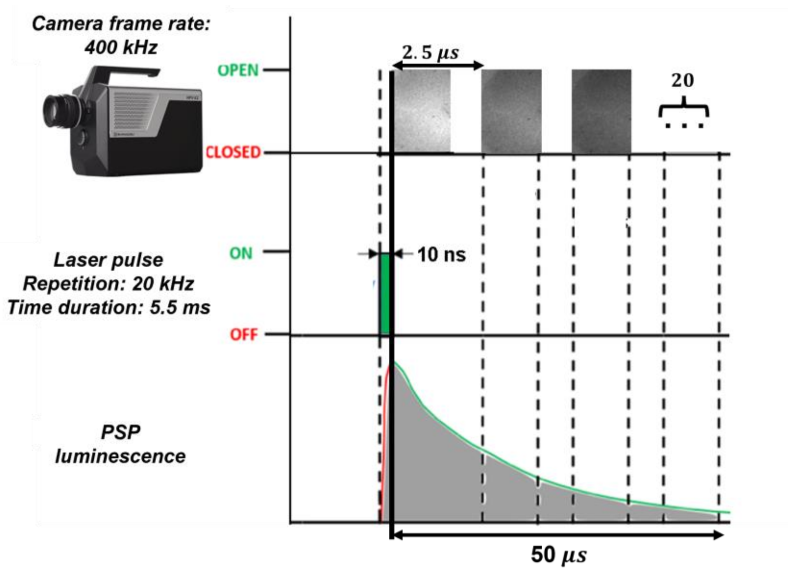

Figure 9: Timing sequence for pulse lifetime method

Table 1: Pulse lifetime calibration settings

PC-PSP calibration settings	
Quasi-continuous burst mode Nd: YAG laser	20 kHz [2 ms pulse duration] every 10 sec
Shimadzu HPV-X2 camera	400 kHz (2 µs exposure)
Images per laser pulse	20 [50 micro-sec capture time]
Excitation/emission wavelength	532 nm / 650 nm
Optical filter	532 notch filter
Calibration points	15
Datasets	12 [240 images per dataset]

3.5 Precise measurements of PSP thickness

The PSP coating thickness directly relates to the intensity, time response, temperature dependency, and pressure sensitivity. A thin layer of PSP yields a faster response to a pressure change at the expense of reduced SNR; however, the intensity signal from PSP is saturated with too much paint thickness. Moreover, highly porous, oxygen permeable binders such as the polymer ceramic binder used in these experiments have a weaker luminescence of the PSP at the ambient conditions, leading to low SNR than non-porous polymer binders. In general, to minimize roughness and aerodynamic effects on the testing apparatus, a typical roughness coating should be less than 0.25 µm, and coating thickness should range between 20 – 40 µm [15]. Hayashi and Sakaue [41] experimented with polymer-ceramic binder-based PSP by varying the paint thickness from 10 to 240 µm. Temperature, time response, signal level, and pressure sensitivity effects were uniform over 80 µm. At a thickness of 80 µm, the average pressure sensitivity and time response were approximately 0.55%/kPa and 46 µs, respectively.

A *Dualscope FMP40C* system with an *FD13H* spring-loaded measurement probe was used to precisely measure the PSP coating thickness. The *FD13H probe* can be used as magnetic inductive for ferrous metals or eddy current for paint, varnish, or plastic coatings applied on non-ferrous metals. A coil wrapped around the ferrite core is induced with an excitation current for the eddy current test method. The generated high-frequency magnetic field sends loops of electrical current into a base material in planes perpendicular to the magnetic field. The resulting magnetic field signal's obtained measurement is converted to a coating thickness value with an accuracy of 2% of the nominal value. The probe tip is made up of a hard metal material and has a diameter of 4 mm.

A corrective calibration procedure is applied before each thickness measurement. First, the uncoated or unpainted base material (aluminum) is measured by the probe five times in the same approximate area. After the calibration of the base material, two standard thin calibration foils with a precise thickness rating are placed on the unpainted material. Both thin foils are measured five times each to complete the corrective calibration. After the calibration procedure, multiple areas of the PSP coating are measured, as shown in Figure 10, for a total of 1071 data points. The thickness across the entire PSP coupon surface is shown in Figure 11. The total measurements' average value and standard deviation are 58.68 ± 6.59 µm. The uncertainty reported for the average value is within the 95% confidence interval. The coefficient of variation of 11.2% results from non-uniform spray painting of the binder and luminophore topcoat. Figure 12 represents the thickness measurements from one edge of the PSP coupon to the opposite edge. A total of 10 data points were acquired at 13 measurement locations along the line. Based on the probe's outer diameter, each measurement area has a diameter of 13 mm. The results indicate that the coupon edges have a relatively larger thickness variation than the coupon's center.

Figure 10: Eddy current probe used to measure PC-PSP coating thickness

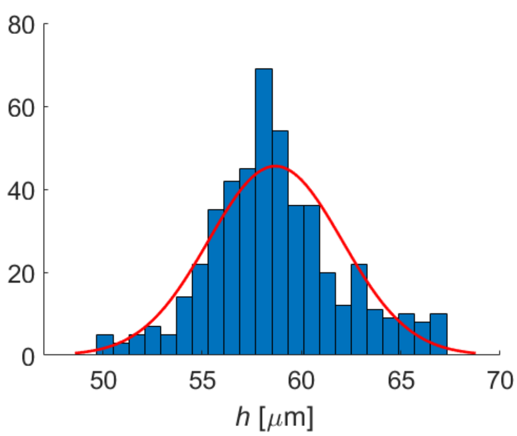

Figure 11: Histogram of thickness measurements on PSP coupon

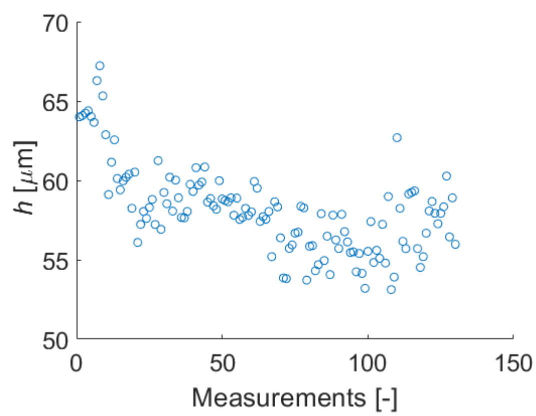

Figure 12: Thickness measurements along a straight line between coupon edges

3.6 Spatial intensity and lifetime variation

The intensity signal and lifetime variations are corrected by ratioing a wind-off (reference) to the wind-on image at constant pressure and temperature. Figure 13 and Figure 14 show the non-uniform distribution of lifetime at a constant pressure of 23.4 kPa and 102.94 kPa (reference condition), respectively. The lifetime is calculated for each pixel, assuming a single exponential decay. An example of ratio correction is applied by dividing the lifetime at 24 kPa by the lifetime at reference condition, as shown in Figure 15. Without the ratio correction, the coefficient of variation of the lifetime at 23.4 kPa and 102.94 kPa are 3.2% and 2.86%, respectively. After the ratio correction, the difference is reduced to 1.07%. The decrease in lifetime towards the center of the image shown in Figure 13 and Figure 14 is consistent with the PSP thickness measurements in Figure 12. A reduced coating thickness corresponds to a reduced diffusion timescale and shorter luminophore lifetimes. Figure 16 and Figure 17 show the non-uniform intensity map at a constant pressure of 23.4 kPa and 102.94 kPa. Without the intensity ratio correction shown in Figure 18, the relative standard deviation at 23.4 kPa and the reference condition is 15.3% and 15.88%, respectively. The variation is reduced to 1.12% with the ratio correction, which is considerably improved by 14. Without any modification, it is evident that the lifetime method is less sensitive to non-uniform illumination, thickness, or dye concentration compared to the intensity signal.

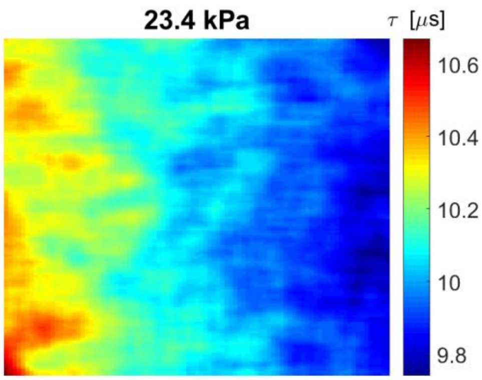

Figure 13: Single exponential decay lifetime distribution at 23.4 kPa

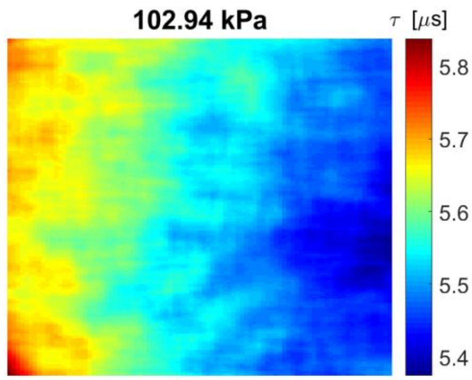

Figure 14: Single exponential decay lifetime distribution at 102.94 kPa (reference)

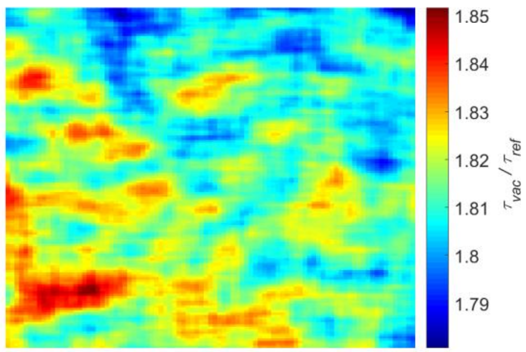

Figure 15: Ratio of lifetime at vacuum to reference pressure

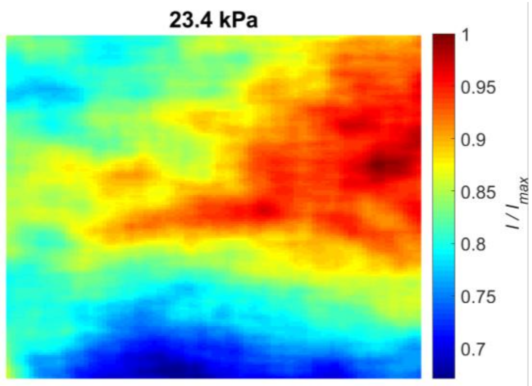

Figure 16: Intensity signal distribution at 23.4 kPa

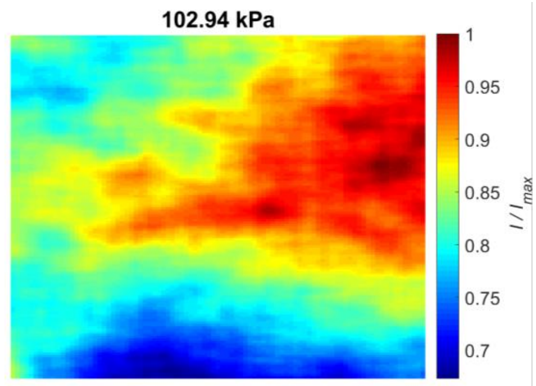

Figure 17: Intensity signal distribution at 102.94 kPa

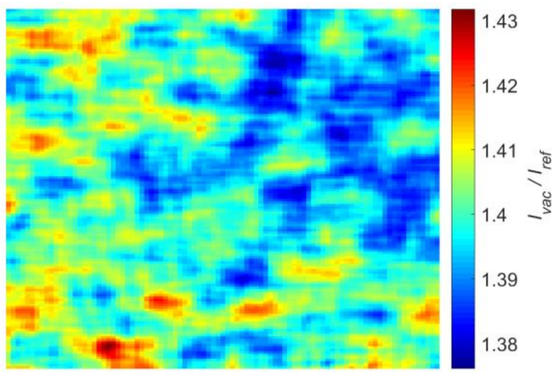

Figure 18: Ratio of intensity signals at vacuum to reference pressure

The minimum difference intensity variation at 23.4 kPa and the reference condition implies that the laser intensity and beam profile are consistent at different calibration pressures. The increased intensity magnitude at the lower calibration pressure is mainly due to the change in oxygen concentration and the interaction of the oxygen molecules with the excited luminophores. The maximum intensity near the center of the PSP coupon is comparable in shape to the signal intensity of the laser beam profile shown in Figure 19**.** The laser beam spatial shape is near Gaussian, with some low-intensity regions extending out from the central portion of the beam. While the energy per pulse changes for different repetition rates, the spatial beam profile does not depend on the laser repetition rate or temporal pulse shape for specific flash lamp energy, burst duration, and burst period [42]. Dye concentration or thickness is not the main contributor to intensity signal change between the two calibration pressures for the following reasons: 1) insignificant difference of coefficient of variation between 23.4 kPa (low O_2 diffusion), and reference condition (high O_2 diffusion) Additionally, locations on the PSP coupon with increased coating thickness should correspond to increased signal intensity unless too much coating of PSP is applied; however, Figure 16 shows the opposite trend.

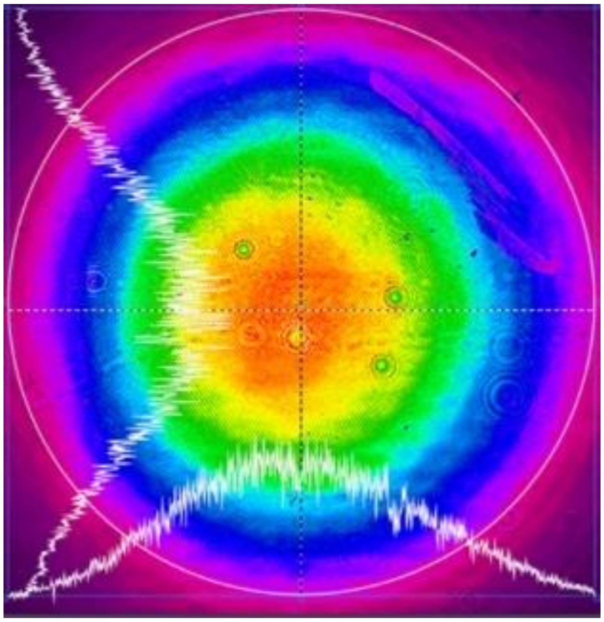

Figure 19: *Quasimodo* laser beam profile

3.7 Fluorescence decay curve fit analysis

The fluorescence lifetime is one of the essential characteristics of a luminophore. The lifetime of an excited state is the average time a molecule spends in an excited state before returning to the ground state [14]. In eq. (11), the intensity decay is modeled as an ideal luminescent decay response to a pulse illumination. For a single exponential decay, 63% of molecules have decayed before $t = \tau$ and 37% decay at $t > \tau$ [14].

$$I(t) = I_0 e^{-\frac{t}{\tau}} \tag{11}$$

The normalized intensity decay at three different calibration pressures from 23.4 kPa to 199.94 kPa is shown in Figure 20. The normalized intensity data are averaged over all pixels into a single value. The abscissa represents the duration of the camera exposure between each laser pulse. Fast intensity decays at higher pressures are a direct result of oxygen quenching. The normalized intensity decay is also displayed on a logarithmic scale shown in Figure 21 with data from images 2, 3, and 4. The average lifetime and coefficient of determination for each laser pulse over time are shown in Figure 22 and Figure 23**,** respectively. The averaged lifetime and goodness of fit are consistent over a time interval of 0.55 milliseconds. Moreover, the coefficient of determination with a single exponential decay model was above 0.993 for all calibration pressures, as shown in Figure 24**.**

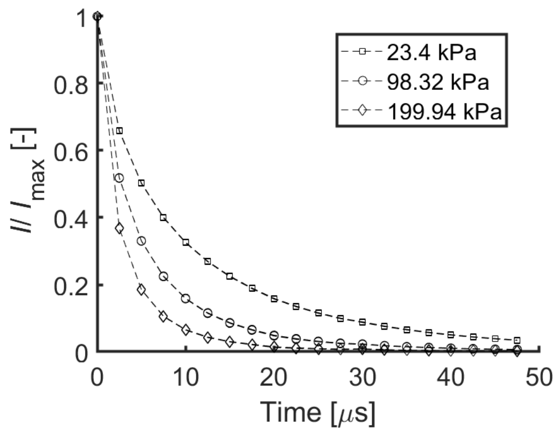

Figure 20: Normalized intensity decay

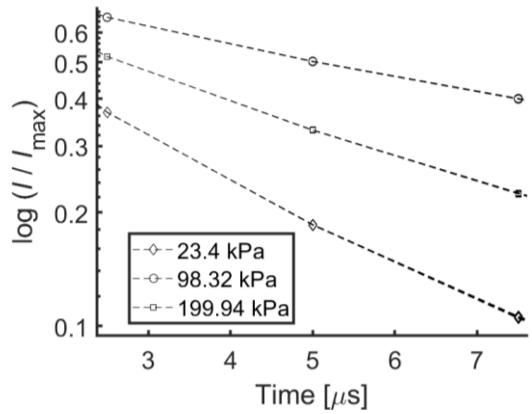

Figure 21: Logarithmic normalized intensity decay

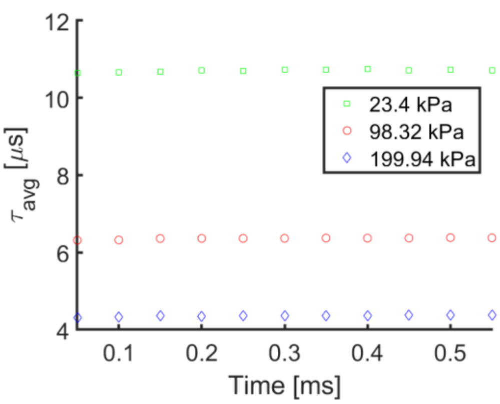

Figure 22: Average lifetime over the laser pulse duration

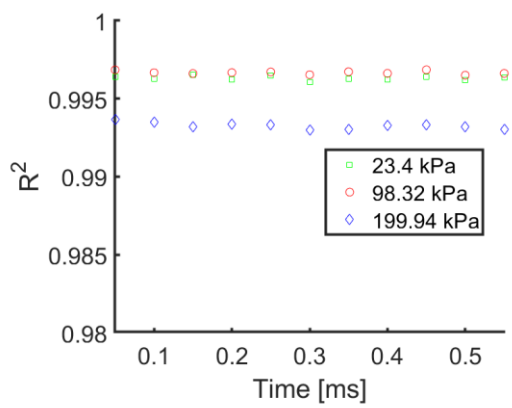

Figure 23: Coefficient of determination for each laser pulse

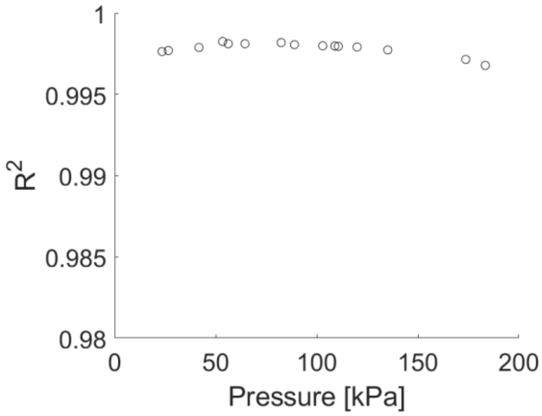

Figure 24: Coefficient of determination for each calibration pressure

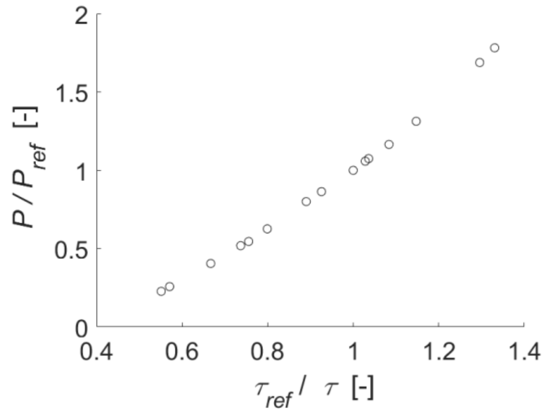

Figure 25: Normalized calibration pressure and normalized calculated lifetime

Ideally, the relationship between pressure and lifetime is linear according to the Stern Volmer model for a single excited-state lifetime with homogeneous quenching. However, static and dynamic quenching contribute to a non-homogenous environment where O_2 can exist at various sites with its characteristic quenching constant. From the calibration data, the trend of normalized pressure and lifetime is shown in Figure 25 and expressed by a second-order polynomial in (12). Each pixel or bundle of pixels (if binning is applied) has unique coefficients (C_1, C_2, and C_3) that correlate lifetime to pressure. The lifetime variation at constant pressure is propagated into the variability in the 2nd order polynomial coefficients shown in Figure 26. The histogram represents the coefficients from all the pixels. The histogram of the coefficient of determination indicates that the quadratic formula is an acceptable fit for the regression data in Figure 27. The coefficients from eq. (12**)** are applied to the lifetime calibration data to retrieve the reconstructed pressures from the PSP. The relative difference between the calculated pressure and calibrator set pressure is shown in Figure 28. The maximum relative difference is less than 2%.

$$\frac{P}{P_{ref}} = C_1\left(\frac{\tau_{ref}}{\tau}\right)^2 + C_2\left(\frac{\tau_{ref}}{\tau}\right) + C_3 \tag{12}$$

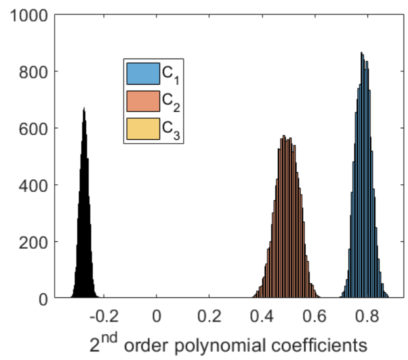

Figure 26: Histogram of 2nd order polynomial coefficients

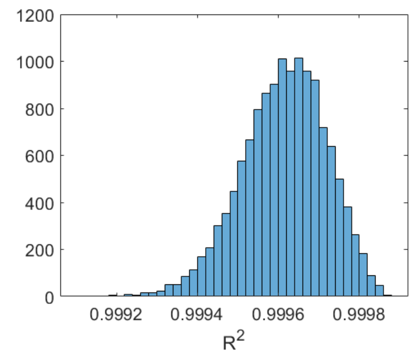

Figure 27: Histogram of the coefficient of determination for 2nd order polynomial

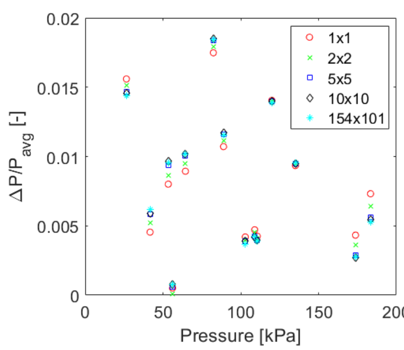

Figure 28: Relative error between reconstructed PSP pressure and reference pressure calibrator

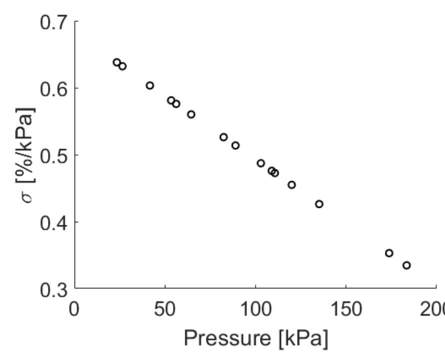

Figure 29: Pressure sensitivity as a function of the calibration pressure

3.8 Pressure sensitivity and signal to noise ratio

The pressure sensitivity is the minimum pressure resolution for a percent change in lifetime or intensity. The first derivative of eq. (12) with lifetime as the independent variable was used to calculate the pressure sensitivity defined in eq. (13). A linear relationship between pressure sensitivity and calibration pressure is shown in Figure 29. The pressure sensitivity is more significant at lower pressures due to less oxygen quenching.

$$\delta = \frac{d\left(\frac{\tau_{ref}}{\tau}\right)}{dP} \ [\%/kPa] \quad (13)$$

The signal-to-noise ratio (SNR) is computed as the logarithmic ratio of an average lifetime to the standard deviation of the lifetime as shown in eq. (14). The trend of signal-to-noise ratio for each calibration pressure is described in Figure 30**.** There is a gradual increase in SNR from minimum pressure to ambient pressure. Although the mean value of the lifetime is larger at low pressures, the variation has a larger effect on the SNR from low pressure to ambient pressure. Beyond ambient pressure, the SNR is almost constant. Since the luminophore molecules are quenched at ambient pressure, there is no relative change in SNR at higher pressures because of signal saturation and reduced pressure sensitivity.

$$SNR = 20\log_{10}\left(\frac{\mu_{signal}}{\sigma_{signal}}\right) \tag{14}$$

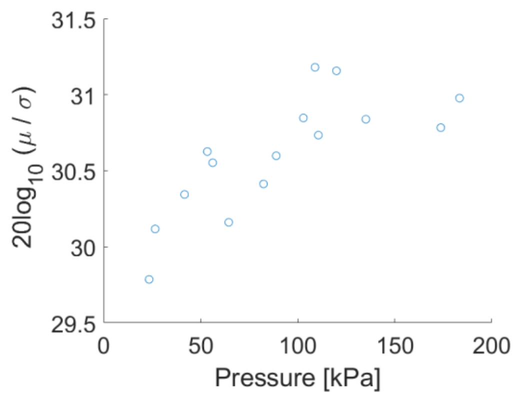

Figure 30: Signal to noise ratio as a function of calibration pressure

3.9 Summary

The following is a summary from systematic evaluation of the pulse lifetime technique: 1.) An additional high accuracy reference sensor is required to measure static pressure and should be synchronized with the high-speed camera to reduce the difference between PSP and reference pressure. 2.) A 610 nm long-pass filter is adequate in filtering out incident laser reflections and provides enough signal of the fluorescence emission of PSP. A 532 nm notch filter may be used in addition to achieving an even better luminescence signal from the PSP. 3.) A quasi-continuous burst mode Nd: YAG 532 nm laser is adequate to excite the PtTFPP oxygen-sensitive dye 4.) A high-speed camera with sufficient spatial resolution and memory should be used to increase the number of useful laser pulses during the burst duration 5.) A single exponential decay regression can be used to model the luminescence decay of PtTFPP 6.) A second-order polynomial regression can be used to model the relationship between normalized lifetime and pressure.

CHAPTER 4: DEMONSTRATION OF PULSE LIFETIME PSP IN A SUPERSONIC TEST SECTION

This chapter demonstrates the pulse lifetime PSP method in a linear test section (TRL 1-2) with a supersonic test article. Three test conditions of increasing mass flow are assessed to evaluate the capability of measuring pressure fluctuations. The overall measurement uncertainty and error propagation of the pulse lifetime PSP method is assessed. A data processing methodology is applied to remove images with a low signal-to-noise ratio, reduce uncertainty, use image resectioning and select an optimal binning bundle of pixels for spatial-temporal pressure analysis. A sensitivity analysis of the calibration method is performed to find the parameters with a substantial effect on final pressure uncertainty.

4.1 Facility Operation

As shown in Figure 31, the linear test section is mounted in a wind tunnel at the Purdue Experimental Turbine Aerothermal Lab (PETAL) [43]. The high-pressure piping upstream of the settling chamber is connected to air tanks at Zucrow labs that contain 56 m^3 compressed dry air at 15 MPa. The exhaust of the wind tunnel is connected to a vacuum tank (280 m^3) located outside the test cell. A *Dekker* vacuum pump attached to the exhaust pipeline can reduce the pressure to as low as 30 mbar in the test section.

Figure 31: Wind tunnel with the linear test section mounted

The facility operation schematic is illustrated in Figure 32. Before the flow experiment, the vacuum pump is used to set the pressure in the linear test section from atmospheric pressure to 16 kPa to complete the calibration of the PSP. Once the required vacuum level in the test section is achieved, a control valve regulates air from the high-pressure reservoir into the test cell. Flow is guided through the cold line and a critical flow venturi for accurate mass flow rate measurements. The purge line sets the mass flow to the correct rate. Once the desired conditions are met, a fast butterfly valve upstream of the linear test section is opened, and the purge valve is closed. The natural gas heat exchanger is not used for these experiments since all tests were at cold conditions. The air is radially discharged into a settling chamber before passing through honeycombs and flow straighteners. The flow is then accelerated through the inlet contraction area and released into the test section with uniform spatial and temporal flow conditions. At the end of the experiment, the test section valve opens, and the pressure equalizes to atmospheric pressure.

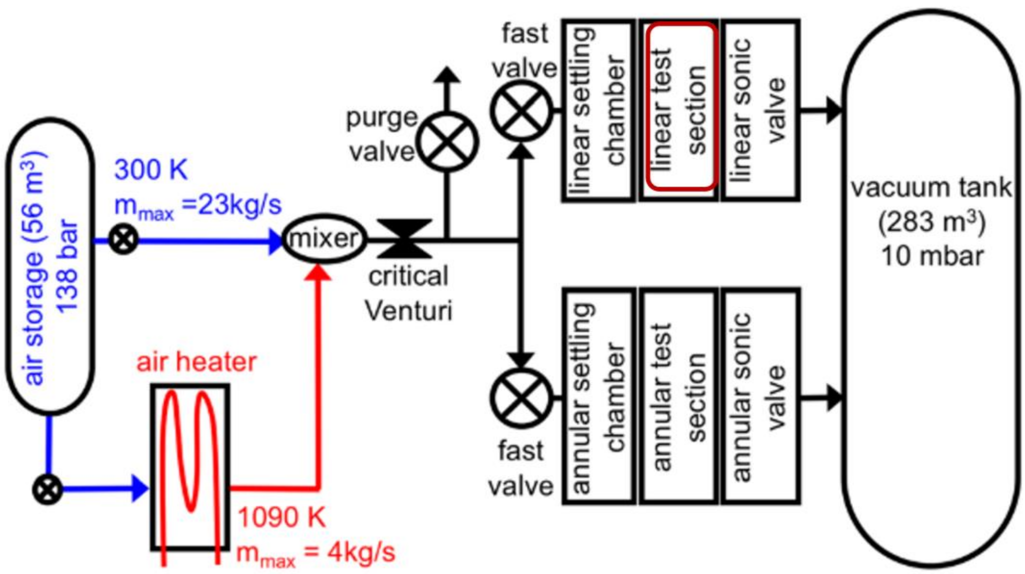

Figure 32: Facility operation with a supersonic test article mounted in a linear test section

4.2 Optical Setup

The linear test section was designed to be fully optical accessible with removable fused quartz windows and modular for rapid interchange of test models. The supersonic test article mounted in the linear test section is shown in Figure 33. The outer metal frame of the linear test section holds four large quartz windows. Quartz-to-quartz contact defines the test section's inner geometry, making it ideal for evaluating novel optical measurement techniques. The optical path for the laser

Figure 33: Supersonic test article mounted in the linear test section

beam and camera mounting position is shown in Figure 34a. The laser beam was guided through a series of Nd: YAG mirrors and a 1500 grit diffuser lens to provide uniform illumination on the wavy surface. A *SAZ Photron* CMOS camera was sampled at 200 kHz with a 160x384 spatial resolution to capture the fluorescence decay. A 532 nm notch filter and 610 nm long-pass optical filter were installed to dampen the incident laser reflections. The test case consists of a converging-diverging nozzle accelerating the flow to Mach 2, followed by a wavy surface to study shock-separation phenomena, as depicted in Figure 34b. Due to high spatial gradients, the test article is suitable for precisely evaluating optical diagnostics for unsteady applications [15]. Both steady and unsteady PSP data are compared with conventional instrumentation (low & high-frequency pressure sensors) and Computational Fluid Dynamic (CFD) simulations to validate the pulse lifetime PSP method.

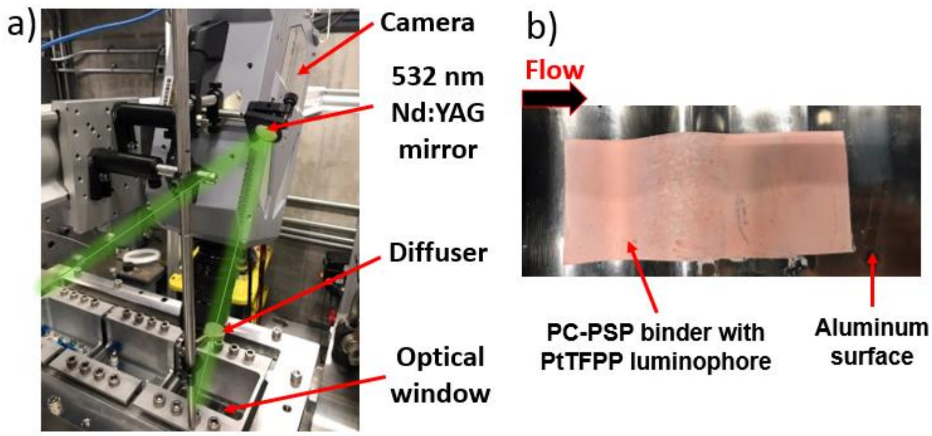

Figure 34: a) Top-down view of the optical setup for PC-PSP evaluation in PT1
b) PC-PSP sprayed on the wavy surface

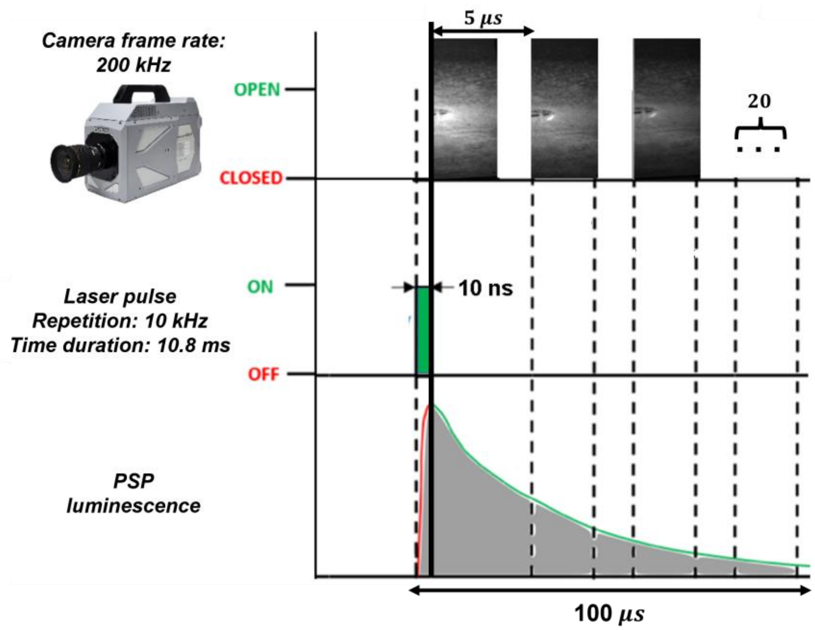

Figure 35: Laser and camera timing sequence

A vacuum pump connected to a downstream exhaust duct set pressures in the test section from 101.15 kPa to 16.34 kPa for the PSP calibration. A total of 14 calibration points were acquired within the pressure range. At each pressure, a TTL pulse from a *Quantum Composer 9530* pulse generator sends a trigger signal with a negligible pulse generator jitter of 250 ps to start the timing sequence of the experiment shown in Figure 35. The laser has a repetition rate of 10 kHz and a pulse burst duration of 10.8 ms, which yields 108 datasets for each calibration point. The camera acquires 20 images at 200 kHz between each laser pulse with a 3.4 µs exposure for a total acquisition time window of 100 µs. *Scanivalve DSA 3217* pressure scanners measure the static pressure in the wind tunnel to an accuracy of ± 173 Pa and are used as a reference pressure to calibrate the PSP.

4.2 Pulse lifetime PSP data processing routine:

A data post-processing routine shown in Figure 36 was implemented to remove data with low SNR, reduce uncertainty, and select the optimal binning for flow-field analysis. A background image is acquired without laser excitation for camera sensor noise subtraction. The raw images are cropped to an 84x347 pixel ROI, and each calibration pressure value is reshaped from a single

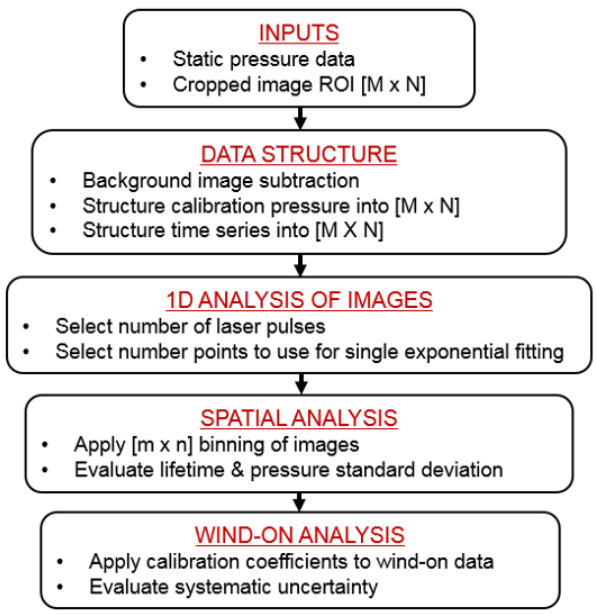

Figure 36: Schematic of the data processing routine

value into an 84x347 matrix. Additionally, the 1-D time interval vector of the camera exposure between each laser pulse is structured into an 84x347 matrix. For the 1-D image analysis, all the pixels are averaged into a single averaged value. The fluorescence decay is measured 20 times, and each point is normalized by the first point, which is at maximum intensity. The normalized intensity decays rapidly (shorter lifetime) for all 108 datasets at 101.15 kPa than at 56.33 kPa and 18.41 kPa due to less oxygen quenching at lower pressures, as shown in Figure 37. The trend of a shorter lifetime at higher pressures is consistent with the rest of the calibration data not shown. For all 108 datasets, a threshold of 0.9 is applied for the maximum calibration pressure and 0.01 for the minimum calibration pressure. If the first point after the laser pulse is less than 0.9 and the last point is greater than 0.01, the dataset is discarded as an outlier. Out of 108 datasets, 99 datasets are selected and shown in Figure 38 on a logarithmic scale. The outliers removed from the initial 108 datasets are primarily from the initial start-up and ramp-down of the burst mode laser. A focus on the first eight points of the normalized intensity decay in Figure 39 depicts an excellent linear trend. Thus, a single exponential decay is an appropriate model for calculating the lifetime.

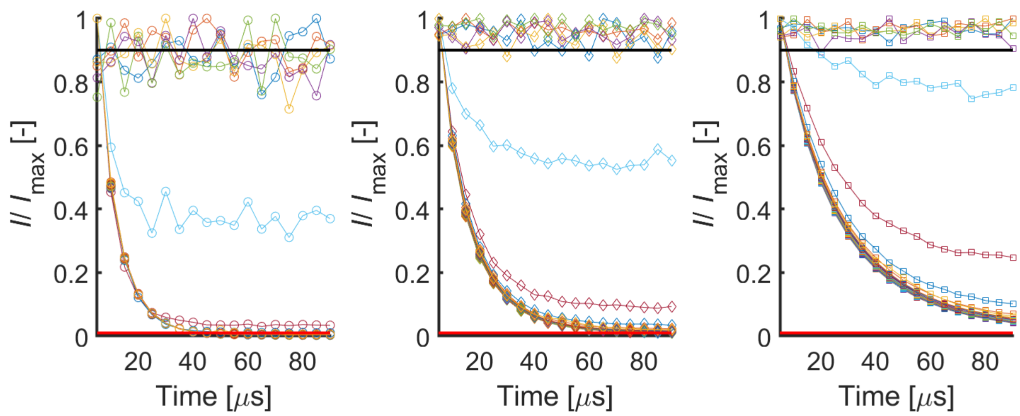

Figure 37: Normalized intensity decay at 101.15 kPa (left), 56.33 kPa (middle), and 18.41 kPa (right)

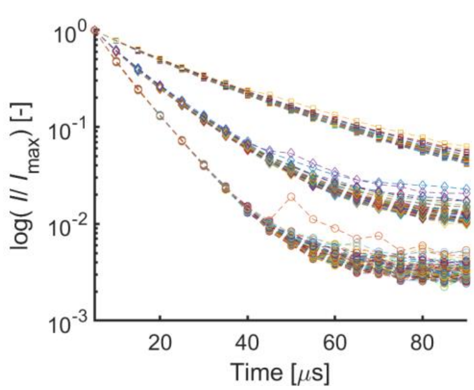

Figure 38: Logarithmic normalized intensity decay: top (101.15 kPa), middle (56.33 kPa), bottom (18.41 kPa)

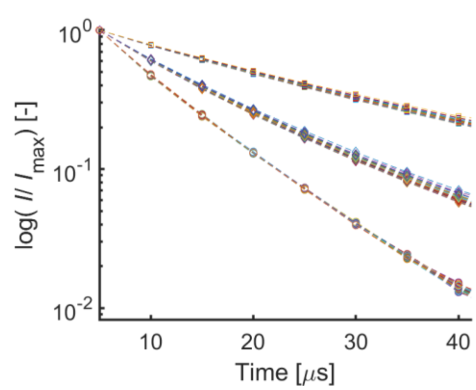

Figure 39: Logarithmic normalized intensity decay of first 8 points: top (101.15 kPa), middle (56.33 kPa), bottom (18.41 kPa)

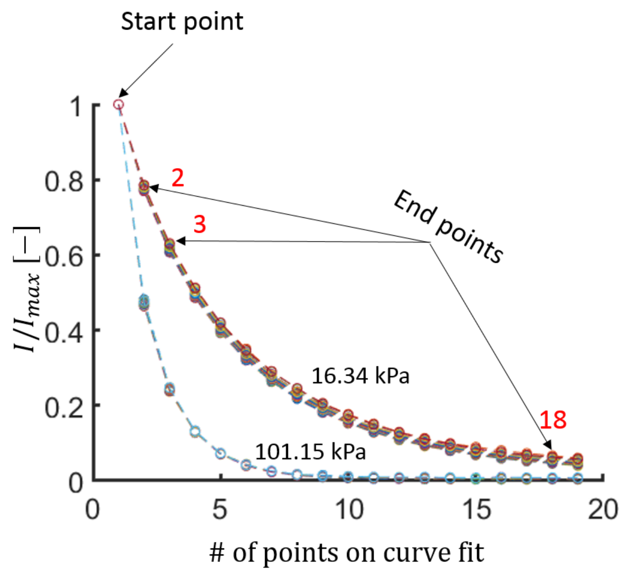

Figure 40: Evaluation of curve fit points with the initial point as the start point

The first point on the intensity decay curve is sensitive to the effect of the laser if the excited luminophore has not fully returned to the ground state or residual laser energy. Additionally, data points in the noise floor have a low coefficient of determination for exponential curve fitting. Therefore, a combination of data points on the decay curve was evaluated to understand the effect on the calculated lifetime and coefficient of determination. An example of one arrangement of the intensity decay is shown in Figure 40. The first point in the intensity decay is the starting point for calculating the single exponential decay lifetime, while the rest of the points are defined as endpoints totaling 18 combinations. A similar treatment was applied using the 1st through 5th points as start points and the rest on the curve as endpoints, which yielded 75 total combinations for calculating the single exponential decay lifetime shown in Figure 41. The lifetime values shown are averaged across 99 datasets. Figure 41a and Figure 41b show the lifetime for the 75 combinations at 101.15 kPa and 16.34 kPa, respectively, with single exponential decay least-squares fitting.

As shown in Figure 41a, the fluorescence lifetime increases with curve fit points and the start points at 101.15 kPa and 16.34 kPa. At ambient pressure, the lifetime does not vary if more than 5 points are used for the curve fit with the 1^{st,} 2nd, or 3rd image used as a starting point. Due to increased oxygen quenching, a high pressure, and a shorter lifetime, the intensity decay curve is near-zero intensity after the 5th data point, as shown in Figure 37. Due to increased fluorescence at lower pressures, the coefficient of determination is above 0.99 at 16.34 kPa compared to ambient for all combinations of curve fit points, as shown in Figure 41c and Figure 41d. The results indicate that using a minimum of three points to fit a single exponential decay with the 2nd or 3rd point on the intensity decay curve as a start point has a high coefficient of determination. In Figure 42, the repeatability of lifetime computed using the 3rd point as a start point, with three points for the curve fit, is consistent within the calibration range for the laser burst duration of 10.8 milliseconds. The effect of the laser during the initial warm-up time before stabilizing is more noticeable in lifetime data at lower pressures. As a result, there is more variation in the lifetime at the tail ends of the laser duration period. An additional threshold was applied to remove any lifetime results outside the 95% confidence interval. The coefficient of determination is greater than 0.998 for the final points used for calibration, as shown in Figure 43.

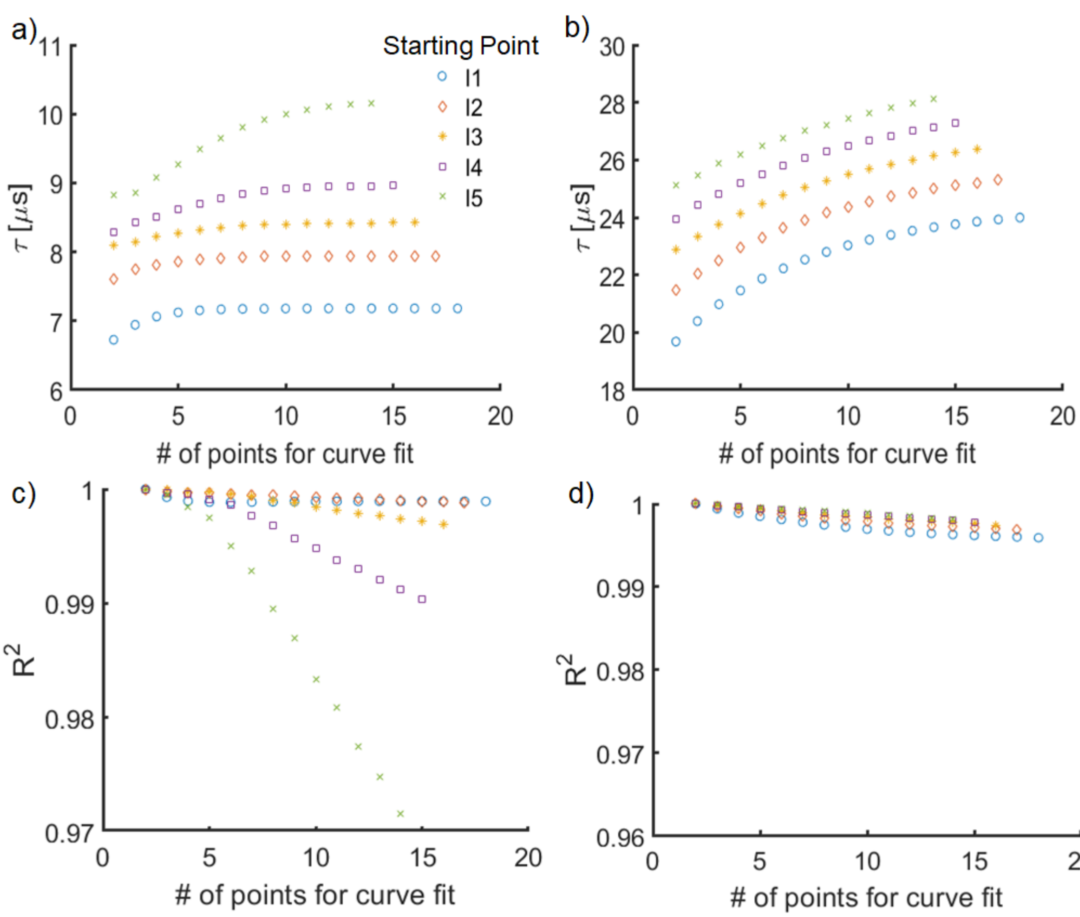

Figure 41: Computed single exponential decay lifetime using first five start points at a) 101.15 kPa and b) 16.34 kPa. Coefficient of determination at c) 101.15 kPa and d) 16.34 kPa

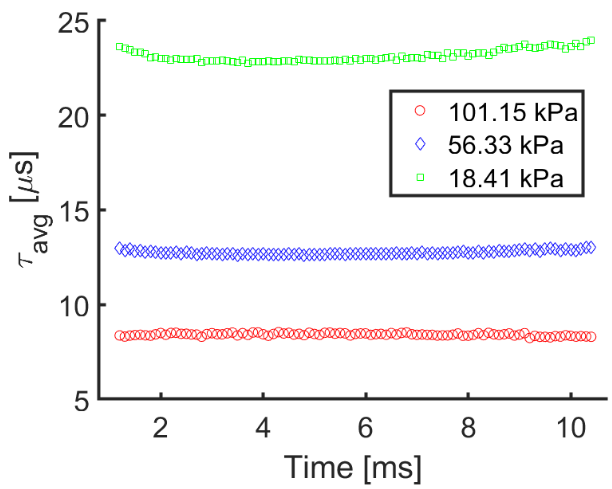

Figure 42: Computed lifetime over laser duration of 10.8 ms

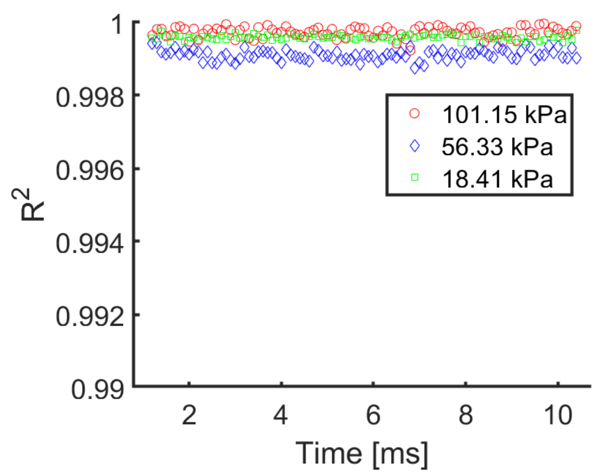

Figure 43: Computed coefficient of determination over laser duration of 10.8 ms

After selecting the optimal curve points from the intensity decay, a trade-off study with pixel binning was performed to reduce the uncertainty of using a single averaged value across all pixels and image pixelization without distorting the image. A 2-D convolution function from MATLAB (*conv2*) is applied to perform spatial averaging for each image. The kernel, convolution matrix, or mask is a small matrix with values that specify how the neighborhood of a pixel contributes to the pixel's state in a final image. The kernel matrix is defined with ones divided by the total number of elements in the kernel matrix. A convolution between the kernel and image includes adding each image pixel to its local neighbors, weighted by the kernel without any zero paddings at the matrix edges. For discrete, two-dimensional variables *G* and *H*, eq. (15) defines the convolution of *G* and *H*. Compared to other MATLAB tools such as *nlfilter*, *colfilt*, and *blockproc*, the *conv2* function provides a smoothing filter approach for images with a computation time of at least a magnitude faster. From a total of 6,534 images, each with 83 x 347 elements, a computational time of fewer than 2 hours is achieved for kernel matrix bundles: 1x1, 5x5, 10x10, 50x50, 50x100, and 83x347.

$$C(j,k) = \sum_{p}^{\infty}\sum_{q}^{\infty} G(p,q)H(j-p+1, k-q+1) \tag{15}$$

The effect of binning on the lifetime is illustrated in Figure 44. The average lifetime is displayed on the ordinate with 95% confidence interval error bars. There is a negligible difference between the average lifetime value for all binning bundles and calibration pressures. However, the lifetime variation gradually increases from high to low calibration pressures. The advantage of binning is more evident at low pressures where the lifetime variation is largest. The 5x5 binning bundle has a maximum deviation from the average lifetime value, while the 50x100 bundle has the minimum deviation for each calibration pressure. The coefficient of variation results in Figure 45 also confirms that the effect of binning is most significant at lower pressures. The difference in the coefficient of variation between the 5x5 and 50x100 binning bundle is 10.2% and 5.2%, respectively, at 18.41 kPa. The difference in coefficient of variation between the 5x5 binning bundle and 50x100 binning bundle is only 6.5% and 3%, respectively, at 101.15 kPa. Additionally, for the first three binning bundles (5x5, 10x10, and 50x50), the coefficient of variation monotonously decreases from low to high calibration pressures until about 80 kPa. For calibration pressures larger than 80 kPa, the coefficient of variation is constant.

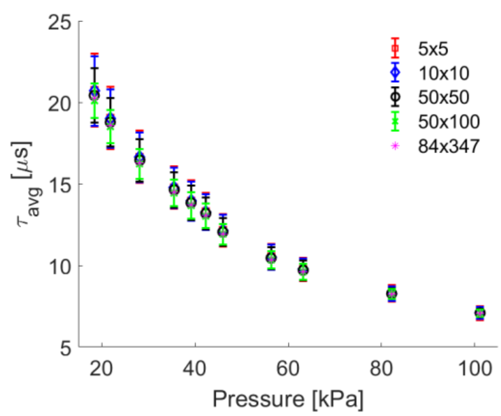

Figure 44: Binning effect on average and standard deviation of lifetime

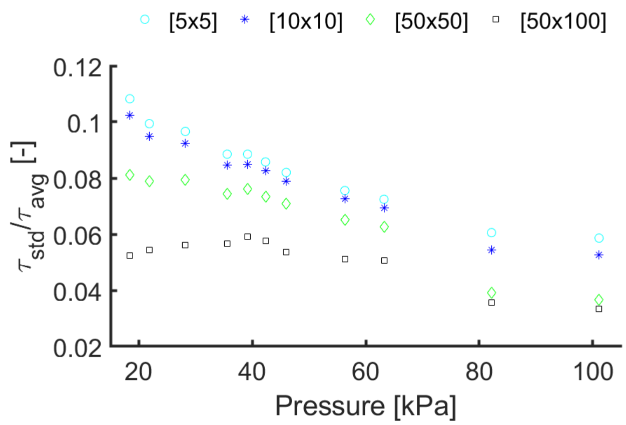

Figure 45: Binning effect on the coefficient of variation of lifetime

The 2nd order polynomial coefficients (C_1, C_2, and C_3) from eq (12) are solved using a least-squares fitting model that relates luminescent lifetime to pressure and is unique for each pixel bundle. The coefficient results from the 10x10 binning are shown in Figure 46, and the coefficient of determination is described in Figure 47. Although there is a significant variation in C_1 *and* C_2, compared to C_3, the resulting coefficient of determination for all pixel values exceeds 0.995, which indicates that the 2nd order polynomial is an accurate fit for the relationship between lifetime and pressure. The polynomial coefficients are applied to the lifetime calibration data to reconstruct the calibration pressure from the PSP.

The comparison between pressure tappings and PSP reconstructed pressure is shown in Figure 48 for each binning bundle. The uncertainty bars in the ordinate are 95% of the readings among all the pixels. The results indicate a linear trend that fits within the error bars. Contrary to the lifetime results, the binning effect on the reconstructed pressure is more evident near the maximum calibration pressure. Since pressure is inversely proportional to the single exponential lifetime, increased variability in lifetime results in decreased pressure variability. The relative difference between the calculated pressure from PSP and the pressure tappings is shown in Figure 49. The maximum difference between PSP and the reference calibration pressure is estimated at 4% at 49 kPa. At ambient pressure, the relative difference is less than 1%.

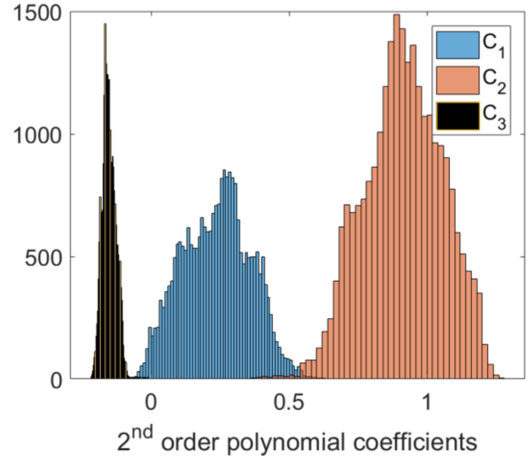

Figure 46: Histogram of 2^{nd} order polynomial coefficients

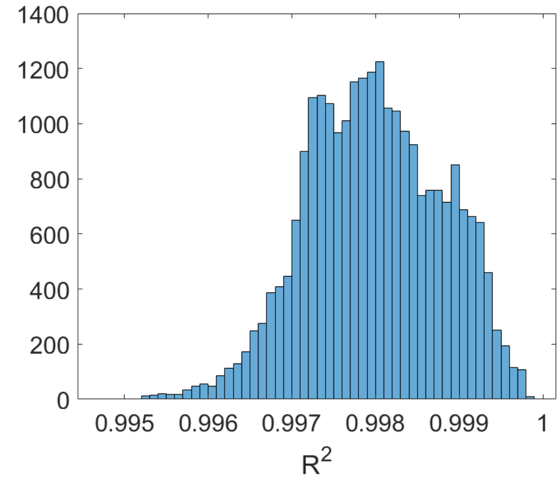

Figure 47: Coefficient of determination of 2^{nd} order polynomial coefficients

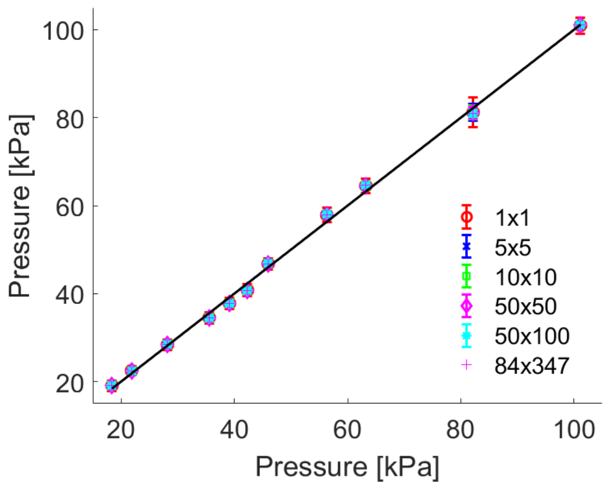

Figure 48: Comparison of calibration pressure from PSP and pressure tappings

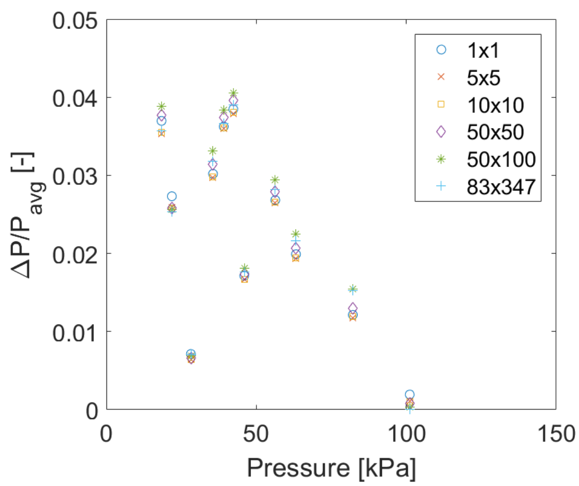

Figure 49: Relative difference between PSP and pressure tappings

4.3 Calibration uncertainty

Uncertainty analysis of the laser lifetime PSP methodology is performed considering the parameters that affect the conversion of the single exponential lifetime to pressure using eq. (12) with the 10x10 binning calibration data. Each independent variable is assumed to be uncorrelated with a Gaussian distribution. The effects of thickness errors and inhomogeneous illumination on the final uncertainty are negligible. The absolute uncertainty of the lifetime ratio and reference pressure is evaluated with a 95% confidence interval from 41 data points for a single pixel, 5x5, 10x10 bundles, and average of all pixels. The relative uncertainty results of the lifetime ratio are defined as the ratio of absolute uncertainty divided by the mean value, as shown in Figure 50. For each binning option, there is increased uncertainty at low calibration pressures. Moreover, the relative uncertainty is constant for calibration pressures over 50 kPa. The difference in relative uncertainty between the average of all pixels and the three other binning bundles is by a factor of two. The uncertainty at the reference pressure is zero since the lifetime values are normalized to the reference value.

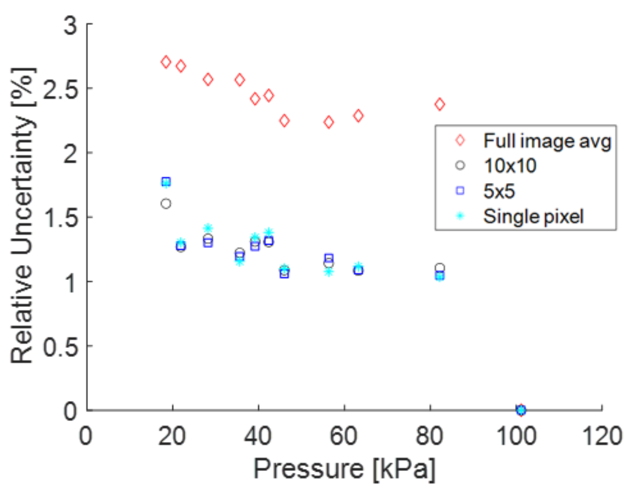

Figure 50: Relative uncertainty of lifetime ratio for each calibration pressure

Each pixel bundle is spatially averaged to a single value for the calibration coefficients (C_1, C_2, and C_3), after which the absolute uncertainty is computed from 41 data points. The results for the relative uncertainty of the calibration coefficients are shown in Figure 51. A change in calibration pressure does not affect the relative uncertainty since a single coefficient matrix is applied to calculate pressure from the lifetime ratio in eq. (12). The most significant relative uncertainty comes from the average of all pixels followed by the single pixel approach for all three coefficients. The 5x5 and 10x10 binning bundles have the lowest relative uncertainty and are almost the same in C_1 and C_2. In the results of C_1, the average of all pixels has a substantial value of 80% compared to about 30% for C_2 and C_3.

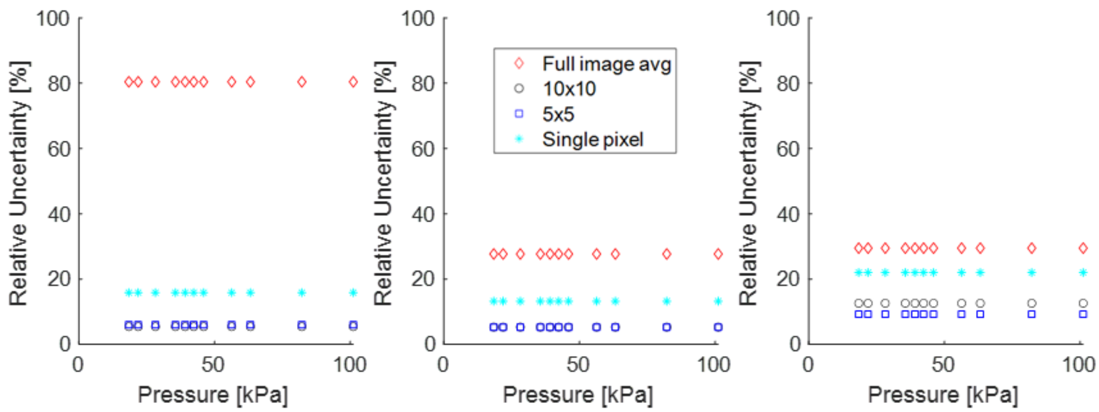

Figure 51: Relative uncertainty for calibration coefficients C_1 (left), C_2 (middle), C_3 (right)

The uncertainty of each independent variable is added to its average value to calculate pressure from eq. (12) and to estimate each parameter's uncertainty on the final pressure uncertainty. The pressure variation is characterized relative to the average pressure without any uncertainty. The sensitivity is the ratio of pressure variation over the relative uncertainty, and the final uncertainty is the root-sum-squares of each error source. The uncertainty approach is derived from Moffatt *et al.* [44]. The overall calibration uncertainty for a single pixel and bundles of pixels are shown in

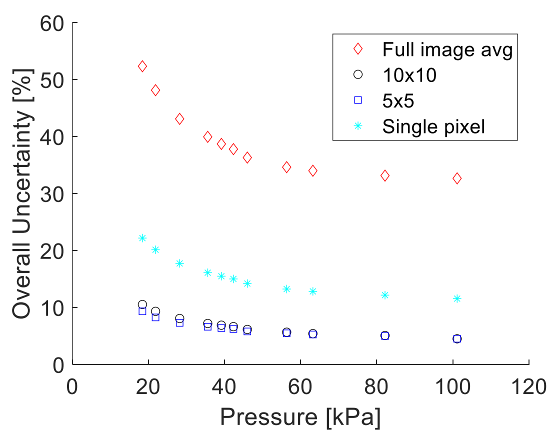

Figure 52: Overall pressure uncertainty for single and bundle of pixels

Figure 52. Given that the relative uncertainty from the calibration coefficients is constant for all calibration pressures, the most significant contribution to the overall uncertainty for low and high calibration pressures is directly from the relative uncertainty in the lifetime ratio. The relative uncertainty of the lifetime ratio and the overall uncertainty follow trends of decreasing uncertainty from the minimum pressure to about 50 kPa. For the 5x5 binning, the minimum uncertainty is 4.5% at 100.15 kPa. The maximum uncertainty is 8% at 18.41 kPa A single-pixel approach has reduced uncertainty compared to averaging all the pixels; however, the 5x5 and 10x10 pixel bundles show the most significant reduction in overall uncertainty.

The sensitivity as a function of calibration pressure for the lifetime ratio and calibration coefficients is depicted in Figure 53. For a given pressure at 82.2 kPa, the most sensitive variable to the final uncertainty is the lifetime. The lifetime has the most significant contribution to uncertainty since it is the highest power term in eq. (12). A change in the lifetime will contribute to a 155% change in the final uncertainty. The trend of sensitivity and pressure is similar to the relative uncertainty. The minimum pressure has the most substantial sensitivity of 185%, which implies that it is essential to minimize the pressure variation at lower pressures. At pressures above 50 kPa, the sensitivity is constant.

The calibration coefficient C_2 is the second most sensitive variable contributing to the final uncertainty. The sensitivity of C_2 as a function of the calibration pressure is displayed in Figure 53c. The single-pixel, 5x5, and 10x10 binning results coincide similarly to the other parameters. The sensitivity monotonously decreases from vacuum to ambient pressure. Since there is a single value of averaged C_2 for each calibration pressure, the significant contributor to C_2 is the lifetime variation.

Interestingly, the sensitivity of C_2 is above unity for pressures below 40 kPa, less than unity at pressures above 40 kPa. C_2 is the most significant contributor to the uncertainty among the other polynomial coefficients because it is the coefficient of the second term. In contrast, C_1 has the most negligible sensitivity effect on the final uncertainty because it is multiplied by the 2nd order first term. Moreover, the 2nd order term affects the trend of the sensitivity as a function of pressure. Opposite to the other calibration coefficients, the pressure increases monotonously with C_1. The final coefficient, C_3, is a constant in eq. (12), the sensitivity plot shown in Figure 53 is not a function of the lifetime ratio. The histogram of the calibration coefficients shown in Figure 46 corroborates the sensitivity behavior of the coefficients. The coefficient C_2 has the largest variability and corresponds to the coefficient with maximum sensitivity. Likewise, coefficient C_3 has minimal variation and corresponds to the coefficient with minimum sensitivity. It is worth noting an exception for pressures below 30 kPa; the C_1 coefficient has the minimum sensitivity to the final uncertainty.

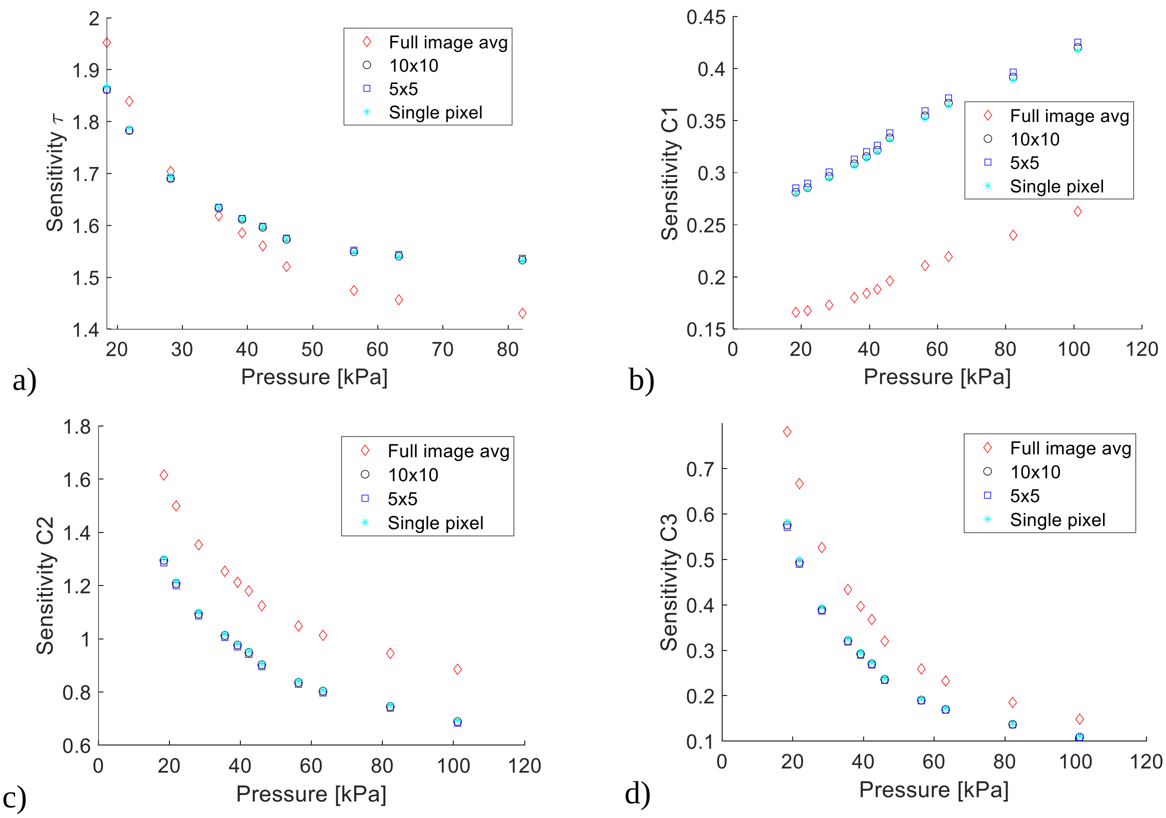

Figure 53: Sensitivity of lifetime ratio and calibration coefficients

The pressure variation, sensitivity, and total uncertainty at three calibration pressures (82.19 kPa, 42.33 kPa, and 18.41 kPa) are shown in

Table 2. The reference pressure has a unity sensitivity since the influence parameter has the same units as the measurand. The total uncertainty increased from 82.19 kPa to 18.41 kPa from 5.1% to 10.54%. The increase in pressure variation and sensitivity of the C_2 and C_3 coefficients directly contribute to uncertainty. In Figure 54, the standard deviation of pressure increases as a

function of calibration pressure. However, the relative standard deviation of pressure decreases with increasing calibration pressure.

Table 2: Uncertainty calculation at 82.19 kPa (top), 42.33 kPa (middle), and 18.41 kPa (bottom)

		Mean	Absolute uncertainty	Pressure variation [%]	Sensitivity
P_{ref}	kPa	101.14	0.173	0.171	1.00
C_1	[-]	0.42	0.0229	2.12	0.39
C_2	[-]	0.69	0.0366	3.96	0.75
C_3	[-]	-0.11	0.0137	1.72	0.14
τ_{ratio}	[-]	0.87	0.0095	1.67	1.53
Total	%			5.1	

		Mean	Absolute uncertainty	Pressure variation [%]	Sensitivity
P_{ref}	kPa	101.14	0.173	0.171	1.00
C_1	[-]	0.42	0.0229	1.75	0.32
C_2	[-]	0.69	0.0366	5.03	0.95
C_3	[-]	-0.11	0.0137	3.41	0.27
τ_{ratio}	[-]	0.56	0.0073	2.09	1.60
Total	%			6.67	

		Mean	Absolute uncertainty	Pressure variation [%]	Sensitivity
P_{ref}	kPa	101.14	0.173	0.171	1.00
C_1	[-]	0.42	0.0229	1.52	0.28
C_2	[-]	0.69	0.0366	6.87	1.30
C_3	[-]	-0.11	0.0137	7.25	0.58
τ_{ratio}	[-]	0.36	0.0057	2.99	1.86
Total	%			10.54	

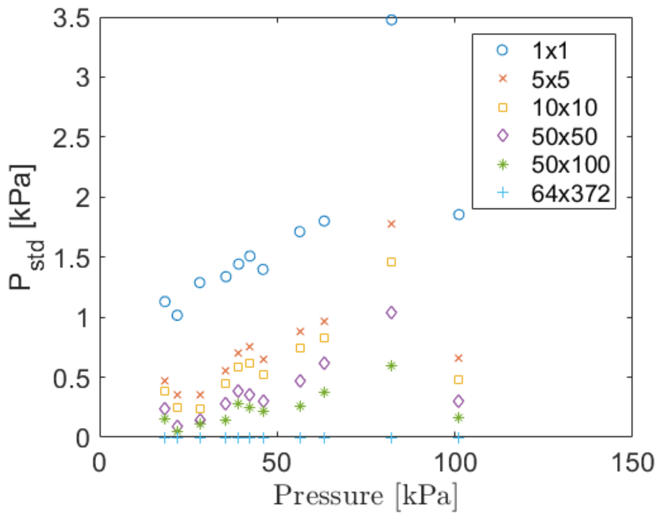

Figure 54: Standard deviation of reconstructed pressure as a function of calibration pressure

4.4 Time-averaged pressure analysis

The pulse lifetime method was validated on a wavy hub surface exposed to inlet supersonic flow. The test duration was approximately 100 seconds, providing a unique opportunity to test the technique since the laser fires every 10 seconds. Unsteady Reynolds-averaged Navier Stokes can generally provide an adequate prediction of the start of the separation bubble; however, they over-predict the magnitude of the separation bubble. Additionally, the experimental campaign is limited to discrete pressure tappings in the stream-wise and spanwise directions.

The flow behavior of the wavy surface is described from Shadowgraph experiments with the same test article and flow conditions [45]. Once the flow impacts the first wave, the flow is compressed, forming a shock. The flow accelerates after the compression zone in which the static pressure decreases, followed by a subsequent separation shock, as shown in Figure 55. A shear layer or separation zone is ultimately formed in the valley between the two wave peaks. A similar flow pattern is repeated for subsequent waves downstream at reduced intensities. Schlieren imaging results at 20 kHz [45] showed that flow instabilities were mainly observed in the shear layer and separation and downstream compression zones, explaining shear layer interaction with the consequent shock.

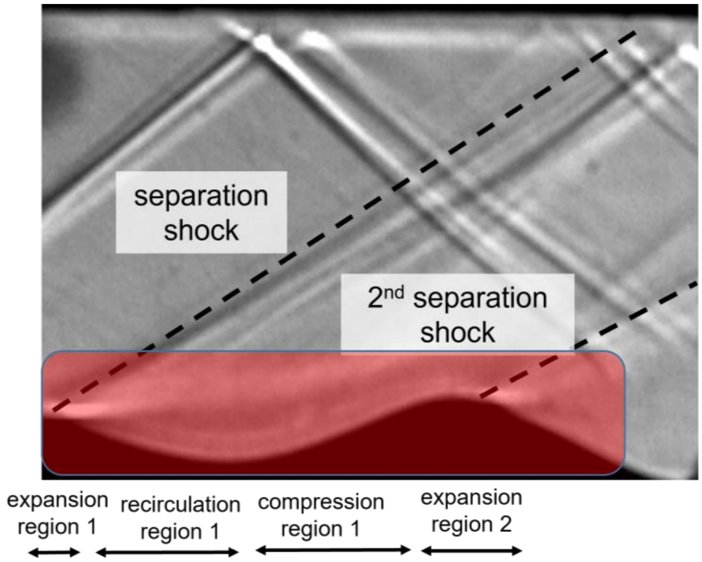

Figure 55: Shadowgraph results of wavy hub surface exposed to inlet supersonic flow

The wind tunnel PSP experiments were conducted at very low pressure downstream of the test section to achieve supersonic conditions with low total pressure and mass flow requirements. After vacuum calibration, the pumps were turned off, the clamps were removed from the big vacuum tank outside the facility, and upstream valves were used to set the correct mass flow rate through a purge line. Once the mass flow was stable, the upstream butterfly valve to the test section was opened. After a delay from the valve opening, the quantum pulse delay generator is triggered to start the sequence of laser excitation, followed immediately by image acquisition.

Three mass flow rates (3 lb/s, 4.25 lb/s, and 6 lb/s) were tested at a laser repetition rate of 10 kHz for wall pressure distribution comparisons. At each mass flow condition, 100 images of wall pressure distribution are acquired over a time duration of 10.8 ms. The 2nd order polynomial coefficients of each bundle of pixels from the no-flow calibration are applied to the lifetime ratio from 100 laser pulses during stable mass flow. The data set includes multiple 100 spatially resolved flow structures for 10.8 ms for each mass flow rate.

The time-averaged 2-D surface pressure acquired during a 6 lb/s flow experiment over a time duration of 10.8 ms is shown in Figure 56a. The spanwise, time-average pressure for different binning bundles is depicted in Figure 56b. A first compression wave provides a pressure increase (x = 0 to 0.1 [-]), followed by a first expansion region. A first separation shock appears at a location of x=0.25 [-] followed by a separation region (x = 0.25 - 0.5 [-]) due to the onset of the second wavy surface downstream. A second compression region with pressure rise is shown in the PSP data, followed by an expansion fan and a second separation shock. The results from PSP show excellent agreement with the Shadowgraph results for the same test case.

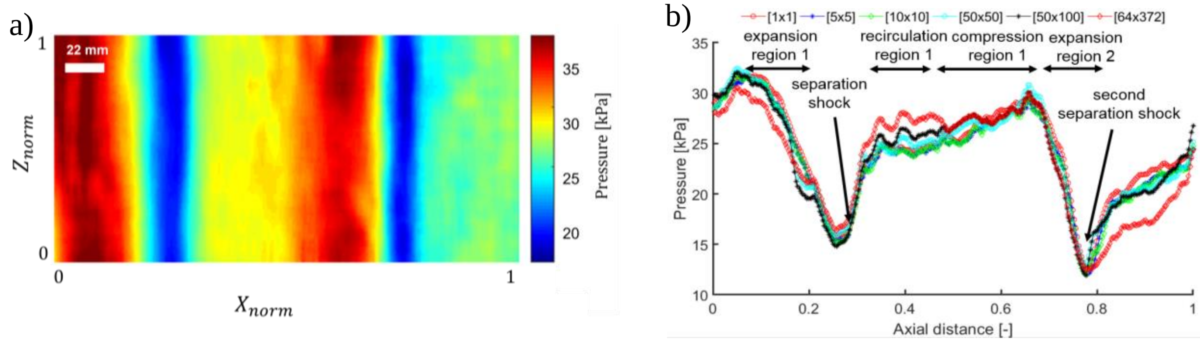

Figure 56: a) 2-D time-averaged surface pressure at 6 lb/s b) Spanwise average pressure for different binning bundles

The reconstructed 2-D pressure distribution at 4.25 lb/s in Figure 57a is compared to a RANS CFD result in Figure 57b. The qualitative comparison shows excellent agreement. The spatially resolved flow features are consistent with the CFD results for all binning bundles in spanwise and streamwise directions. The isentropic Mach number is the ideal Mach number without any flow losses and walls without friction. In eq. (16), the total inlet pressure is normalized by the resolved static pressure at each pixel (i,j). The ratio of specific heat γ was assumed as 1.4. The total pressure was acquired during the experiment from a total pressure Kiel probe at the inlet of the test section, far upstream of the wavy surface. The supersonic Mach number distribution shown in Figure 58 is opposite to the pressure trend as expected. It highlights the peak Mach number point just before the separation shock. The 2-D pressure and Mach number results provide invaluable data for validating turbulence models for computational simulations.

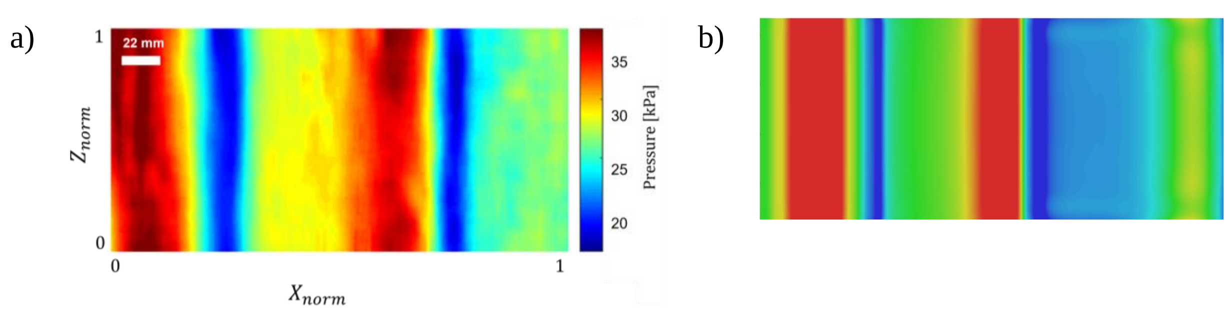

Figure 57: a) 2-D time-averaged surface pressure at 4.25 lb/s b) RANS CFD simulation results

$$M_{is_{(i,j)}} = \sqrt{\left(\left(\frac{P_o}{P_{(i,j)}}\right)^{\frac{\gamma-1}{\gamma}} - 1\right)\frac{2}{\gamma - 1}} \tag{16}$$

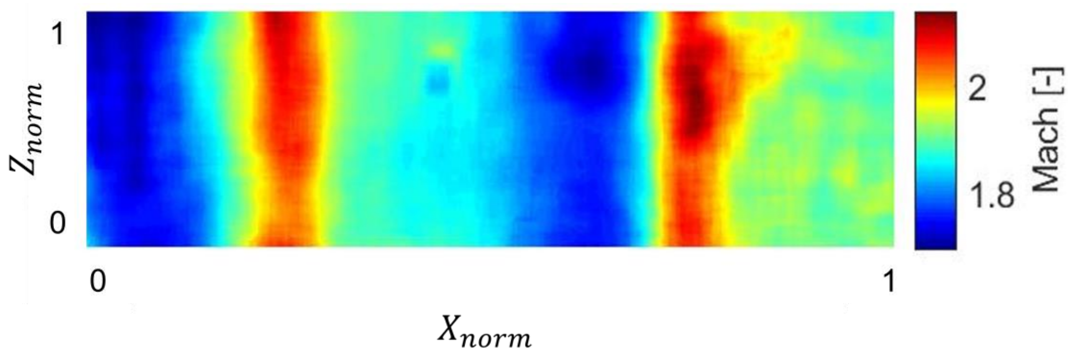

Figure 58: Isentropic Mach number distribution from PSP static pressure data

4.5 Camera calibration and image resectioning:

Image resectioning (mapping of two-dimensional (2-D) pixel image data to three-dimensional (3-D) surface geometry) is utilized in this experiment. A photogrammetry technique is applied to establish the geometrical relationship between the image plane and 3-D object space when the object to be measured is not easily accessible, when the object moves or deforms, or when its contour and surface information is required [46]. The calibration camera exterior, interior, and lens distortion parameters are used to supplement collinearity equations. A detailed summary of this technique for aerospace applications is provided by Liu et al. [46]. The Direct Linear Transformation (DLT) and the optimization method developed by Liu et al. [47] were used in this experiment. The optimization method combined with an initial guess from the DLT method allows rapid semi-automatic camera calibration. Moreover, the technique is already applied to TSPs, PSPs, and model deformation measurements.

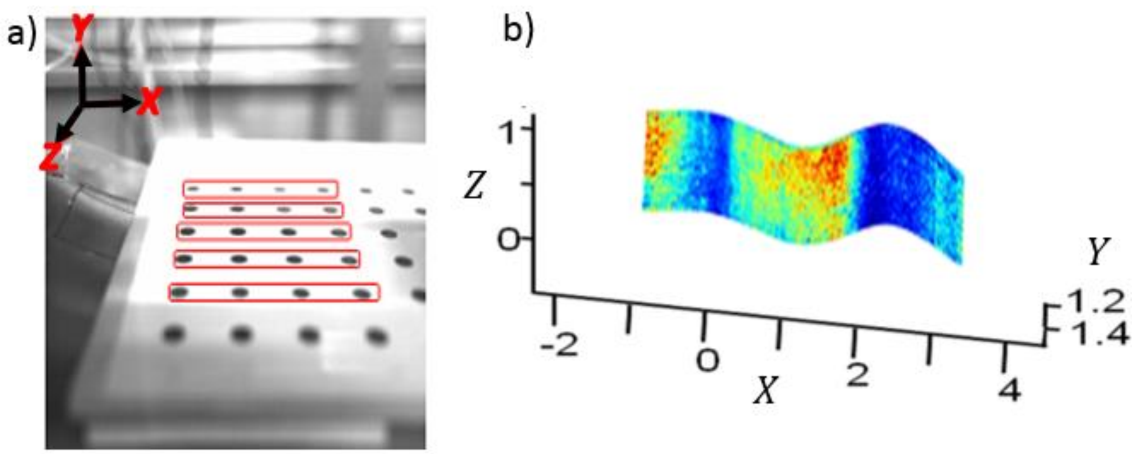

Figure 59: a) Camera calibration dot targets
b) PSP data mapped unto 3-D model geometry

The procedure for camera calibration is as follows: A dot target with a thickness of 0.25” is placed at six height levels in the object space (0, 0.25”, 0.5”, 0.75”, 1.0” and 1.25”). Black dots are printed on white paper for contrast and attached to the target made of wood material. The diameter of the dots is 0.25” and are equally spaced 1” in vertical and horizontal directions. Based on the camera focus, perspective, and region of interest, an array of dots are selected from the dot target and used in the calibration procedure. Next, any rotation or translational shifts needed for the system are applied based on the camera's mounting. After these steps, the centroids of the dots are selected and used to build up the image space in the calibration technique. Finally, the collinearity equations are applied to directly map the image space to the object or model space. The calibration procedure is summarized in Figure 59a. An example of PSP data mapped unto the 3D object space is shown in Figure 59b.

Comparison between PSP, low and high-frequency pressure sensors

The comparison between the PSP time-averaged pressure at two-span locations with low-frequency static pressure tappings, high-frequency ultra-miniature piezo-resistive sensors, and CFD RANS results is depicted in Figure 60. The PSP static pressure results align with low and high-frequency pressure sensors and the CFD simulation results. The peak pressure and the minimum pressure are both accurately measured by the PSP. The dotted black line represents the averaged pressure distribution from CFD. The black markers represent the average normalized pressure from the unsteady pressure sensors, and the blue and red tags symbolize the normalized pressure measured with discrete low-frequency pressure sensors.

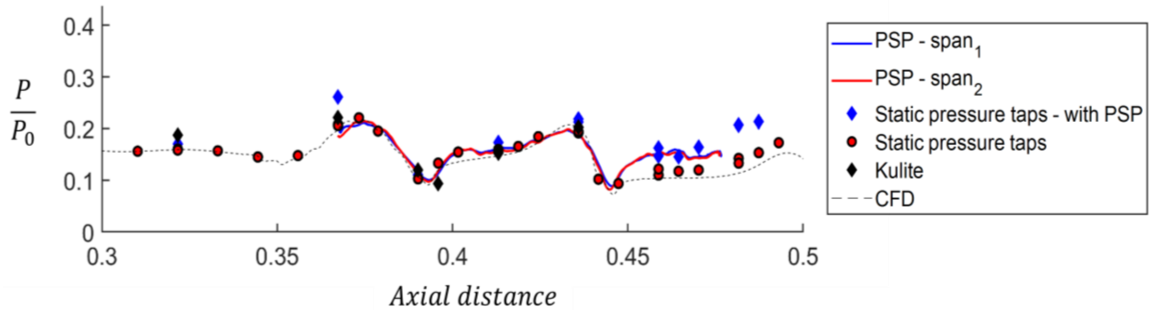

Figure 60: Comparison between PSP and pressure taps

4.6 Spatial-temporal surface pressure analysis

The pulse lifetime PSP technique outputs time-resolved data at 10 kHz, with a camera frame rate of 200 kHz. During 10.5 milliseconds, 100 timestamps of 2-D pressure data are resolved with a period of 100 microseconds between each image of pressure. The average pressure from each pixel normalizes the standard deviation. Figure 61 shows the spatial distribution of the coefficient of pressure variation at a mass flow rate of 6 lb/s. The unsteadiness in the expansion and separation location is relatively more intense than in the recirculation and compression regions. Moreover, the second wave has a stronger unsteadiness near the separation shock location than the first wave. The pressure variation is as high as 60% of the average pressure near the second shock location, consistent with reduced mass flow rates. The histogram of the pressure in the separation location regions and shock location regions is shown in Figure 62. At the shock location, the pressure is centered around the average pressure. However, a 10% increase and a 5% decrease from the average pressure in the separation locations confirm the relatively high unsteadiness levels in the separation location region.

A time series of pressure in the expansion and recirculation region is depicted in Figure 63. The variation between frames is expected due to the interaction between separated shock and the separated area and the compression shock and recirculation region. There are spanwise and streamwise fluctuations in pressure in this time series of nine-time steps. This demonstrates that the pulse lifetime method can acquire high-frequency pressure measurements in a high-speed flow environment with high spatial pressure gradients. Each pixel indeed represents a high-frequency sensor.

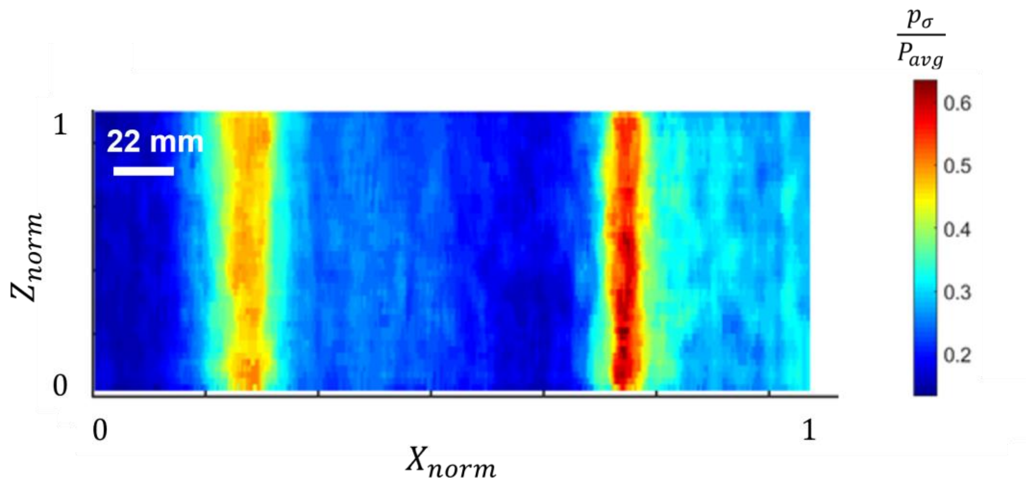

Figure 61: 2-D coefficient of variation of pressure calculated over 10.8 ms

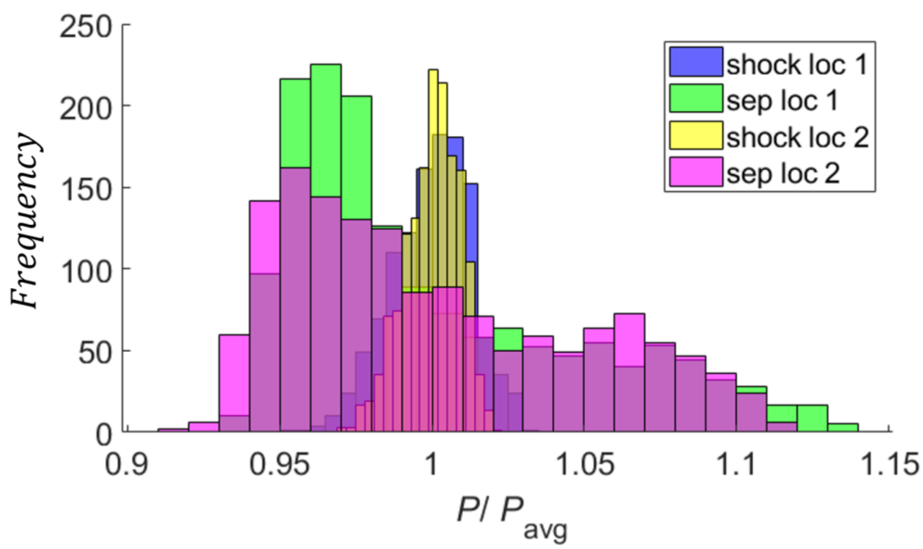

Figure 62: Normalized pressure at shock and separation locations

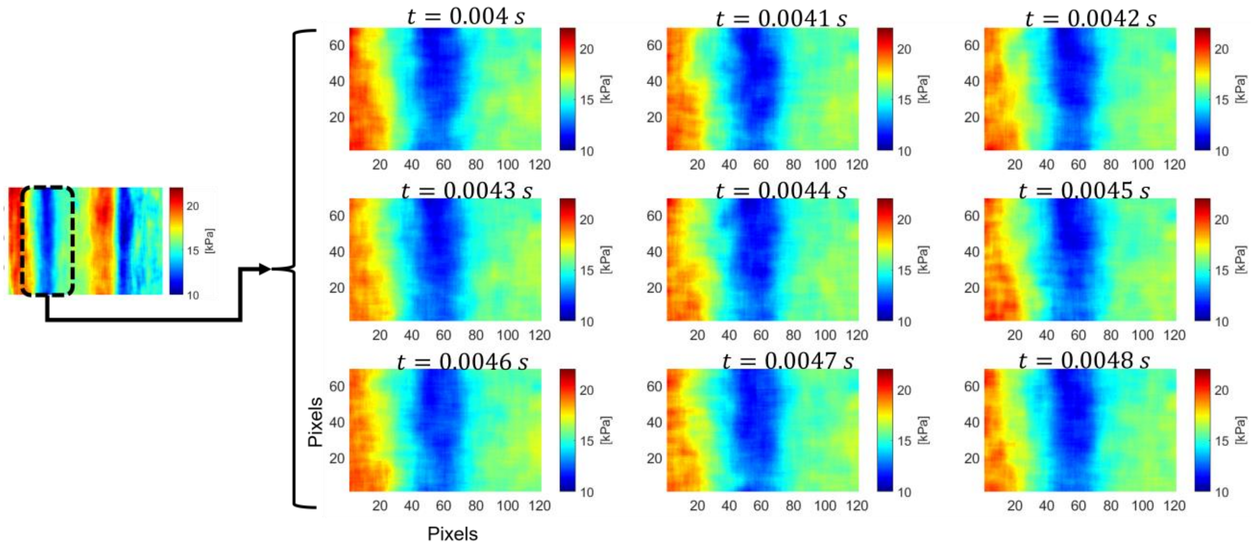

Figure 63: Surface pressure time series of the expansion and recirculation region

CHAPTER 5: APPLICATION OF PULSE LIFETIME PSP IN A HIGH-PRESSURE TURBINE VANE ASNNULAR CASCADE

Acknowledgment of prior publication: Aye-Addo, N., Paniagua, G., Gonzalez Cuadrado, D., Bhatnagar, L., Castillo Sauca, A., Braun, J., Gomez, M., Meyer, T., and Bloxham, M. (October 13, 2021). "Development Of A Lifetime Pressure Sensitive Paint Procedure For High-Pressure Vane Testing." ASME. J. Turbomach. DOI: https://doi.org/10.1115/1.4052739

The airfoil surface pressure is an important parameter for quantifying lift distribution and aerodynamic loading. For example, the aft part of the vane suction side (SS) experiences diffusion and is prone to separation for some airfoil designs. Additionally, the cross stream-wise pressure gradients from the pressure side (PS) to SS are intensified with higher blade loading and cause secondary flow structures in the passage. Specifically, for low-aspect-ratio turbine airfoils, the radial pressure gradient may be on the same order of magnitude as the transverse blade-to-blade pressure gradient. Radial variation of blade loading can also cause secondary flows even in the absence of inlet vorticity [1]. Finally, from a forced response and a high cycle fatigue perspective, the static pressure on the stator vane also fluctuates periodically as it encounters the potential field of a downstream blade. Highly spatial and unsteady analysis of the flow physics on the suction side can be a valuable tool to evaluate the performance differences between airfoil designs and the unsteadiness of pressure waves due to downstream disturbances or secondary flows.

One of the first demonstrations of PSP applied in turbomachinery was in a low-speed facility at the Wright Laboratory Turbine Engine Research Center (TERC) in August 1994 [48]; however, the images were not correctly aligned. Navarra et al. [49] applied steady-state PSP to the suction surface of a first-stage rotor transonic compressor and compared pressure results qualitatively to CFD. Temperature correction was applied using the predicted surface temperature from CFD. At temperatures above 80° C, the temperature uncertainty is less than 1° C to ensure a 1% error in the pressure measurement. Jordan et al. [50] performed steady-state PSP on a large-scale commercial-engine test stand. The surface pressure on the engine inlet bell mouth was measured with PSP. A coordinate mapping allowed reference images acquired under wind-off conditions to be registered and accurately ratioed with wind-on conditions to mitigate temperature, model deflection, and warping errors.

Gregory et al. [16] applied fast responding PSP to measure unsteady pressure fluctuations on a turbocharger compressor inlet wall. A shock-tube and fluidic oscillator were used to characterize a frequency response of 40 kHz. An iterative process was implemented to match the rotor position between wind-on and wind-off reference images due to a phase delay in the triggering system. In recent years the lifetime PSP method has also been extensively applied to rotorcraft blades ([51], [24], [52–54]). However, there is still a gap in the literature on applying lifetime PSP to satisfy the spatial and temporal requirements for high-pressure turbine testing at aerodynamically representative conditions compared with conventional pressure transducers. Combining high-fidelity data and 3-D CFD can potentially reduce steady losses in a turbine by 10%, equivalent to about a 0.7% reduction in SFC for a large turbofan engine [55].

This chapter focuses on applying the developed pulse lifetime technique discussed in Chapters 3 and 4 to a high-pressure turbine vane suction surface in the Big Rig for Annular Stationary Turbine Analysis (BRASTA) test section at the PETAL lab. A detailed review of the wind tunnel and annular test section design (TRL 3-4), flow conditions, and layout can be found in reference [43]. The annular vane cascade is a large capacity test section with a shroud diameter of 840 mm, and a maximum flow rate of 18 kg/s at a wide range of temperatures. The test section's large size maximizes the spatial resolution of optical techniques such as high-frequency PSP and PIV.

5.1 Facility description

The facility operation schematic is illustrated in Figure 64. Compressed dry air at 15 MPa is stored in a 56 m3 pressure tank during facility operation. One pipeline guides flow into the test cell and discharges from the high-pressure reservoir in a mixer. The other pipeline diverts air through a natural gas heat exchanger. For uniform flow temperature, pipe elbows are placed in the pipeline downstream to enhance mixing between hot and cold lines. The mass flow ratio between both pipelines determines the flow temperature of the experiment.

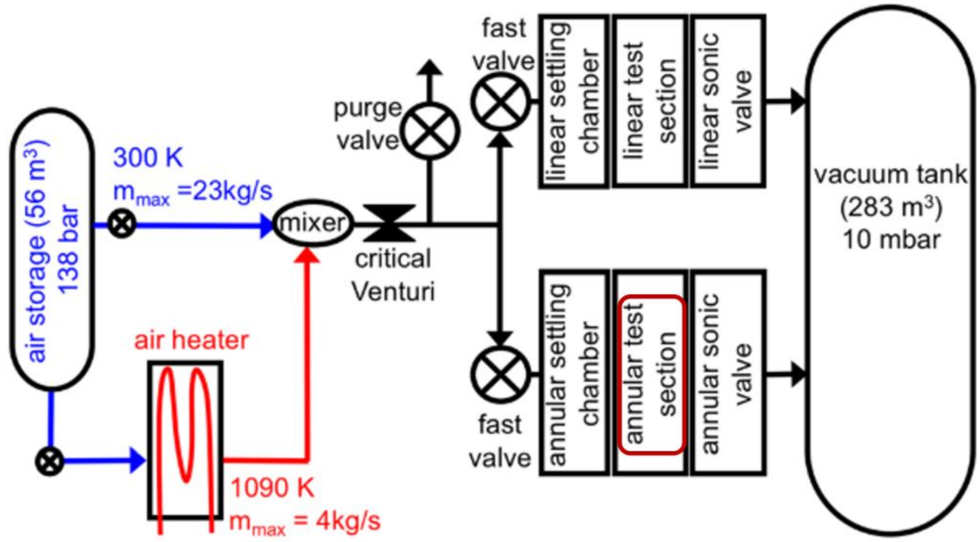

Figure 64: Facility operation with a High-pressure turbine vane cascade mounted in the annular test section

While the heat exchanger heats the fluid, the air is vented through a purge line outside the test cell. Once the flow temperature is stable, a fast-actuating valve upstream of the annular cascade is opened, and another fast-actuating valve in the bypass line is closed. The air is radially discharged into a settling chamber before passing through honeycombs and flow straighteners. The flow is then accelerated through the inlet contraction area and released into the test section with uniform spatial and temporal flow conditions. The flow exits to a vacuum tank through a sonic valve. Once it is choked, the sonic valve isolates the test article from the downstream conditions and provides an independent adjustment of Reynolds and Mach numbers.

A forward-looking aft (FLA) view of the annular vane test section is shown in Figure 65. The annual vane row has a rainbow design for the modular testing of two geometries. The configuration used for this experiment is a traverse system mounted on the right side of the test section to acquire traverse flow field data downstream of the vane geometry A. On the other side of the test section, pressure taps are installed in the PS, SS, hub, and shroud passage of a single vane row. The PSP was applied to the suction side of the vane adjacent to the vanes instrumented with pressure taps. The vane was located more than three rows away from the split line between the two geometries to mitigate any flow effects from the change in geometry. The vane surface is accessible through one of the four large azimuthal rectangular windows to apply PSP on the vane surface in-situ, calibrate the camera, and align the laser beam. The window is simultaneously an egress for the pressure tube lines and thermocouple wires for total pressure rakes, total temperature rakes, and static pressure tappings in the vane. Once the test section was mounted in the annular wind tunnel facility, the optical table and optical rails were mounted around the facility to begin the experiment's alignment process and optical setup.

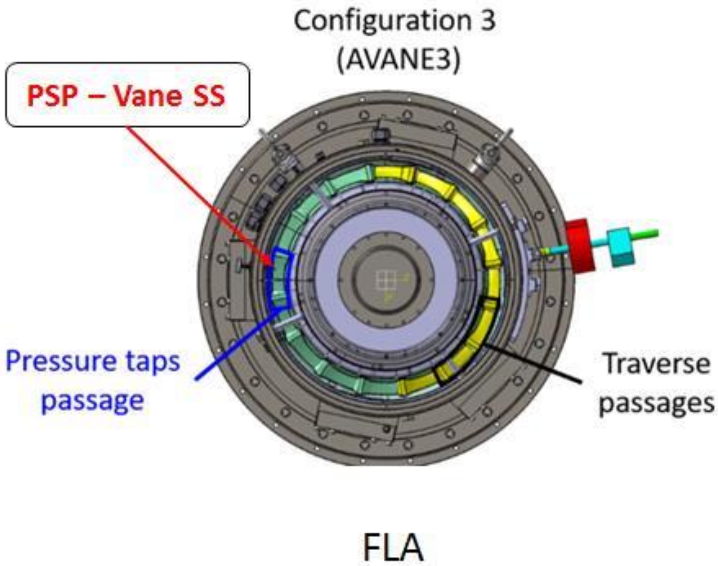

Figure 65: FLA view of the annular test section

Table 3: Annular vane cascade operating conditions

***Tt* [K]**	***Re/L* [1/m]**	**Mach Number Plane 2**	**Mass flow [kg/s]**
311	$1.5 \text{x} 10^7$	0.69	11.3

The test operating conditions are summarized in Table 3. The vane has an outer radius of 420 mm, a radial span of 63 mm, and a flow turning of approximately 76°. The low vane aspect ratio reflects the small core turbine design space. The inlet temperature of 311 K with a mass flow rate of 11.35 kg/s was achieved by mixing the hot and cold lines and applying the energy balance calculations from eq. (17) to (23). The sonic valve area was opened to 31.9% to achieve an exit Mach number of 0.69 at plane 2 (42% C_{ax} downstream of the vane trailing edge).

$$C_p = 1161.482 - 2.37T + 0.0149T^2 - 5.035 \times 10^{-5}T^3 + 9.929 \times 10^{-8}T^4 - 1.11 \times 10^{-10}T^5 + 6.540 \times 10^{-14}T^6 - 1.574 \times 10^{-17}T^7 \tag{17}$$

$$Q_{cold} = m_c Cp_c T_c = 8.63\frac{kg}{s} \times\ 259.8\,K\ \times\ 1005.49\frac{J}{kg * K} = 2.253 \times 10^6\,W \tag{18}$$

$$Q_{hot} = m_h Cp_h T_h = 2.72\frac{kg}{s} \times\ 477.6\,K\ \times\ 1025.35\frac{J}{kg * K} = 1.33 \times 10^6\,W \tag{19}$$

$$Cp_{mixed} = \frac{Cp_c + Cp_h}{2} = 1015.42\frac{J}{kg * K} \tag{20}$$

$$m_{final} = m_c + m_h = 11.35\,kg/s \tag{21}$$

$$Q_{total} = Q_{hot} + Q_{cold} = 3.587 \times 10^6\,W \tag{22}$$

$$T_{final} = \frac{Q_{total}}{m_{final} \times Cp_{mixed}} = 311.3\,K \tag{23}$$

5.2 Performance data instrumentation

The annular vane cascade has a maximum capability of 545 sensors that can be used to run any experiment or configuration. The measurement chain for each sensor is shown in Figure 66. For PSP application to the vane, the most critical sensors required for the experiment are the total temperature, metal temperature, total pressure, and static pressure. The sensor (type, location, count) and signal conditioning systems' uncertainty are accounted for in the uncertainty of the wall measurements.

The signal conditioner used to acquire total and metal temperature measurements is a VTI EX 1048A system with 48 differential inputs. Thermocouples are mainly used to measure the total temperature because they respond faster than resistance temperature detectors. A mini-marlin K-type connector interfaces with the 2-pin input connection on the *EX 1048A.* A braided, insulated, shielded thermocouple wire connects the thermocouple to the mini-marlin connector. The conditioning system has an internal isothermal section monitored by precision thermistors (one for every four thermocouple channels). The accuracy of the cold junction compensation on the VTI system is less than 0.3 °C with a 0.1 °C resolution. The CJC is synchronized with the input voltage channels with a maximum time separation of less than 4 ms between the input and associated CJC measurements. The system has an in-built 2-pole Bessel filter with a cut-off frequency of 4 Hz, providing a low noise floor and common-mode rejection. The sampling rate was 400 Hz to have a standard acquisition sampling rate between the pressure scanners and the temperature signal conditioner. Data is continuously streamed over Ethernet from a network switch to the data acquisition PC in the control room during the experiment.

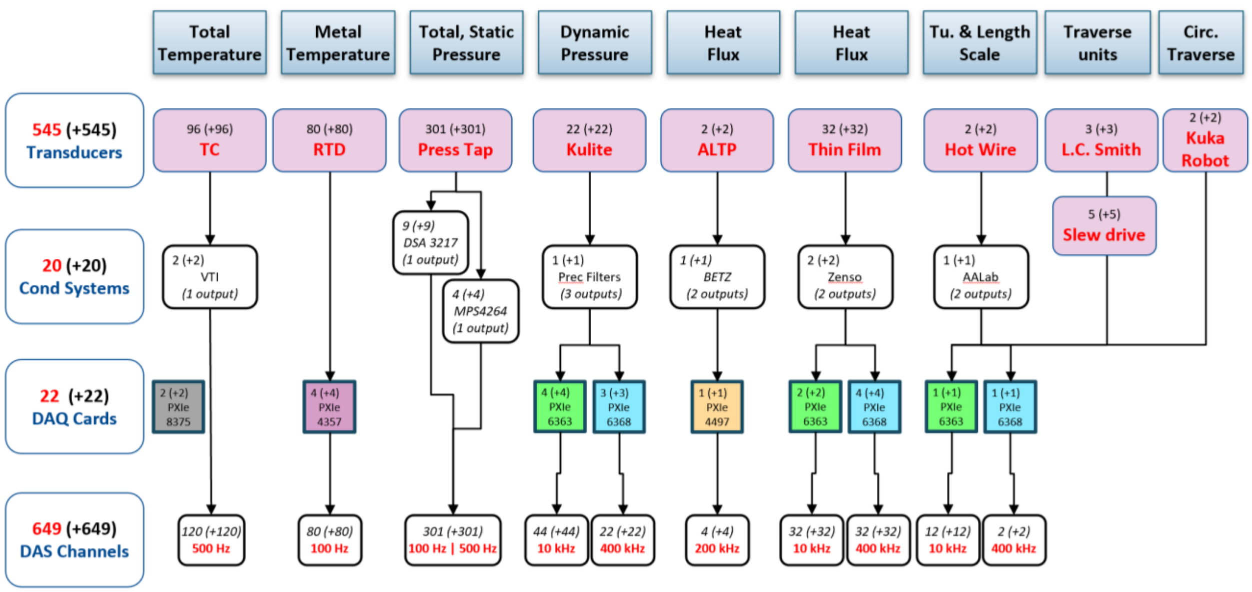

Figure 66: Instrumentation layout of annular wind tunnel

Resistance temperature detectors are primarily used to measure the metal temperature. They do not drift significantly between calibrations and are more linear and stable than thermocouple sensors. A 4-wire bridge configuration is the most accurate configuration for RTDs since it compensates for all resistance in the lead wires and connectors between them. Two wires link the sensing material to the monitoring device on both ends of the sensing element. One set of wires sends a current used for measurement and the other set measures voltage drop over the resistor. A *National Instrument PXIe-4357* device with an ADC resolution of 24 bits is used to measure the resistance of the RTD sensors. The maximum sampling rate of the device is 100 Hz, and that was the setting used for this experiment. The ADC timing mode was selected for the highest resolution setting with the lowest noise floor. The RTD measurement accuracy is 0.07 °C, and 0.09 °C at operating temperatures of 0 °C and 100 °C, respectively. A PCI Express Host (PCIe-8375) remote controller in the data acquisition PC in the control room is connected by fiber optic cable to a PXIe-8375 remote control module in the NI PXIe-1085 chassis for data streaming. The fiber-optic remote control is ideal for long-distance control of devices and electrical isolation.

The total and static pressure in the test section was measured using Scanivalve pressure scanner units: DSA 3217 and MPS 4264. The sampling rate of both devices was 400 Hz for the experiment. The accuracy for the pressure scanners is ± 0.05% of the full-scale range. Data is streamed to the data acquisition PC over the network. The static pressure tappings data reference PSP calibration data and provide comparisons for flow data. The measurement chain of pressure taps with pneumatic lines with reduced length is essential for a fast response time to a change in pressure. The pressure scanners measure gauge pressure and require a reference pressure either connected to ambient or back pressure based on the pressure range for the experiment. An extremely accurate reference pressure (GE DPI 610 calibrator) with an accuracy of ± 0.01% of the full-scale range is used with a precision of 0.004% full-scale range. No-flow data is acquired before and after the experiment to correct any sensor drift throughout the test. A precise feedback signal from the camera is synced with the static pressure tapping data when the camera's exposure is active to align images with the correct calibration pressure or flow data.

The slew drive system controls the sonic valve area downstream of the vane row and sets the test section Mach number. A quadrature encoder connected to the slew drive motor is wired to an NI PXIe-6363 A/D card. Three encoder outputs (A, Z, and B) are used to determine the relative position of the sonic valve based on the number of revolutions of feedback measured by the encoder from a home position of 100% opened area. A position sensor is also mounted in the sonic valve to detect the completely open or closed limit. The fast response pressure transducers (Kulite sensors), Atomic layer thermopile (ALTP) sensor, Hotwire, L.C. smith, traverse units, and Kuka robot were not used for this experimental campaign.

The sensors used for this experiment are outlined in Figure 67. A total pressure Kiel probe is positioned at the aerodynamic inlet plane (plane 0). Additionally, an in-house manufactured 12-head total pressure and temperature rake are installed along the circumference of plane 0 to measure the radial distribution of pressure and temperature. At plane 1, upstream of the vane, a 9-head pressure and temperature rake are positioned in addition to static pressure tappings and

RTD’s in the shroud and hub. Downstream of the vane in plane 2, pressure taps and RTDs are mounted in the shroud, and 3-head pressure rakes are mounted in a section 180° from the location of the painted PSP vane.

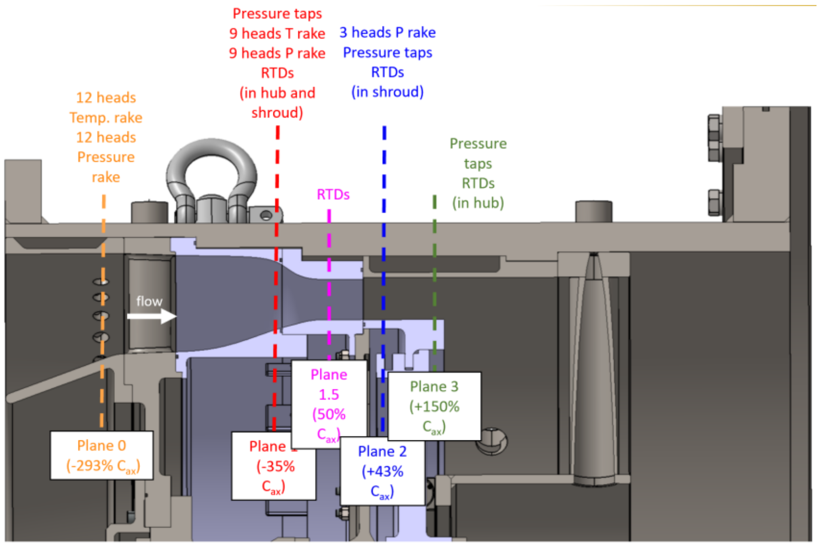

Figure 67: Section view of the flow path and instrumentation planes

5.3 Numerical methodology

There are two primary considerations for applying PSP in the annular wind tunnel. The first is to identify the flow features with numerical tools that could be resolved by PSP considering the limitations of the technique. Secondly, optical access in the rig is evaluated for laser delivery, imaging, and application of pulse lifetime PSP to the test article.

The numerical simulations were performed using the Rolls-Royce proprietary meshing package PADRAM and the CFD package HYDRA with the k-omega SST turbulence model [56]. A half annulus simulation was modeled using a structured H-O-H mesh with approximately 17 million cells. A close-up view of the mesh in the region of the PSP measurements is provided below in Figure 68. The simulation boundary conditions are derived from the test data. The inlet boundary was defined using a specified total pressure, total temperature, k-omega turbulence quantities, and radial and pitch angles. The exit boundary condition was set using an outflow condition with a specified hub static pressure and a radial equilibrium assumption. Periodic surfaces were assumed on the circumferential boundaries, and the solid surfaces were defined as viscous walls.

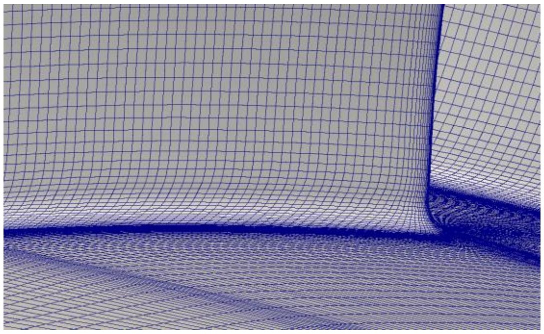

Figure 68: Close up view of mesh in the region of the PSP measurements

5.4 Optical setup

The first step in the optical setup process is to align the camera to the vane suction surface's field of view and spatial resolution. The camera's weight and more limited mounting options with the ports and window make it necessary to set it up before the laser is aligned to the vane. Once the camera’s position is fixed, a 3-D printed dot target is mounted on the vane to calibrate the camera, as shown in Figure 69 and Figure 70. The borescope mounted with the camera was initially positioned through the rectangular window, depicted in Figure 71. The borescope is aligned through an inner and outer metal blank, and the insert frame needs to be fully secured during camera calibration. The camera is calibrated with the 532-notch filter installed with a retainer ring mounted in the c-mount extension rings.

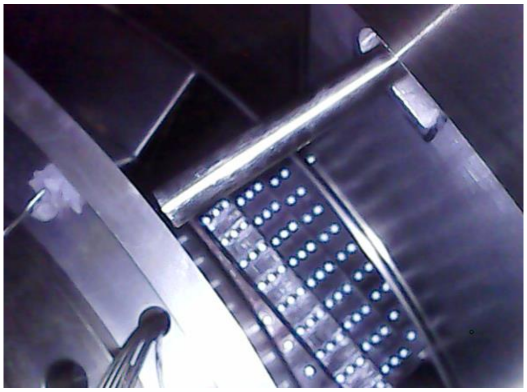

Figure 69: Endoscope view of dot target mounted on vane surface

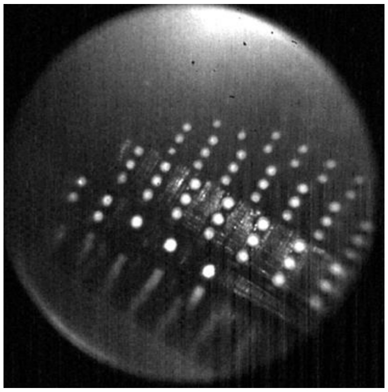

Figure 70: Borescope view of dot target mounted on vane surface

After camera calibration, the vane is painted through the same window, so to have repeatable camera calibrations while opening and closing the window after calibration is not feasible. Moreover, instrumentation such as plastic tubes, thermocouple wires can be easily damaged. A 1.5” *AS 5202* port downstream of the vane trailing edge was used as a second location for the camera, as shown in Figure 72. In this case, the rectangular window access was primarily used to check the laser beam, install, and remove the camera dot target, paint the vane, and instrumentation egress.

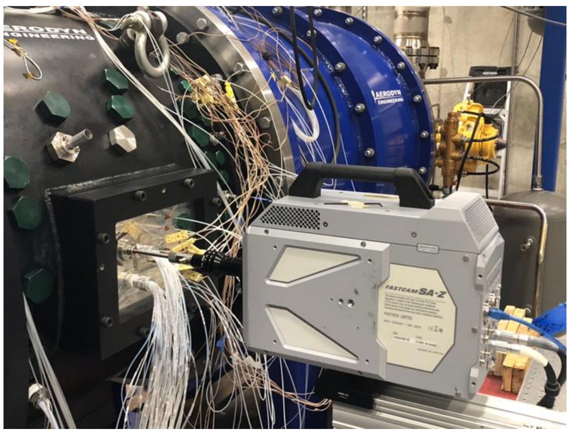

Figure 71: Borescope positioned through the large rectangular window

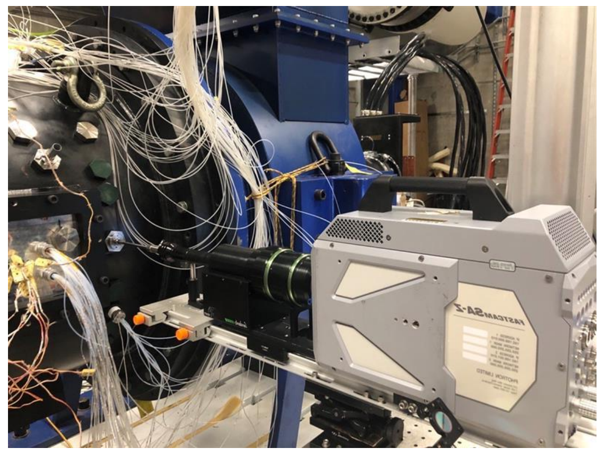

Figure 72: Borescope positioned through the 1.5" optical port

Initially, experiments were performed with a *SAZ Photron* camera and a borescope, as shown in Figure 71. However, due to the limited borescope diameter of 6.35 mm and 12.7 mm optics in the laser delivery probe, the signal to noise of the first three images after the laser pulse was not sufficient to compute the single exponential lifetime with high accuracy. To improve the light sensitivity and extend the camera's dynamic range to lower levels, a *HiCATT* high-speed imaging intensifier was mounted between the camera and the borescope, as shown in Figure 72. The quantum efficiency output of the intensifier is displayed in Figure 73. Compared to other available intensifiers, the *HiCATT* provides the maximum quantum efficiency at 650 nm to capture the peak fluorescence of PtTFPP. An optical lab jack was also installed to aid the fine adjustment of the height of the camera-intensifier-borescope setup. The gate width of the intensifier was 4.5 μs, which is 1.11 μs longer than the shutter speed of the camera. The non-linear gain function was increased in small increment amounts until the required fluorescence was achieved without camera saturation. The intensifier was synchronized with the laser and the camera with the *Quantum* delay pulse generator.

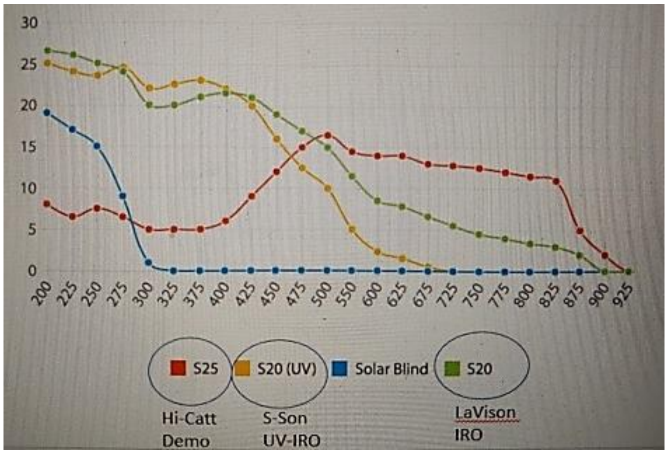

Figure 73: Quantum efficiency for Intensifiers

After camera alignment, the laser beam is aligned through lenses and mirrors. The optical layout is shown in Figure 74. Outside the test section, the laser beam is guided into the laser delivery probe installed in one of the 32 optical ports in the test section. A laser leveler's aid ensures that the laser is centered and parallel as it goes through the laser delivery probe from the mirror mounted on the optical rail. A rigid borescope installed in an optical port downstream of the vane trailing edge is connected to a high-speed intensifier and camera. The optics are mounted on optical tables furnished with leveling isolation dampers. These isolators are necessary to mitigate misalignment from the vibrations of the test rig.

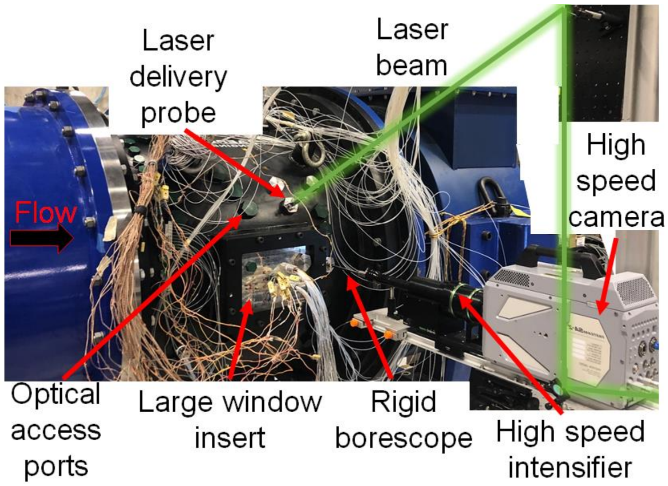

Figure 74: PSP optical setup in the turbine test section

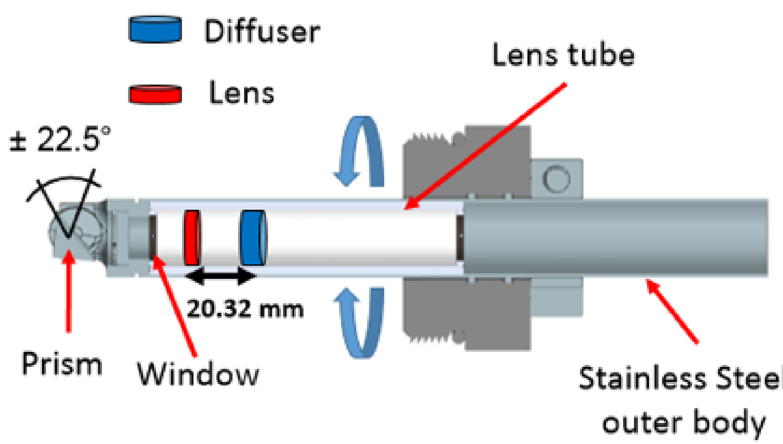

Figure 75: Schematic of the laser delivery probe

The laser delivery probe shown in Figure 75 is designed to be adjusted radially into and out of the flow path and rotated 360° around the probe shaft. Additionally, a prism at the bottom can be rotated 45° pitch-wise. A window with a visible anti-reflection coating is installed to seal the probe upstream of the prism and maximize light throughput to the reflector prism. A plano-convex positive lens with a 120 mm focal length and a 1500 grit ground glass diffuser is spaced out 20.32 mm in the lens tube. The diffuser first spread the laser beam and was refocused by the positive lens adjacent to the permanent window. The laser is aligned with a laser leveler's aid to ensure that the delivery path is concentric and parallel to the delivery probe axis. Figure 76a shows the laser alignment process. The laser probe yaw and pitch are first determined by centering the unexpanded beam in the region of interest. Afterward, the 12.7 mm optics are carefully installed to capture a homogeneous portion of the expanded laser within the region of interest. After the final check for a uniform, diffused beam on the vane surface area, the final laser probe position is fixed and marked. The rectangular large window opening, also shown in Figure 76b, provides access to mount the 3D-printed calibration dot target used for camera calibration and apply the PC binder and PtTFPP luminophore on the vane in-situ with the airbrush spray gun.

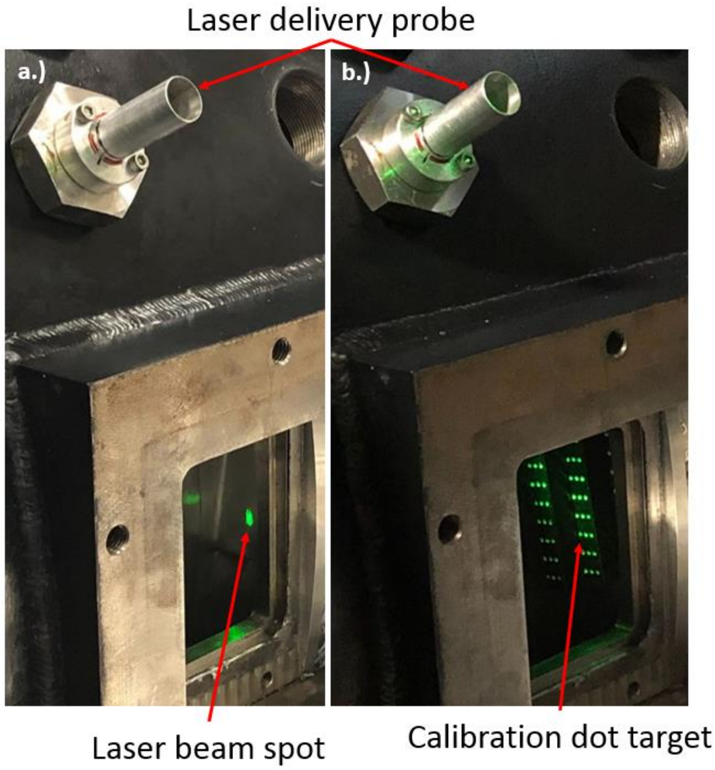

Figure 76: a) Laser beam spot aligned on vane without focusing lens or diffuser
b) 3D calibration dot target mounted on the vane for camera calibration

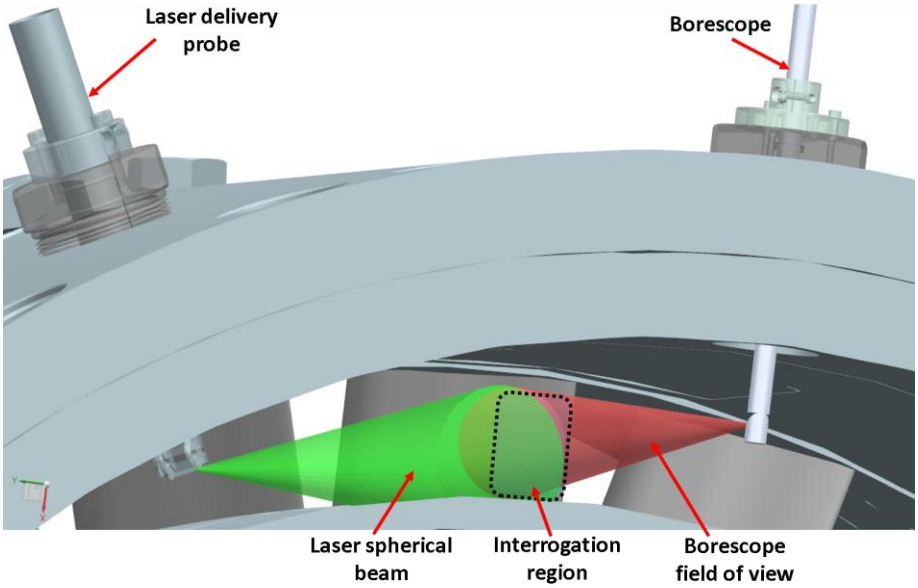

Figure 77: Close up view of the optical layout in the annular test section

A close-up view of the optical layout inside the test section is shown in Figure 77. Before installing the laser delivery probe in the test section, the spacing between the diffuser and focusing lens was precisely measured to produce a uniformly diffused beam with a 63.5 mm spot size. The 304.8 mm long rigid Hawkeye borescope has a 50° field-of-view (FOV) and provides the interrogation region near aft SS of the turbine vane. The borescope was aligned with an angle of view fixed at 90°. The maximum lens outer diameter is 7.95 mm, and a focusing lens is used to adjust and optimize the sharpness of the image for different distances. A SAZ Photron camera with a frame rate of 200 kHz and pixel resolution of 160x384 pixels is synchronized with a *HiCATT* (high-speed intensified camera attachment) and the quasi-continuous burst mode laser. TTL pulses from a Quantum Composer 9530 pulse generator are used to trigger the experiment timing signals shown in Figure 78. After every laser pulse, the camera acquires a series of 10 images, of which the first three useful images are used to model the pressure-sensitive luminescent lifetime.

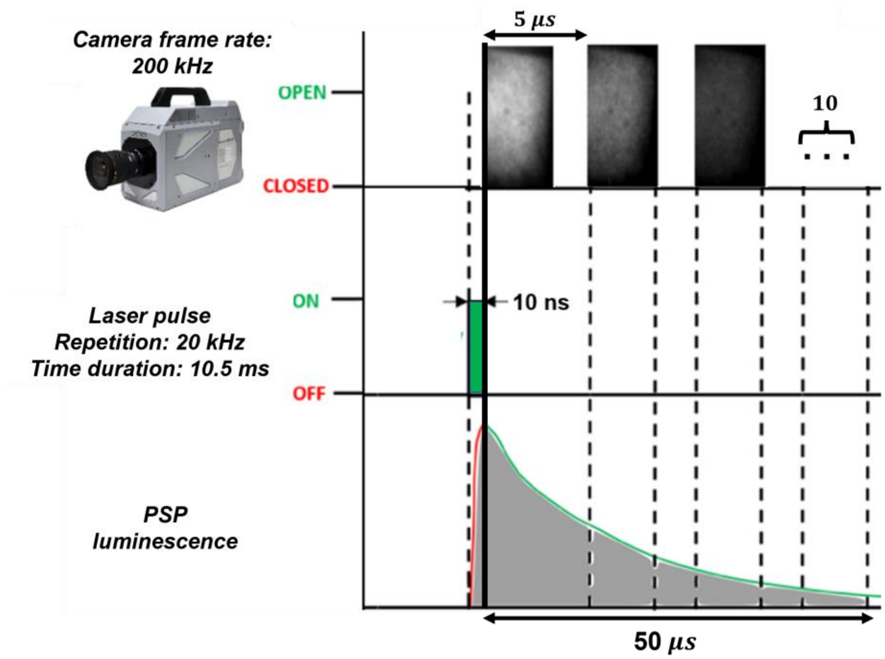

Figure 78: Timing chart for laser and camera synchronization

5.5 In-situ calibration procedure

The PSP is calibrated in-situ on the vane suction surface, with a vacuum pump connected to the wind tunnel from ambient pressure to 80 kPa in several steps. At each pressure level, the laser is triggered, and a feedback signal from the intensifier exposure is synchronized with pressure tappings data on an adjacent vane. The 10x10 binning data processing routine is applied to each image of cropped 88x128 pixels to calculate the single exponential lifetime. The relationship between pressure and lifetime is modeled using eq. (2). The comparison between the pressure tappings and the PSP calibration pressure retrieved from the regression coefficients averaged over 88 x 128 pixels is shown in Figure 79. The uncertainty bars in the ordinate are 95% of the readings among all the pixels calculated from PSP. The abscissa's uncertainty bars represent ± 0.05% of the full-scale pressure range of the reference Scanivalve DSA 3217 unit. The maximum difference between PSP and the pressure tappings from the calibration is 5100 Pa. The PSP thickness is measured at seven sectors on the painted surface, as summarized in Table 4. The most significant minimum to maximum variation was 27.1 μm at a location near the edge of the vane.

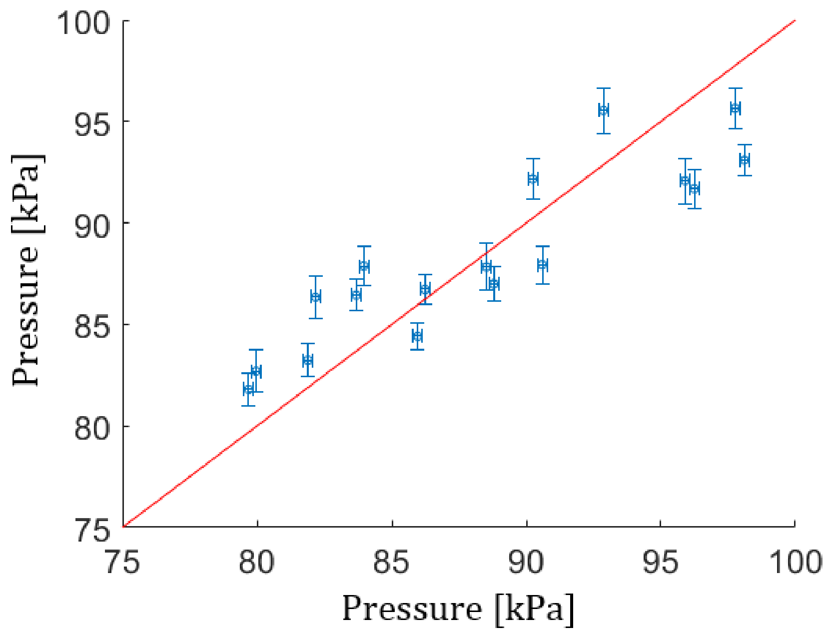

Figure 79: Comparison between PSP (ordinate) and reference pressure (abscissa), 1.96σ applied to PSP dataset

Table 4: PSP thickness measurements on turbine vane surface

Sector	1	2	3	4	5	6	7
Min [μm]	13.2	17.3	12.5	32.6	31.8	34.7	23.4
Max [μm]	35.1	32.7	39.6	55.2	46.4	49.7	29
Avg [μm]	22.1	25.4	21.6	39.3	38.0	43.8	25.8
σ [μm]	4.55	8.83	4.89	6.45	3.91	3.56	1.65

5.6 Time-averaged surface pressure

The CFD results agree with the static pressure tapping data at 50% span, depicted in Figure 80a. The pressure tappings on the vane pressure surface were not included since PSP was not applied on that surface. The calibration coefficients are applied to the wind-on experiment with test conditions summarized in Table 3. The normalized 2-D pressure distribution from the CFD simulations is compared to the 2-D normalized pressure from the PSP, as shown in Figure 80b. The PSP results are time-averaged for 3.4 ms.

The CFD results match well with the PSP results qualitatively. Both CFD and PSP pressure distributions show a gradual increase in pressure along the streamwise direction with higher pressures near the trailing edge in the aft section of the vane suction surface. Additionally, there is a gradual increase of pressure along the spanwise direction from the hub. The PSP results along the streamwise direction at 15% and 50% are compared with static pressure taps shown in Figure 81. The uncertainty bars from PSP represent the single standard deviation range on either side of the mean. The difference between the static pressure taps and the PSP at 50% span is 3160 Pa.

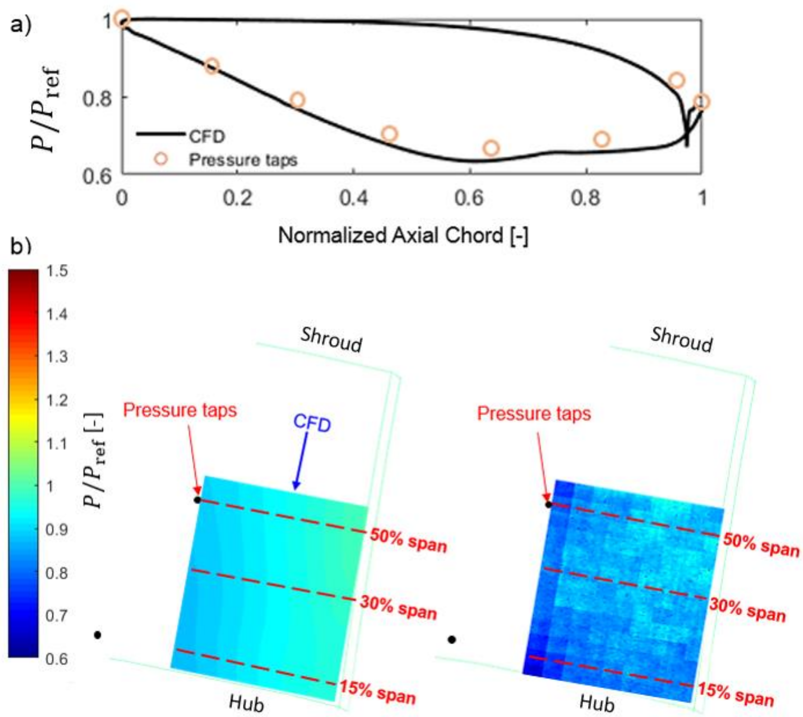

Figure 80: a) CFD comparison with pressure taps at 50% span b) 2D pressure map comparison between CFD and PSP

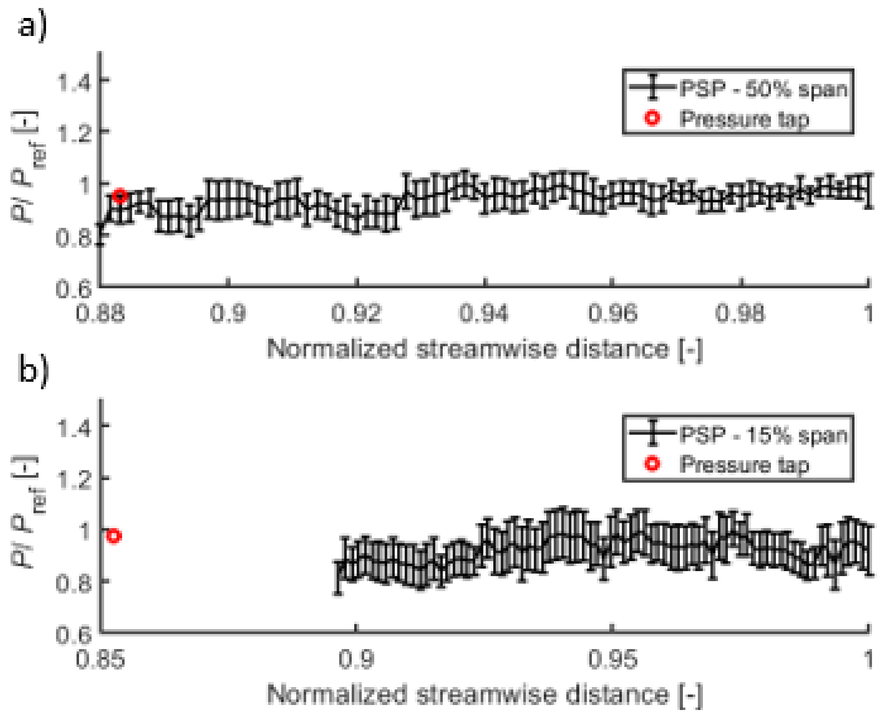

Figure 81: Comparison between PSP pressure profile and static pressure taps at 50% span and 15% span (bottom)

5.7 Time-resolved surface pressure

The time history of pressure data from two 5x5 bundles of pixels at 50% and 30% span are processed to evaluate the unsteady PSP results. The average pressure of 25 pixels is monitored within a time window of 2.3 ms. The pressure signal is repeated 100 times resulting in a time length of 0.23 seconds to improve the frequency resolution. The pressure signal's discrete Fourier transform (DFT) is calculated for two datasets (wind-off and wind-on conditions). At 50% span, the difference between wind-on and wind-off results is insignificant, as shown in Figure 82. Closer to the hub at 30% span, there is an increase in frequencies and pressure amplitude in the wind-on results than wind-off, as shown in Figure 83. The flow conditions near 50% span are less dominated by secondary flow structures and are therefore steady. Several researchers [57–59] have studied the horseshoe vortex system formation in low-speed flows. Wang et al. [57] identified a horseshoe vortex frequency of 2.5 Hz with an inlet velocity of 0.8 m/s in a linear cascade. We can expect several hundred Hz frequencies if we consider the same Strouhal number scaled to the high-speed test conditions.

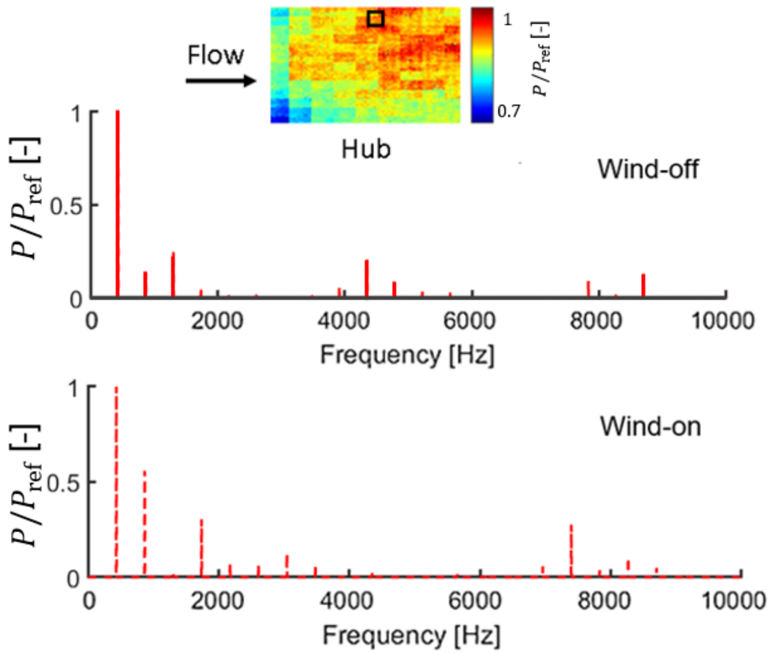

Figure 82: Unsteady data processed at 50% span a) DFT of wind-off with a window of 0.23 seconds, b) DFT of wind-on with a window of 0.23 seconds

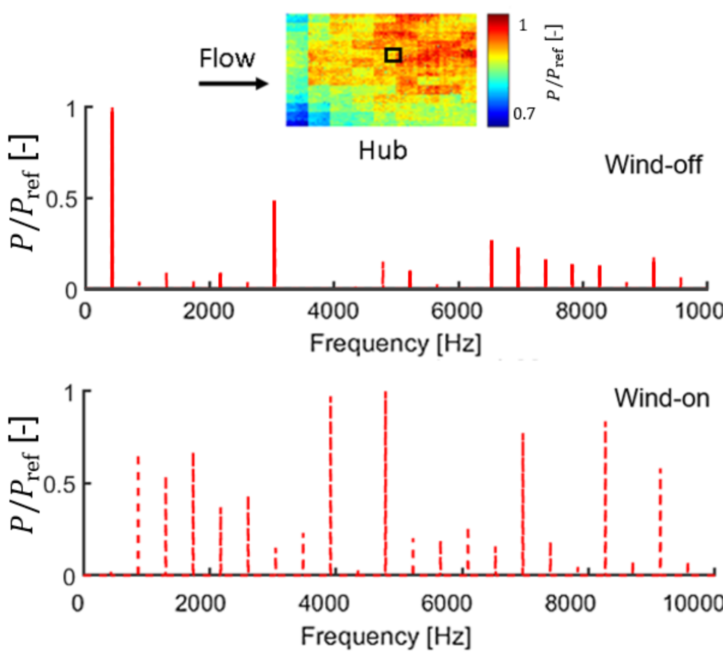

Figure 83: Unsteady data processed at 30% span a) DFT of wind-off with a window of 0.23 seconds, b) DFT of wind-on with a window of 0.23 seconds

CHAPTER 6: CONCLUSIONS

This doctoral study aimed to develop an optical surface technique for a new class of high-pressure turbines. The overall goal was subdivided into three main strategies: 1) a calibration procedure was created for a laser-based lifetime PSP method. The systematic evaluation of the calibration parameters, including luminescent lifetime and pressure correlation, pressure sensitivity, and signal-to-noise ratio, provided an improved understanding of time-resolved luminescent lifetime methods. 2) The pulse lifetime PSP method was tested in a high spatial pressure gradient flow field, revealing insights into the spatial-temporal analysis of the shock and shear layer interaction. 3) The procedure for pulse lifetime PSP was finally successfully demonstrated on a high-pressure turbine vane annular cascade at engine representative conditions. Sections 6.1 to 6.3 summarize how each research objective was completed.

6.1 Accuracy Assessment of a Pulse Lifetime Procedure with no-flow

A systematic evaluation of the pulse lifetime calibration procedure was investigated by manufacturing and testing a pressure chamber operated under vacuum and above ambient pressure with optical access to excite and capture the luminescence decay of a sample PSP coupon. The calibration results were analyzed to evaluate the accuracy, reliability, and uncertainty of the pulse lifetime method.

Precise measurements of the calibration coupon’s thickness indicated relatively larger PSP thickness near the edge of the coupon than at the center. This finding was corroborated with a decrease in the luminescent lifetime towards the center of the calibration coupon. Reduced coating thickness indicates a reduced diffusion timescale and shorter lifetimes. Both intensity and lifetime variations were reduced when divided by a reference image at constant pressure and temperature. After applying the image ratio, the luminescent lifetime coefficient of variation was reduced from 3.2% to 1.07%, while the intensity coefficient of variation was reduced from 15.3% to 1.12%. The more significant improvement of intensity variation explained that the luminescent lifetime is less sensitive to non-uniform illumination, thickness, or dye concentration than the luminescent intensity. When comparing vacuum to the ambient intensity map, there was a less than 1% difference between the luminescent intensity variation. However, the magnitude of intensity was significantly increased at lower pressure. This result implies that laser intensity and beam profile are consistent at different calibration pressures (small or large O_2 concentrations). The increased intensity magnitude at vacuum (low O_2 diffusion) compared to a reference pressure (higher O_2 diffusion) is mainly due to a change in O_2 quencher interaction with excited luminophores.

A single exponential decay regression model of luminescence decay yielded a coefficient of determination greater than 0.993 for all calibration pressures. A 2nd order polynomial demonstrated the best fit between pressure and luminescent lifetime with a maximum relative difference of 2% between reconstructed pressure from PSP and pressure calibrator reading. The pressure sensitivity was more significant at lower pressures due to less oxygen quenching.

6.2 Uncertainty Quantification and Unsteady Analysis of the Pulse Lifetime Method in a Linear Test Section

The pulse lifetime PSP method was demonstrated for aerodynamic wind tunnel testing in a linear test section (TRL 1-2) with high spatial pressure gradients. The pulse lifetime calibration, overall measurement uncertainty, and error propagation were evaluated. A data processing methodology was applied to remove images with a low signal-to-noise ratio, reduce uncertainty, and select an optimal binning bundle of pixels for spatial-temporal pressure analysis. A sensitivity analysis of the calibration method was performed to find the parameters with a substantial effect on final pressure uncertainty.

A parametric study of the data used for the single exponential decay model showed that the first point on the intensity decay curve might be sensitive to residual laser energy or reflection. Additionally, the advantage of using more points at vacuum conditions is not automatically true at ambient conditions since the intensity decays to the ground state much faster. A minimum of 3 points used to fit a single exponential decay with the 2nd or 3rd point on the decay curve as a start point yielded a high coefficient of determination. Over the laser burst duration of 10.8 milliseconds, the average lifetime was constant for each laser pulse at ambient and 56.33 kPa—however, the average lifetime at 18.14 kPa varied significantly. The increased variation at vacuum is related to the increased variation in luminescence lifetime among all pixels.

From the pixel binning analysis, it was evident that the variation in the luminescent lifetime gradually increases from high to low pressures. However, the advantage of binning is more effective at low pressures. For example, the improvement in coefficient of variation between 5x5 and 50x100 binning bundle data is 10.2% and 5.2% at 18.41 kPa, compared to 6.5% and 3.5% at ambient pressure. After applying the 10x10 binning bundle for analysis, the relative difference between reconstructed pressure from PSP and pressure tappings was 4% at 49 kPa, and less than 1% at ambient pressure.

The luminescent lifetime ratio was the most sensitive variable to the final pressure uncertainty from the sensitivity analysis. Since it is the highest power term from the 2nd order polynomial, it has the most significant contribution to uncertainty. The second polynomial coefficient was the most sensitive to the pressure uncertainty between the polynomial coefficients, while the first polynomial coefficient was the least sensitive. The final summary of the overall uncertainty analysis showed that the relative uncertainty in the luminescent lifetime ratio directly affects the pressure uncertainty.

The time-averaged spatially resolved surface pressure from PSP was consistent with the CFD RANS results and Shadowgraph experiment results for all binning bundles in spanwise and streamwise directions. The PSP results showed a pressure increase from the first compression wave, followed by the first expansion region. Further downstream, a first separation shock appears followed by a separation region due to the onset of the second wavy surface downstream. A second compression region repeats the flow pattern with pressure rise, followed by an expansion fan and separation shock. The time-averaged, spanwise-averaged PSP results agree with the static pressure tappings data within the error bars from the PSP calibration.

The spatial-temporal analysis revealed that the unsteadiness in the expansion and separation location is relatively more intense than in the recirculation and compression regions. Moreover, the second wave has a stronger unsteadiness near the separation shock location than the first wave. For example, the pressure variation is as high as 60% of the average pressure near the second shock, consistent for all test conditions. A histogram of the pressure in the separation location regions and shock location regions showed that the pressure is centered around the average pressure at the shock location. However, a 10% increase and a 5% decrease from the average pressure in the separation locations confirm the relatively high unsteadiness levels in the separation location region.

6.3 Application of the Pulse Lifetime PSP Method in an Annular Test Section

The pulse lifetime PSP technique was applied to a high-pressure turbine vane suction surface in the Big Rig for Annular Stationary Turbine Analysis (BRASTA) test section at the PETAL lab. A 10x10 binning bundle was applied to calibration and wind-on PSP data.

The procedure for pulse lifetime PSP measurements at 20 kHz is successfully demonstrated in an annular test section at engine representative conditions. The PSP thickness measurements showed that the largest minimum to maximum variation was 27.1 μm with a difference of 5100 Pa between the PSP and pressure taps from the PSP calibration. The two-dimensional normalized static pressure results in the interrogation region showed a gradual increase of pressure from the hub in the spanwise direction. Additionally, the pressure increased towards the trailing edge along the flow direction, and the difference between the PSP and pressure taps at mid-span was 3160 Pa. The DFT of the unsteady pressure signal showed increased frequency content in wind-on conditions compared to wind-off at both 30% and 50% span. At a 30% span, an increase in frequencies and pressure amplitude was identified compared to the mid-span region.

This doctoral work covered developing and applying an optical surface pressure measurement technique, from simple experiments on a small research coupon to experimental demonstrations in a linear test section and an annular test section with precise calibrations and uncertainty analysis. As turbine designs become more efficient, optical surface measurements can provide a robust tool to evaluate differences between airfoil designs and validate computational design tools.

REFERENCES

[1] Sieverding, C. H., 1985, *Secondary Flows in Straight and Annular Turbine Cascades in "Thermodynamics and Fluid Mechanics of Turbomachinery", NATO ASI Series E. No. 97A.*

[2] Sieverding, C. H., 1985, "Recent Progress in the Understanding of Basic Aspects of Secondary Flows in Turbine Blade Passages," J. Eng. Gas Turbines Power, **107**(2), pp. 248–257.

[3] Yoon, S., Denton, J., Curtis, E., Longley, J., and Pullan, G., 2013, "Improving Intermediate Pressure Turbine Performance by Using a Nonorthogonal Stator," J. Turbomach., **136**(2), pp. 1–8.

[4] Pullan, G., 2006, "Secondary Flows and Loss Caused by Blade Row Interaction in a Turbine Stage," J. Turbomach., **128**(3), pp. 484–491.

[5] Govardhan, M., and Kumar, K. N., 2011, "Secondary Flow Loss Reduction in a Turbine Cascade with a Linearly Varied Height Streamwise Endwall Fence," Int. J. Rotating Mach., **2011**.

[6] Rottmeier, F., 2003, "Experimental Investigation of a Vibrating Axial Turbine Cascade in Presence of Upstream Generated Aerodynamic Gusts," **2758**.

[7] Paniagua, G., Des, D., Vzw, F., and Grant, E., 2013, "Unsteady Shock Waves Vortex Shedding Entanglement in a Transonic Turbine Cascade Report Date : July 2013 Final Report from 1 July 2012 to 31 December 2012 Distribution Statement A : Approved for Public Release Distribution Is Unlimited . Air Force Researc," (July).

[8] Dring, R. P., and Joslyn, H. D., 2018, "Turbine Rotor-Stator Interaction," **104**(October 1982), pp. 729–742.

[9] Andreoli, V., Braun, J., Paniagua, G., De Maesschalck, C., Bloxham, M., Cummings, W., and Langford, L., 2019, "Aerothermal Optimization of Fully Cooled Turbine Blade Tips," J. Turbomach., **141**(6), pp. 1–10.

[10] Peterson, J. I., and Fitzgerald, R. V., 1980, "New Technique of Surface Flow Visualization Based on Oxygen Quenching of Fluorescence," Rev. Sci. Instrum., **51**(5), pp. 670–671.

[11] Bowen, E. J., 1954, "Fluorescence Quenching in Solution and in the Vapour State," Trans. Faraday Soc., **50**, pp. 97–102.

[12] Ardasheva, M. M., Nevskii, L. B., and Pervushin, G. E., 1985, "Measurement of Pressure Distribution by Means of Indicator Coatings," J. Appl. Mech. Tech. Phys., **26**(4), pp. 469–474.

[13] Kavandi, J., Callis, J., Gouterman, M., Khalil, G., Wright, D., Green, E., Burns, D., and McLachlan, B., 1990, "Luminescent Barometry in Wind Tunnels," Rev. Sci. Instrum., **61**(11), pp. 3340–3347.

[14] McPhie, P., 2000, *Principles of Fluorescence Spectroscopy, Second Ed. Joseph R. Lakowicz*.

[15] Liu, T., Sullivan, P. J., 2004, *Pressure and Temperature Sensitive Paints*.

[16] Gregory, J. W., 2002, "UNSTEADY PRESSURE MEASUREMENTS IN A TURBOCHARGER COMPRESSOR USING POROUS PRESSURE-SENSITIVE PAINT," Purdue University.

[17] Gregory, J. W., Sakaue, H., Liu, T., and Sullivan, J. P., 2014, "Fast Pressure-Sensitive Paint for Flow and Acoustic Diagnostics," Annu. Rev. Fluid Mech., **46**(1), pp. 303–330.

[18] Sakaue, H., Morita, K., Iijima, Y., and Sakamura, Y., 2013, "Response Time Scales of Anodized-Aluminum Pressure-Sensitive Paints," Sensors Actuators, A Phys., **199**, pp. 74–79.

[19] Numata, D., Fujii, S., Nagai, H., and Asai, K., 2017, "Ultrafast-Response Anodized-Aluminum Pressure-Sensitive Paints for Unsteady Flow Measurement," AIAA J., **55**(4), pp. 1118–1125.

[20] Panda, J., Roozeboom, N. H., and Ross, J. C., 2019, "Wavenumber-Frequency Spectra on a Launch Vehicle Model Measured via Unsteady Pressure-Sensitive Paint," AIAA J., **57**(5), pp. 1801–1817.

[21] Sakaue, H., and Sullivan, J. P., 2001, "Time Response of Anodized Aluminum Pressure-Sensitive Paint," AIAA J., **39**(10), pp. 1944–1949.

[22] Baron, A. E., Danielson, J. D. S., Gouterman, M., Wan, J. R., Callis, J. B., and McLachlan, B., 1993, "Submillisecond Response Times of Oxygen-Quenched Luminescent Coatings," Rev. Sci. Instrum., **64**(12), pp. 3394–3402.

[23] Gregory, J. W., Asai, K., Kameda, M., Liu, T., and Sullivan, J. P., 2008, "A Review of Pressure-Sensitive Paint for High-Speed and Unsteady Aerodynamics," Proc. Inst. Mech. Eng. Part G J. Aerosp. Eng., **222**(2), pp. 249–290.

[24] Crafton, J., Forlines, A., Palluconi, S., Hsu, K. Y., Carter, C., and Gruber, M., 2011, “Investigation of Transverse Jet Injections in a Supersonic Crossflow Using Fast Responding Pressure-Sensitive Paint,” 29th AIAA Appl. Aerodyn. Conf. 2011.

[25] Scroggin, A. M., Slamovich, E. B., Crafton, J. W., Lachendro, N., and Sullivan, J. P., 1999, “Porous Polymer/Ceramic Composites for Luminescence-Based Temperature and Pressure Measurement,” Mat. Res. Soc. Symp. Proc., **560**, pp. 347–352.

[26] Peng, D., and Liu, Y., 2020, “Fast Pressure-Sensitive Paint for Understanding Complex Flows: From Regular to Harsh Environments,” Exp. Fluids, **61**(1), pp. 1–22.

[27] Gregory, J. W., and Sullivan, J. P., 2006, “Effect of Quenching Kinetics on Unsteady Response of Pressure-Sensitive Paint,” AIAA J., **44**(3), pp. 634–645.

[28] Sakaue, H., Gregory, J. W., Sullivan, J. P., and Raghu, S., 2002, “Porous Pressure-Sensitive Paint for Characterizing Unsteady Flowfields,” AIAA J., **40**(6), pp. 1094–1098.

[29] Sugimoto, T., Sugioka, Y., Numata, D., Nagai, H., and Asai, K., 2017, “Characterization of Frequency Response of Pressure-Sensitive Paints,” AIAA J., **55**(4), pp. 1460–1464.

[30] Peng, D., Jensen, C. D., Juliano, T. J., Gregory, J. W., Crafton, J., Palluconi, S., and Liu, T., 2013, “Temperature-Compensated Fast Pressure-Sensitive Paint,” AIAA J., **51**(10), pp. 2420–2431.

[31] Kameda, M., 2012, “Effect of Luminescence Lifetime on the Frequency Response of Fast-Response Pressure-Sensitive Paints,” Nihon Kikai Gakkai Ronbunshu, B Hen/Transactions Japan Soc. Mech. Eng. Part B, **78**(795), pp. 1942–1950.

[32] McMullen, R. M., Huynh, D. P., Gregory, J. W., and Crafton, J., 2013, “Dynamic Calibrations for Fast-Response Porous Polymer/Ceramic Pressure-Sensitive Paint,” AIAA Gr. Test. Conf., pp. 1–18.

[33] Ruyten, W., Sellers, M., Air, A., and Base, F., 2004, “PRESSURE-SENSITIVE PAINT PtTFPP IN FIB *,” (January), pp. 1–12.

[34] Carraway, E. R., Demas, J. N., and DeGraff, B. A., 1991, “Luminescence Quenching Mechanism for Microheterogeneous Systems,” Anal. Chem., **63**(4), pp. 332–336.

[35] Goss, L. P., Trump D. D., Sarka, B., 2000, “Multi-Dimensional Time-Resolved Pressure-Sensitive-Paint Techniques: A Numerical and Experimental Comparison.”

[36] Bell, J. H., 2001, “Accuracy Limitations of Lifetime-Based Pressure-Sensitive Paint (PSP) Measurements,” ICIASF Rec. Int. Congr. Instrum. Aerosp. Simul. Facil., pp. 5–16.

[37] Hartmann, P., Leiner, M. J. P., and Lippitsch, M. E., 1995, “Response Characteristics of Luminescent Oxygen Sensors,” Sensors Actuators B. Chem., **29**(1–3), pp. 251–257.

[38] Slipchenko, M. N., Miller, J. D., Roy, S., Gord, J. R., Danczyk, S. A., and Meyer, T. R., 2012, “Quasi-Continuous Burst-Mode Laser for High-Speed Planar Imaging,” Opt. Lett., **37**(8), p. 1346.

[39] Ayers, Z. M., Fisher, J. M., Brown, A., Son, S. F., and Meyer, T. R., 2019, “KHz-Rate Temperature Imaging Using Time-Domain Thermographic Phosphorescence,” AIAA Scitech 2019 Forum, (January), pp. 1–6.

[40] Inman, D., Gonzalez Cuadrado, D., Andreoli, V., Fisher, J., Paniagua, G., Aye-Addo, N., Bhatnagar, L., Lozano, F., Meyer, T., and Bloxham, M., 2020, “Particle Image Velocimetry in a High-Pressure Turbine Stage at Aerodynamically Engine Representative Conditions,” J. Eng. Gas Turbines Power, (c).

[41] Hayashi, T., and Sakaue, H., 2017, “Dynamic and Steady Characteristics of Polymer-Ceramic Pressure-Sensitive Paint with Variation in Layer Thickness,” Sensors (Switzerland), **17**(5).

[42] Smyser, M. E., Rahman, K. A., Slipchenko, M. N., Roy, S., and Meyer, T. R., 2018, “Compact Burst-Mode Nd:YAG Laser for KHz–MHz Bandwidth Velocity and Species Measurements,” Opt. Lett., **43**(4), p. 735.

[43] Paniagua, G., Cuadrado, D., Saavedra, J., Andreoli, V., Meyer, T., Solano, J. P., Herrero, R., Meyer, S., and Lawrence, D., 2019, “Design of the Purdue Experimental Turbine Aerothermal Laboratory for Optical and Surface Aerothermal Measurements,” J. Eng. Gas Turbines Power, **141**(1), pp. 1–13.

[44] Moffat, R. J., 1988, “Describing the Uncertainties in Experimental Results,” Exp. Therm. Fluid Sci., **1**(1), pp. 3–17.

[45] Braun, J., Paniagua, G., Falempin, F., and Le Naour, B., 2020, “Design and Experimental Assessment of Bladeless Turbines for Axial Inlet Supersonic Flows,” J. Eng. Gas Turbines Power, **142**(4).

[46] Liu, T., Burner, A. W., Jones, T. W., and Barrows, D. A., 2012, “Photogrammetric Techniques for Aerospace Applications,” Prog. Aerosp. Sci., **54**, pp. 1–58.

[47] Liu, T., Cattafesta, L. N., Radeztsky, R. H., and Burner, A. W., 2000, “Photogrammetry Applied to Wind-Tunnel Testing,” AIAA J., **38**(6), pp. 964–971.

[48] Sellen, M. E., and Brill, J. A., 1994, "Demonstration Test of Pressure Sensitive Paint in the Aedc 16-Ft Transonic Wind Tunnel Using the TST Model," AIAA 25th Plasmadynamics Lasers Conf. 1994.

[49] Navarra, K. R., Rabe, D. C., Fonov, S. D., Goss, L. P., and Hah, C., 2001, "The Application of Pressure- and Temperature-Sensitive Paints to an Advanced Compressor," J. Turbomach., **123**(4), p. 823.

[50] Jordan, J. D., Watkins, A. N., Davis, J. C. P. N., Weaver, W. L., Dale, G. A., Navarra, K. R., Urban, J. R., Devoid, W. E., Strange, R. A., and St, M., 1999, "Large-Scale Commercial-Engine Test Stand."

[51] Neal Watkins, A., Leighty, B. D., Lipford, W. E., Wong, O. D., Goodman, K. Z., Crafton, J., Forlines, A., Goss, L. P., Gregory, J. W., and Juliano, T. J., 2012, "Deployment of a Pressure Sensitive Paint System for Measuring Global Surface Pressures on Rotorcraft Blades in Simulated Forward Flight," 28th AIAA Aerodyn. Meas. Technol. Gr. Testing, Flight Test. Conf. 2012, (December 2011).

[52] Juliano, T. J., Kumar, P., Peng, D., Gregory, J. W., Crafton, J., and Fonov, S., 2011, "Single-Shot, Lifetime-Based Pressure-Sensitive Paint for Rotating Blades," Meas. Sci. Technol., **22**(8).

[53] Melorose, J., Perroy, R., and Careas, S., 2015, "Development of a Single-Shot Lifetime PSP Measurements Technique for Rotating Surfaces," Statew. Agric. L. Use Baseline 2015, **1**.

[54] Wong, O. D., Watkins, a N., Goodman, K. Z., Crafton, J., Forlines, A., Goss, L., Gregory, J. W., and Juliano, T. J., 2012, "Blade Tip Pressure Measurements Using Pressure Sensitive Paint," AHS 68th Annu. Forum.

[55] Haselbach, F., 2008, "Axial Flow High Pressure Turbine Design," Aero Engine Des. State Art Turbofans Towar. Innov. Archit. (Proceedings VKI Lect. Ser. 2008-03), von Karman Institute, Brussels, Belgium, pp. 1–91.

[56] Shahpar, S., and Lapworth, L., 2003, "PADRAM: Parametric Design and Rapid Meshing System for Turbomachinery Optimisation," *Proceedings of the ASME Turbo Expo 2003, Collocated with the 2003 International Joint Power Generation Conference, Volume 6: Turbo Expo 2003, Parts A and B. Atlanta, Georgia, USA. June 16–19, 2003.*, pp. 579–590.

[57] Wang, H. P., Olson, S. J., Goldstein, R. J., and Eckert, E. R. G., 1995, "Flow Visualization in a Linear Turbine Cascade of High Performance Turbine Blades," Proc. ASME Turbo

Expo, **4**(January), pp. 1–8.

[58] Gross, A., Marks, C. R., and Sondergaard, R., 2017, "Numerical Investigation of Low-Pressure Turbine Junction Flow," AIAA J., **55**(10), pp. 3617–3621.

[59] Cui, J., Nagabhushana Rao, V., and Tucker, P., 2016, "Numerical Investigation of Contrasting Flow Physics in Different Zones of a High-Lift Low-Pressure Turbine Blade," J. Turbomach., **138**(1), pp. 1–10.

[60] Lavagnoli, S., 2019, "Design Considerations for Tip Clearance Control and Measurement on a Turbine Rainbow Rotor With Multiple Blade Tip Geometries," **139**(April 2017), pp. 1–10.

[61] Li, B., 2017, "Superfast 3D Shape Measurement With Application To Flapping Wing Mechanics Analysis," (August).

APPENDIX A: PULSE LIFETIME PSP APPLIED TO A FIN-PLATE HEAT EXCHANGER

Experimental plan:

The region of interest (ROI) painted has dimensions of 1.8” x 1.2” and is depicted in Figure A1 and Figure A2. This ROI was chosen since it contains the most significant pressure gradient on the fins’ domain and an array of pressure taps for the paint calibration. The tests were performed at the Mach 0.3 conditions with the heater on and off.

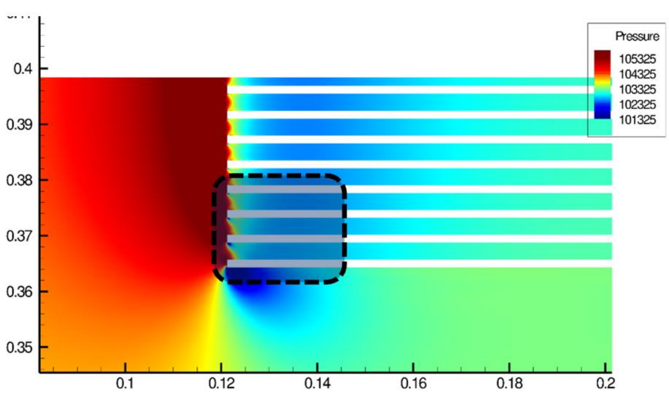

Figure A - 1: CFD surface pressure results and ROI for SACOC experiment

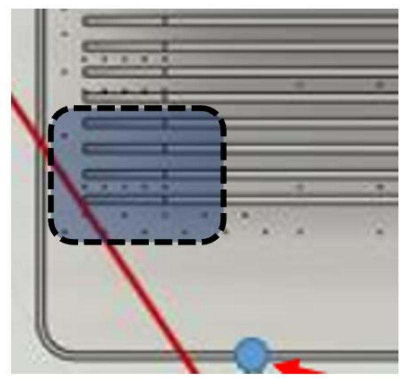

Figure A - 2: CAD schematic with static pressure tapping holes and ROI for SACOC experiment

Test conditions:

Po_1	$110\ kPa$
Ps_{exit}	$103.3\ kPa$
$Mach$	0.3
$To_1 Ps_{exit}$	$300\ K$
$Po_1 - Ps_{exit}$	$4.8\ kPa$

PSP coating application on fin-plate in-situ:

A Platinum tetra-fluorenyl porphyrin (PtTFPP) luminophore with a polymer ceramic binder from Innovative Scientific Solutions, Inc. was applied to the base plate and the fins. At ambient conditions, the luminophore has a luminescent lifetime of 10 micro-seconds (16 kHz cutoff frequency response). The absorptive spectrum of the paint has peak efficiencies at the Soret band (395 nm) and Q-band (541 nm), and the emission spectrum has a peak efficiency near 650 nm. The paint formula has three components: The binder is made up of parts A and B, and Part C is the luminophore solution. Part A's volume is determined based on the interrogation region of interest and paint thickness required for the experiment. A graduated cylinder and syringe are used to measure 4% of Part A from Part B. Parts A and B are combined in a jar with a tight lid and shaken thoroughly. An Iwata airbrush precise for fine and coarse brush painting is used to apply several coating layers of the binder mixture until the required thickness is achieved. After coating the binder, the paint is dried at room temperature for an hour. Finally, part C is poured into a thoroughly cleaned airbrush and sprayed on top of the binder until uniformly pale pink. The process of painting the geometry is shown in Figures A3-A6. Masking tape and needles were used to cover the orifice holes for static pressure instrumentation and avoid painting outside the interrogation region.

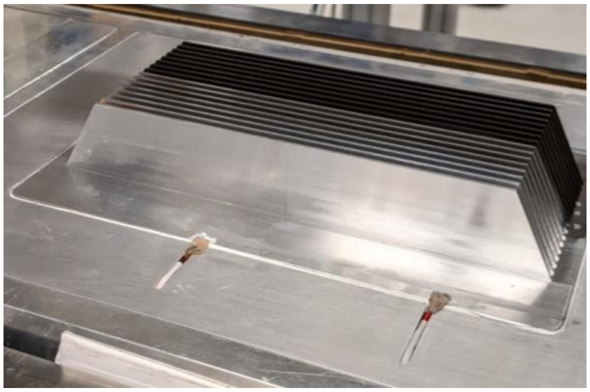

Figure A - 3: Plate-fin mounted in LEAF

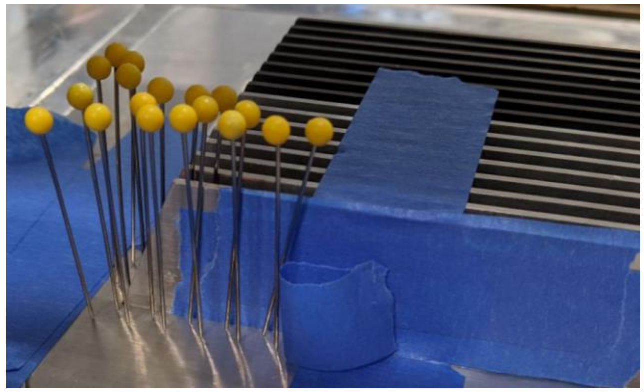

Figure A - 4: Setup before application of PSP coating

Figure A - 5: Side view of applied PSP to the plate-fin test article

Figure A - 6: Top view of applied PSP to the plate-fin test article

Optical setup and alignment:

The lifetime-based technique requires a modulated light source (i.e., laser, modulated LEDs, or flash lamps). A state-of-the-art quasi-continuous burst-mode Nd: YAG laser was used as a light source to excite the paint at 532 nm (2nd harmonic output of the laser). The maximum excitation of the paint is limited by the luminescent lifetime of the luminophore, which provides a window of 50 μs to capture the complete fluorescence decay at ambient pressure between laser pulses. The duration of the intensity decay to 99% of its initial value at the lowest calibration pressure determines the time between each laser pulse. A spherical diffuser and a plano-convex focusing lens produce a closely elliptical uniform laser beam spot on the test article.

The optical path for the laser beam and camera mounting position is shown in Figure A7. The laser beam was guided through a series of Nd: YAG mirrors and a 1500 grit diffuser lens to provide uniform illumination on the wavy surface. A SAZ Photron CMOS camera was sampled at 200 kHz with a 160x384 spatial resolution to capture the fluorescence decay. A 532 nm notch filter and 610 nm long-pass optical filter were installed to dampen the incident laser reflections.

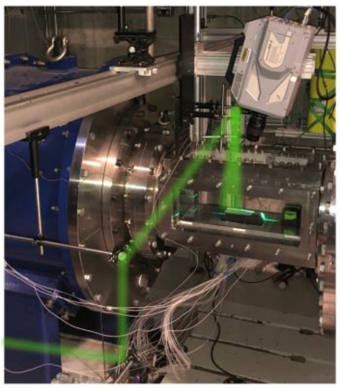

Figure A - 7: Optical setup with the laser beam path

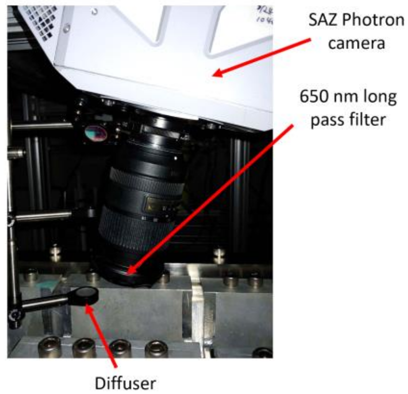

Figure A - 8: Close-up view of the camera with focusing lens and diffuser

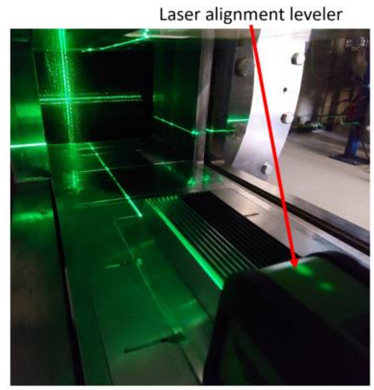

Figure A - 9: Laser leveler used to align the laser beam

Camera calibration

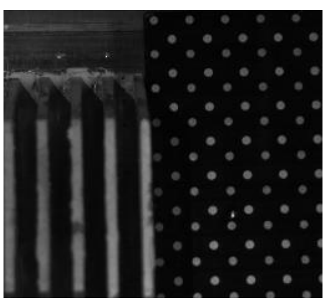

Figure A - 10: Dot target on the base plate

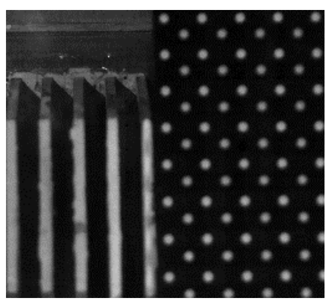

Figure A - 11: Dot target on machined 1" block

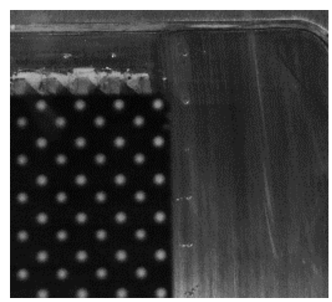

Figure A - 12: Dot target on top of the fins

PSP thickness measurements:

A Dualscope FMP40C system with an FD13H spring-loaded measurement probe was used to precisely measure the PSP coating thickness. The FD13H probe can be used as magnetic inductive for ferrous metals or eddy current for paint, varnish, or plastic coatings applied on non-ferrous metals. A coil wrapped around the ferrite core is induced with an excitation current for the eddy current test method. The generated high-frequency magnetic field sends loops of electrical current into a base material in planes perpendicular to the magnetic field. The resulting magnetic field signal's obtained measurement is converted to a coating thickness value with an accuracy of 2% of the nominal value. The probe tip is made up of a hard metal material and has a diameter of 4 mm.

A corrective calibration procedure is applied before each thickness measurement. First, the uncoated or unpainted base material (aluminum) is measured by the probe five times in the same approximate area. After the calibration of the base material, two standard thin calibration foils with a precise thickness rating are placed on the unpainted material. Both thin foils are measured five times each to complete the corrective calibration. After the calibration procedure, multiple areas of the PSP coating are measured, as shown in Figure A13, for a total of 1071 data points. The distribution across the entire PSP coupon surface is shown in Figure A14.

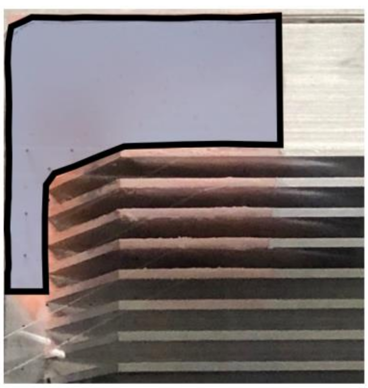

Figure A - 13: PSP thickness measurement region

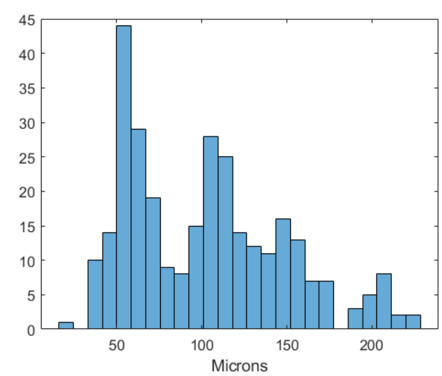

Figure A - 14: Histogram of thickness measurements on the base plate

Calibration results:

Day 1:

Heated plate (30° C):

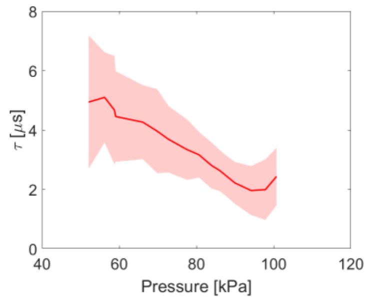

Figure A - 15: Lifetime calculated for calibration A with 95% confidence interval error band

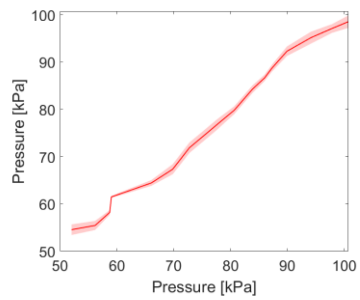

Figure A - 16: Reconstructed PSP calibration pressure with 95% confidence interval error band

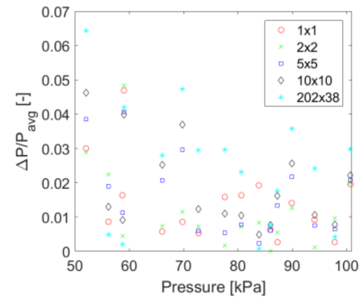

Figure A - 17: Relative difference between PSP calibration pressure and the static pressure tappings

Ambient temperature (25° C):

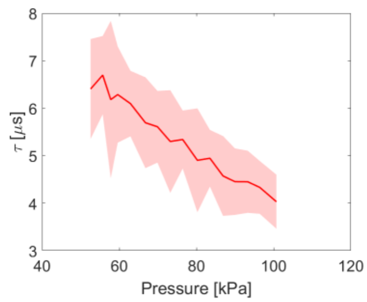

Figure A - 18: Lifetime calculated for calibration B with 95% confidence interval error band

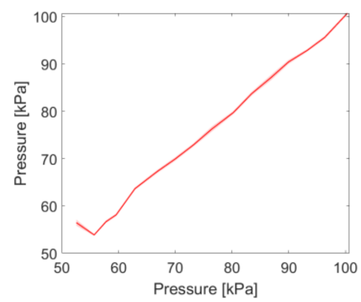

Figure A - 19: Reconstructed PSP calibration pressure with 95% confidence interval error band

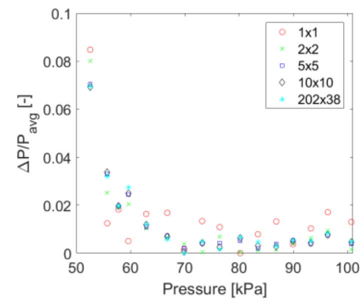

Figure A - 20: Relative difference between PSP calibration pressure and static pressure tappings

Day 2:

Ambient temperature (25° C):

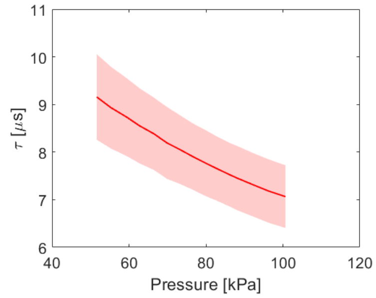

Figure A - 21: Lifetime calculated for calibration C with 95% confidence interval error band

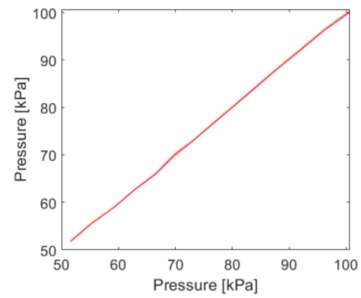

Figure A - 22: Reconstructed PSP calibration pressure with 95% confidence interval error band

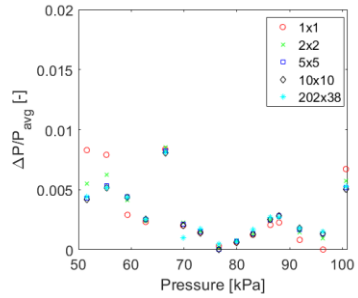

Figure A - 23: Relative difference between PSP calibration pressure and static pressure tappings

Heated plate (50° C):

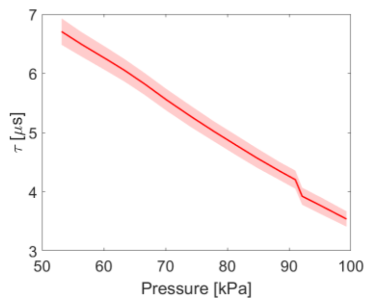

Figure A - 24: Lifetime calculated for calibration D with 95% confidence interval error band

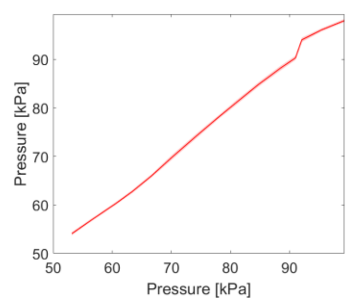

Figure A - 25: Reconstructed PSP calibration pressure with 95% confidence interval error band

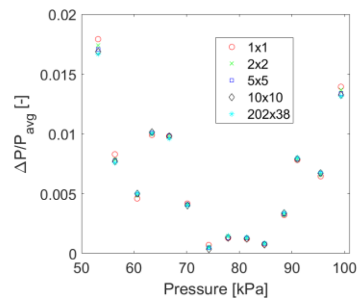

Figure A - 26: Relative difference between PSP calibration pressure and static pressure tappings

No flow data at three different calibration pressures:

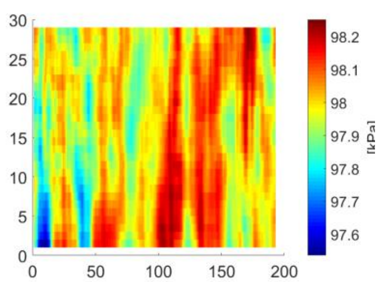

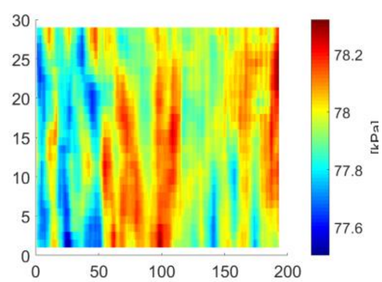

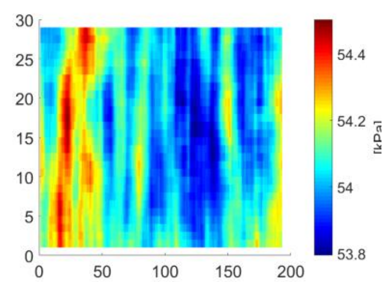

APPENDIX B: DATA PROCESSING CHART FOR PULSE LIFETIME PSP CALIBRATION METHOD

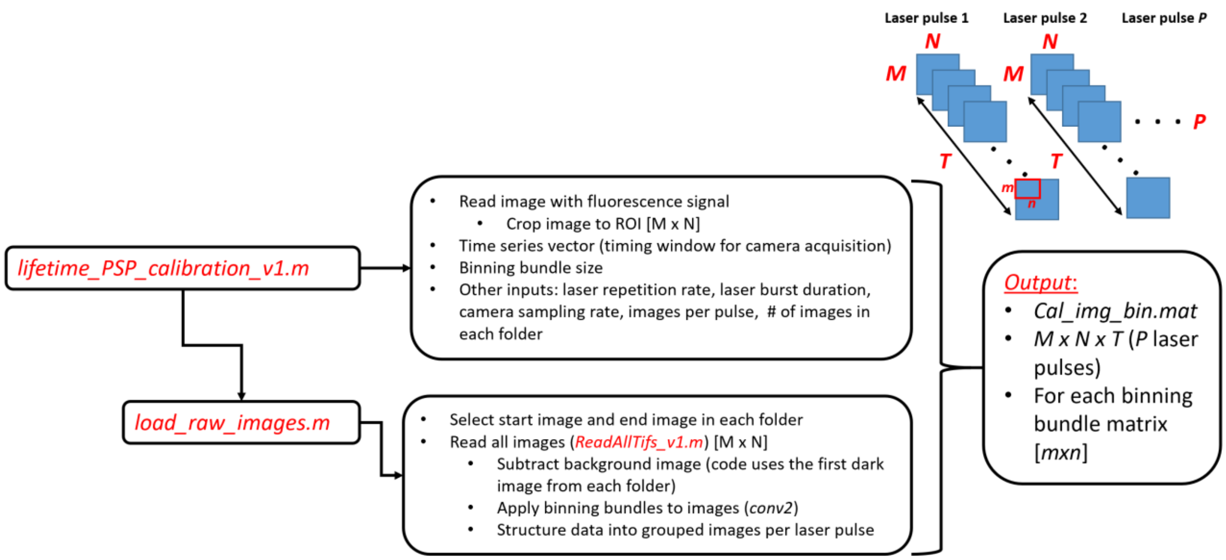

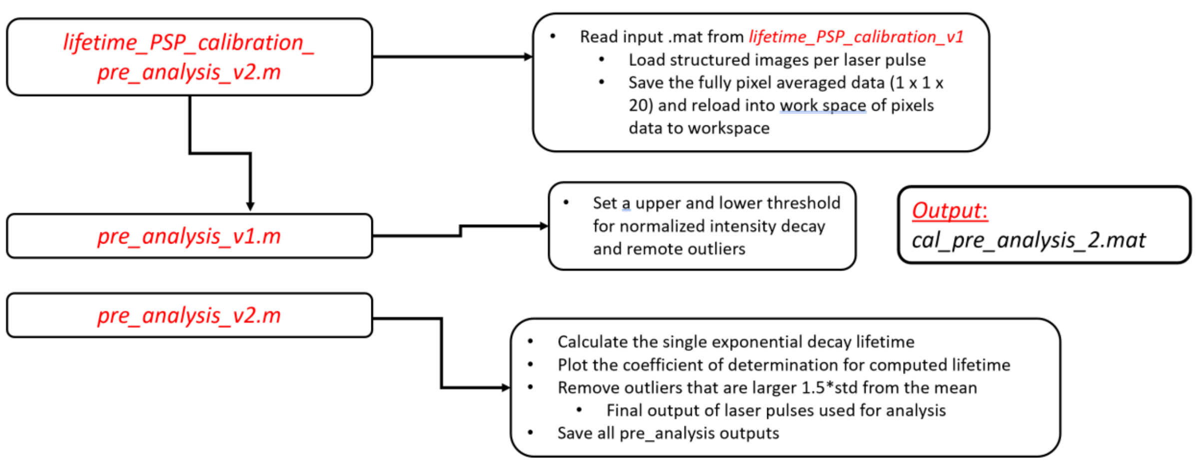

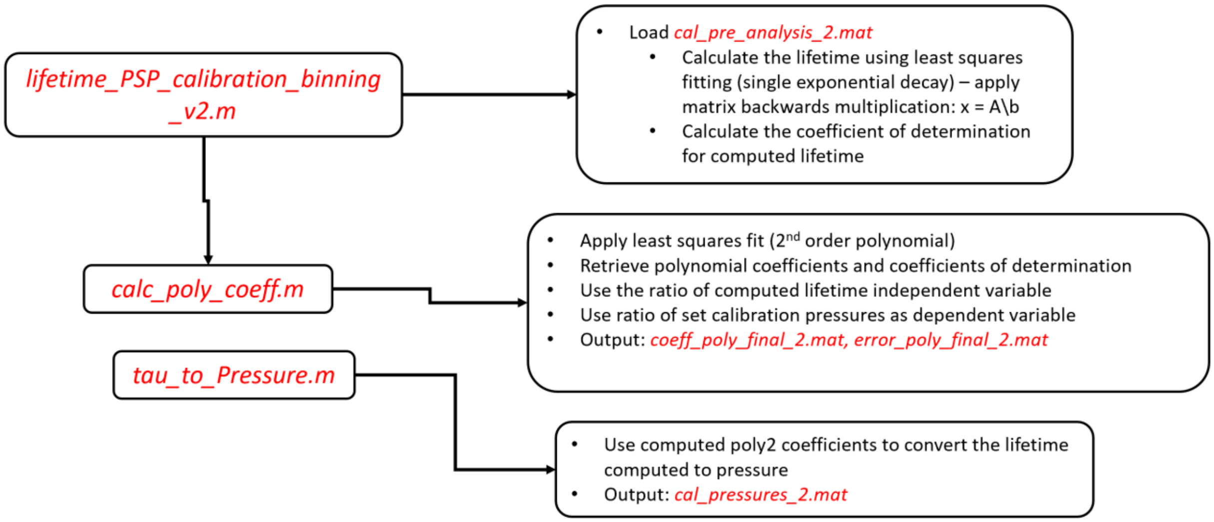
lifetime_PSP_calibration_binning_v2.m
Load cal_pre_analysis_2.mat
Calculate the lifetime using least squares fitting (single exponential decay) – apply matrix backwards multiplication: x = A\b
Calculate the coefficient of determination for computed lifetime
calc_poly_coeff.m
Apply least squares fit (2nd order polynomial)
Retrieve polynomial coefficients and coefficients of determination
Use the ratio of computed lifetime independent variable
Use ratio of set calibration pressures as dependent variable
Output: coeff_poly_final_2.mat, error_poly_final_2.mat
tau_to_Pressure.m
Use computed poly2 coefficients to convert the lifetime computed to pressure
Output: cal_pressures_2.mat

APPENDIX C: INSERT DESIGN AND ANALYSIS FOR CONVENTIONAL AND OPTICAL SENSORS FOR TURBINE FACILITY

Acknowledgment of prior publication: D.G. Cuadrado, P.A.N. Aye-Addo, V. Andreoli, L. Bhatnagar, F. Lozano, J. Fisher, G. Paniagua, J. Saavedra, D. Inman, T. Meyer, M. Bloxham, E. Clemens, B. Stults, T. White, A. Wallace and D. Johnson, 2019. Purdue Small Turbine Aerothermal Rotating Rig (STARR). AIAA Propulsion and Energy 2019 Forum, Indianapolis, pp. 1–13, August 2019

A) Design of instrumentation inserts in a turbine facility

Modular blade track inserts with a wide range of sensors were designed to investigate aero-thermal tip flows. The design was based on over-tip instrumentation of a high-pressure turbine at the CT3 facility, VKI [60]. The design criteria of the rig included comprehensive instrumentation integration to understand modern turbine flow features. The modular inserts utilize axial and pitch-wise measurements within the rotor casing. This establishes a unique capability of high spatial measurements over the rotor tip, including unsteady pressure, heat flux, tip clearance/tip timing, and optical techniques. The inserts are located in six locations around the casing per stage, as shown in Figure B1.

The modularity allows for the interchangeability of inserts with different types of sensors. Additionally, the instrumented inserts can be flipped 180° to gain more axial and pitch measurements. The difference between blue and black symbols in Figure B2 represents the 180° insert flip configuration. There are currently five different types of insert designs: blank insert (shown in Figure B2 with no instrumentation (6 per stage), tip clearance (3 per stage), high-frequency pressure (1 per stage), low-frequency pressure (1 per stage), and optical window inserts (1 per stage). The simple construction of the inserts enables the rapid, cost-effective testing of novel sensors.

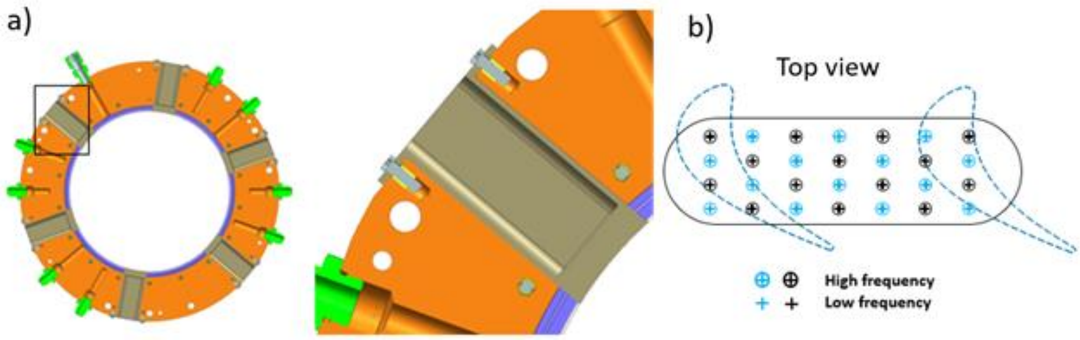

Figure C - 1: a) Over-blade tip inserts installed in casing and b) Top view of high and low-frequency pressure measurements located in the insert

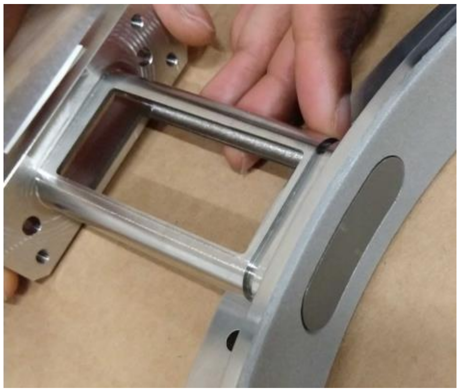

Figure C - 2

The tip clearance insert was designed with eight axial locations and 14 total pitch-wise locations across a standard blade tip. For high-frequency measurements, a Fogale nanotech system with two different diameter sizes of capacitance probes (1 mm and 2.5 mm) was purchased. The Fogale system has the added benefit of static mode calibration, so the sensors can be calibrated without running the facility for long periods.

The measurement resolution of the capacitance probes is half the diameter of the electrode size. The 1 mm electrode provides good resolution of different blade squealer tip rail designs, and the 2.5 mm electrode provides good resolution for larger clearance configurations. Additionally, the larger electrode diameter offers a more extensive resolution measurement range in locations where inertia is not uniform. The capacitance probes measure the clearance for every rotor blade. Additional wear gauges measure the tallest rotor blade's clearance and establish a calibration datum.

The casing static pressure is measured by high-frequency piezo-resistive pressure sensors (Kulite XCE-062 fast response miniature pressure transducers) and low-frequency pneumatic lines connected to static pressure tappings. The high and low-frequency pressure sensors are staggered with four axial and seven pitch-wise measurement points, as shown in Figure B2. The hole diameter of the sensors produces resonance of around 90 kHz. The sensor is recessed from the wall for better protection against debris. Moreover, the recess of the sensor provides a higher spatial resolution since the hole diameter facing the flow path can be much smaller than the sensor pressure-sensitive diaphragm. The dimensions and tolerances for machining inserts require advanced manufacturing techniques such as Electrical Discharge Machining (EDM). The radial location of these inserts can be modified using shims in the outer casing, accommodating different experiment configurations.

To foster the advancement of optical diagnostics toward more relevant turbine flow fields, access to the facility for laser delivery and imaging was prioritized. The application of high-speed laser-based measurements can significantly improve the spatial resolution and temporal resolution of data acquisition while simultaneously reducing the possibility of perturbing the complex flow field. With custom-built burst-mode laser systems [42], the capability of performing Phosphor-based surface thermometry [39] up to 100 kHz has been demonstrated at Purdue University. Modifications to existing hardware on the STARR facility have been implemented to enable optical access to the turbine airfoils for these measurement techniques with minimal impact on the overall design and function of the rig.

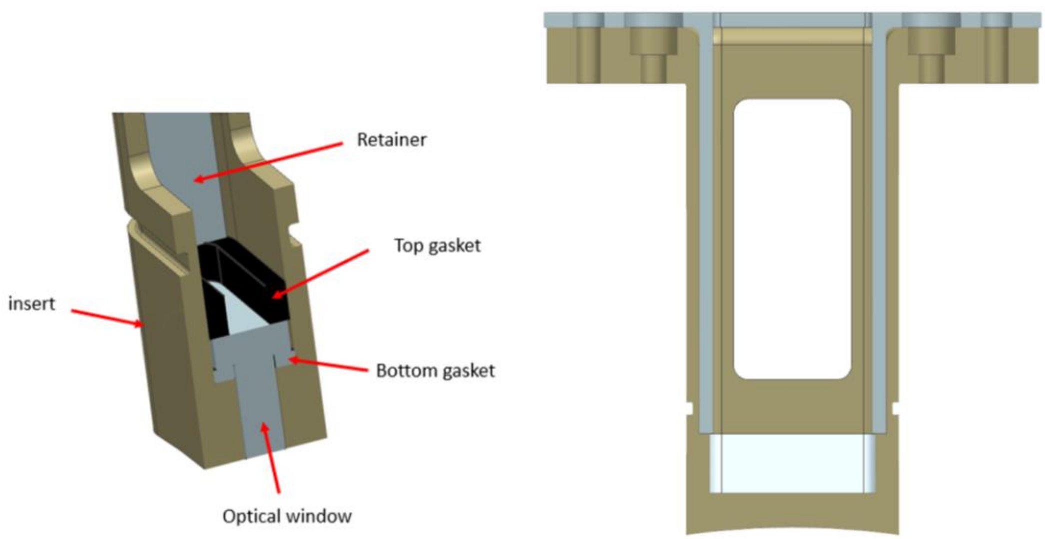

Figure C - 3: Optical over blade tip insert arrangement

Instrumentation inserts used to hold tip clearance measurement probes and other devices over the bladed section can be removed and replaced with small window inserts to allow laser delivery access to the blade passage section for velocity measurement, as shown in Figure B3. A laser sheet can be delivered into the test section to perform PIV with optics placed outside the rig. From the traversing ring downstream, borescope-type imaging probes attached to high-speed cameras can be used to image upstream of the illuminated region. With two separate camera probes, stereo-PIV can be conducted to yield time-resolved 3-component velocity measurements in a plane. This will enable in-depth studies of secondary vortex interaction in the blade passage section, which is a critical factor in analyzing the efficiency of a given turbine design. The proposed PIV layout is shown in Figure B4. Shown as A in the figure are two borescope imaging probes. High-pressure and high-temperature rated borescopes that can be directly mounted to high-speed cameras will be used for image acquisition. B shows the imaging line of sight to the measurement region shown as C. In the figure on the right, D displays the modified optical access insert with sheet forming optics, E, and a window for sealing, represented by F.

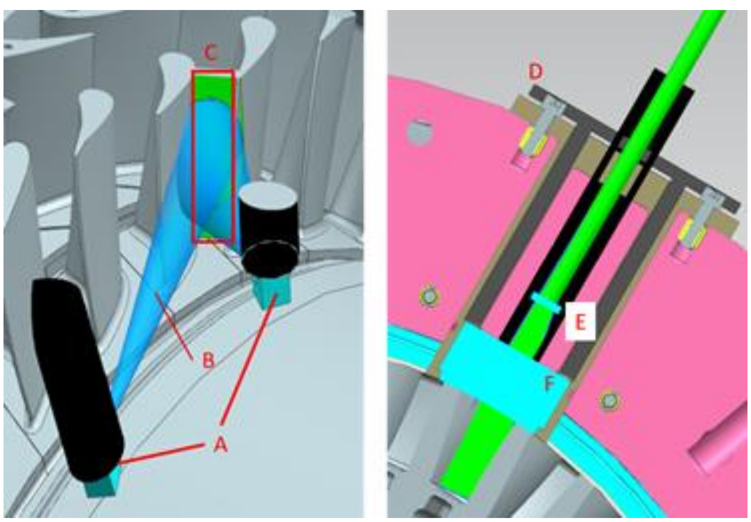

Figure C - 4: PIV layout to measure rotor passage flow field

It is also possible to conduct optical surface measurements such as PSP and phosphor-based surface thermometry in the facility, but a different optical layout is needed. The pressure or temperature on the blade tip surface can be measured using the optical insert for laser delivery. A dichroic mirror in the optical layout setup can separate the illumination light from the fluorescence or phosphorescence. Alternatively, laser delivery through specially designed probes installed in the downstream traversing ring enables flood illumination of the suction side of the blade airfoils. A high-speed camera can track unsteady temperature or pressure fluctuations with responsive coatings applied to this region. Pressure measurements can be used to track unsteady separation, which can cause performance losses in the turbine, while high-speed temperature measurements can lead to new insight on heat transfer mechanisms in the system.

Finite Element Analysis (FEA) setup/results of blank inserts:

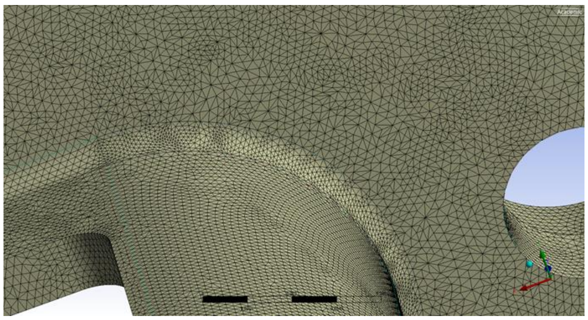

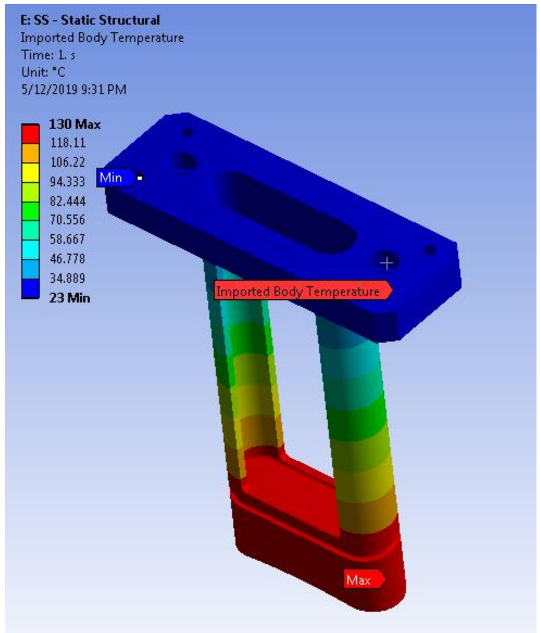

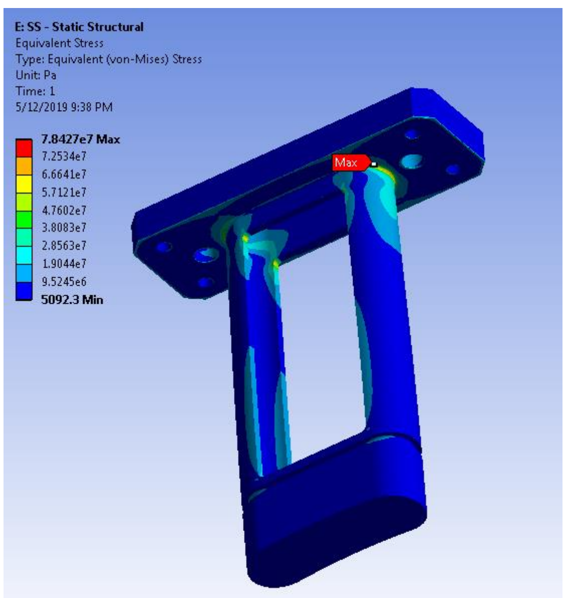

APPENDIX D: DATA ACQUISITION SYSTEMS AND SENSORS FOR TURBINE FACILITY

The sensors required for experiments are selected to meet the criteria of performing high fidelity experiments in the facility on a stationary turbine vane. It is essential to characterize the facility before applying any novel measurements techniques. This will ensure a baseline characterization of the wind tunnel, such as turbulence intensity, spatial variability, and the time response of the sensors used in the experiments. The sensors are compared with the optical measurements and should have high accuracy.

Each experiment may require both low and high-frequency sensors for time-averaged and time-resolved data analysis. Therefore, two chassis were selected for the experimental facility. The chassis was from National Instrument (PXIe-1075). The first chassis is dedicated to high-frequency sensors, and the second is reserved for low-frequency sensors. An MXI-express fiber optical cable from National Instrument sends data from the NI chassis to the desktop computer in the control room and synchronizes the two chassis. To handle large data files while running multiple data acquisition programs, the desktop computer was built with the following specs: 4 TB 3.5" Serial ATA (5.4 rpm) Hard drive, 1 TB 2.5" SATA Class 20 SSD, and 1 TB 3.5" SATA (7.2k rpm).

A National Instrument PXIe-6368 Analog-to-Digital (A/D) card with a maximum 2 MHz/channel sampling rate is utilized with an SCB68 connector block for all high-frequency sensors. The sensors are first connected to an analog low pass filter to avoid aliasing. It is important to note that an anti-aliasing filter does not necessarily prevent user error of aliasing if the experiment's incorrect sampling rate is selected. A National Instrument PXIe-6363 A/D card with a maximum sampling rate of 31.25 kHz/channel is also utilized with a SCB68 connector block for low-frequency sensors.

A low-frequency reference pressure sensor with high accuracy is required to calibrate the PSP and corroborate the results. The Scanivalve pressure scanner units (DSA 3217 and MSP 4264) are Ethernet-based devices that have accuracies of 0.05% of the full-scale range of the pressure scanner. These units were also selected based on their included pressure range below ambient pressure to calibrate with the PSP with the entire section under vacuum conditions. The individual units are temperature compensated. The flow and wall temperature are essential to characterize the gas to wall temperature ratio during the test run. A VTI EX1048 thermocouple conditioner with a built-in anti-aliasing filter was selected with an accuracy of less than 0.3°C. The additional temperature measurement near the PSP coating is for correcting temperature errors. Specifically for metal or wall temperature, Resistance Thermocouple Detectors (RTD's) are utilized and are sampled with a NI PXIe-4357 specially designed for RTDs. The RTD's are suitable for metal or wall temperatures that are not sticking in the flow because they are accurate and stable over time. However, they suffer from a slow time response in comparison to thermocouples.

A fast response pressure transducer is required to resolve sub-microseconds resolution to evaluate the unsteady data. A *Kulite* XCE-062A sensor was selected as a high-frequency pressure sensor to serve as a reference pressure for dynamic calibration of the pressure-sensitive paint and comparison with PSP unsteady data. The sensors require a signal conditioner acquired from Precision Filters (PFI), inc. The filter has a specific low frequency, high frequency, and temperature output, each with respective cut-off frequencies. *Pickering Connect* designed custom cabling to have a single connection from the Kulite sensor interface to the input on the PFI 28000 GUI chassis. The cabling design from the kulite sensor to the PFI chassis is shown in Figure D1. Another cable was designed through *Pickering Connect* to send data from the PFI chassis directly to the National Instrument chassis.

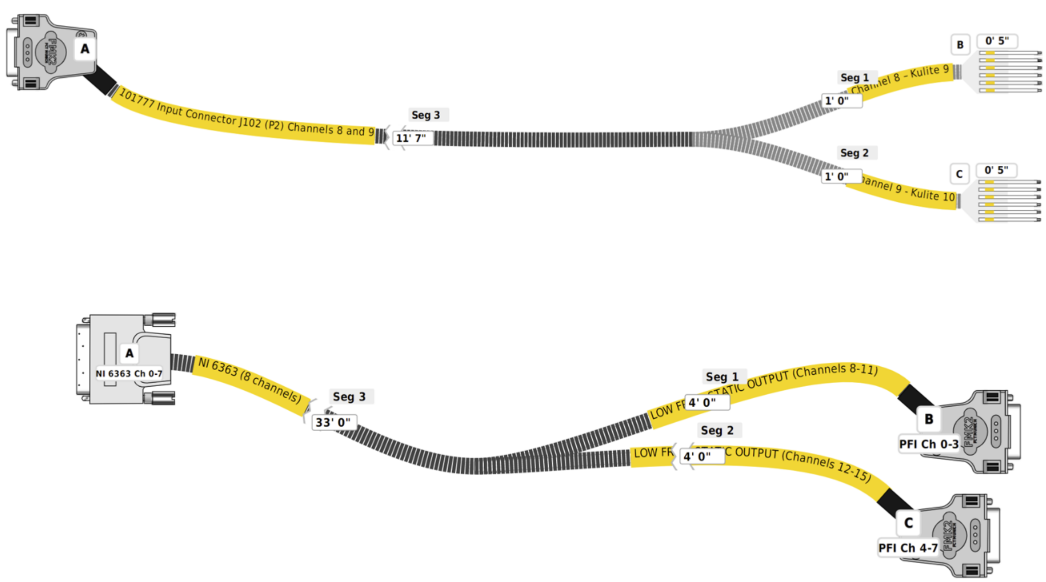

Figure D - 1: Custom cabling for Kulite wires (top), custom cabling from PFI chassis to NI A/D cards (bottom)

The results of steady calibration with the kulite sensors are shown in Figure D2. The coefficient of determination for both sensor calibrations was 0.9997.

$$P_1(V) = 3.21e6V - 8504$$

$$P_2(V) = 3.13e6V + 6720$$

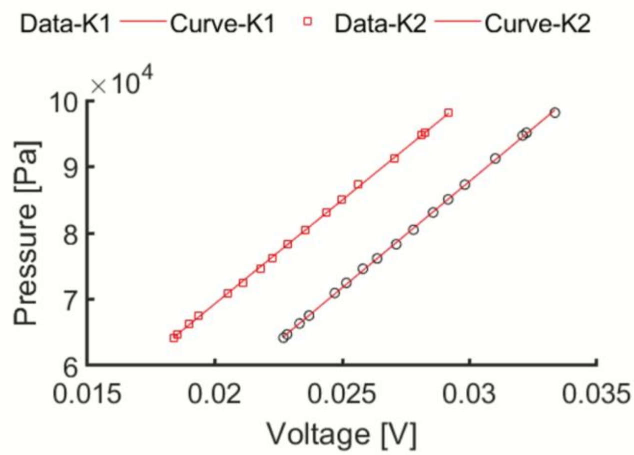

Figure D - 2: Kulite calibration results

The total number of sensors is selected to meet the criteria of high accuracy measurements. Each measurement follows a chain of transducer → conditioning system → Data acquisition card. The scope of channels correctly configured with appropriate data conditioning systems, adequately wired and documented, is key to efficient use between several different projects and teams in the lab.

Performance data acquisition measurement chain for turbine facility:

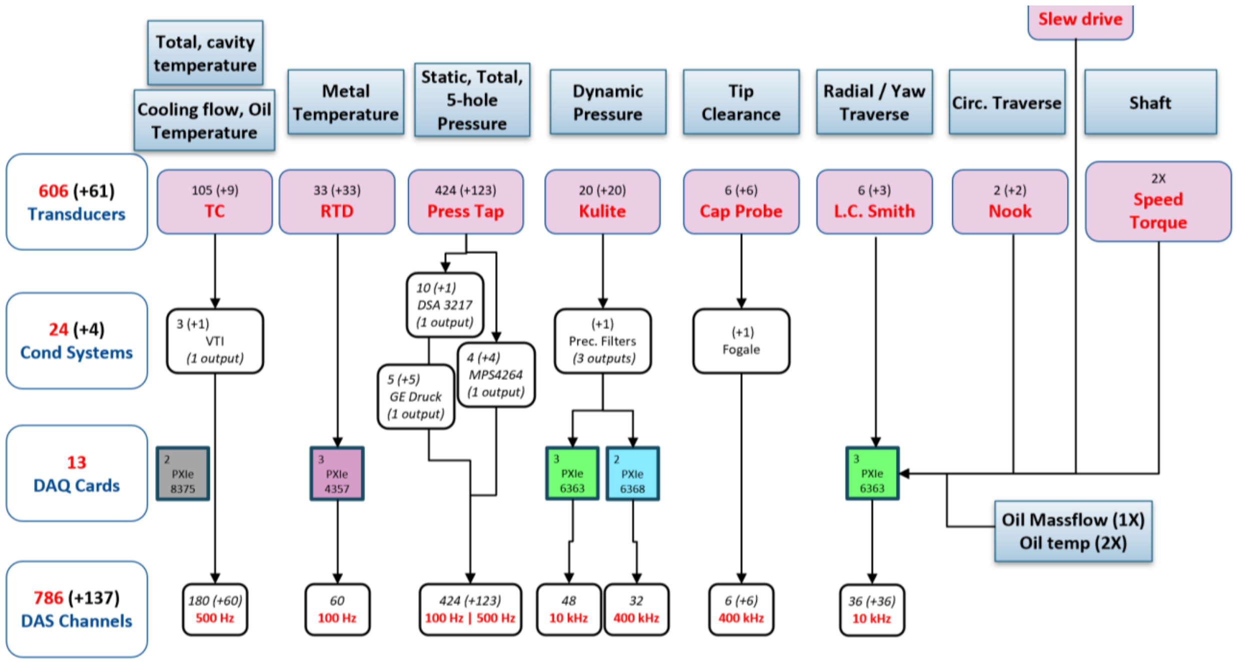

Health and safety acquisition measurement chain for turbine facility: